The Influence of Higher Order Waveguide Modes on Coherent Four-Wave Mixing in Hollow Fibers

A. N. Naumov*, F. Giammanco**, D. A. Sidorov-Biryukov*, A. B. Fedotov*, P. Marsili**, A. Ruffini**, and A. M. Zheltikov*

* International Laser Center, Physics Faculty, Moscow State University, 119899 Moscow, Russia

e-mail: zheltikov@top.phys.msu.su

** Dipartimento di Fisica e Unitá INFM—University of Pisa, via F. Buonarroti 2, 56127 Pisa, Italy

e-mail: giamma@df.unipi.it

Received February 2, 2001

Coherent four-wave mixing (FWM) of laser pulses in gas-filled hollow fibers is studied. The experimental data and the expressions derived for the amplitude of the FWM signal indicate that the excitation of higher order waveguide modes is an important physical factor having a considerable influence on nonlinear optical processes in hollow fibers. © *2001 MAIK "Nauka/Interperiodica".*

PACS numbers: 42.65.Hw

Nonlinear optical interactions in gas-filled hollow fibers are currently widely employed for the generation of extremely short light pulses [1, 2] and optical frequency conversion to the vacuum-ultraviolet and X-ray ranges (including the water-window region) through high-order harmonic generation [3–8]. Fibers of this type also allow the sensitivity of gas-phase analysis based on coherent four-photon spectroscopy to be considerably improved [9, 10].

An important advantage of hollow fibers is associated with the fact that they permit the pump and the signal generated through a frequency-nondegenerate nonlinear optical process to be phase-matched. With a careful choice of the parameters of a hollow fiber, the gas pressure, and excitation of appropriate waveguide modes, the phase mismatch related to the gas dispersion can be compensated for by the waveguide component of the phase mismatch [3, 8, 9, 11]. When these conditions are satisfied, the energy of the nonlinear signal can be considerably increased by using longer hollow fibers. Parameters of short pulses of short-wavelength radiation generated through nonlinear optical interactions in gas-filled hollow fibers can be controlled due to cross-phase modulation [12–14].

The results of nonlinear-optical experiments in hollow fibers are usually analyzed within the framework of models that ignore the possibility of excitation of higher order waveguide modes in the process of nonlinear optical interaction in a hollow fiber. Although such an approach provides an adequate qualitative description of the general features of nonlinear optical processes in hollow fibers, more detailed models are often necessary for calculating specific parameters of hollow fibers that allow the maximum efficiencies of nonlinear optical interactions to be achieved [10]. Such a more accurate analysis of nonlinear optical processes in hollow fibers has to include effects related to higher order waveguide modes, which may influence phase-matching conditions and change the energies of light pulses involved in nonlinear optical interactions. Experimental and theoretical investigation of such effects is the main aim of this paper.

Let us consider the process of coherent four-wave mixing (FWM) of the following type: $3\omega = 2\omega + 2\omega - \omega$, where ω and 2ω are the frequencies of pump pulses (fundamental radiation of the pump laser and its second harmonic). Processes of this type, as demonstrated by experiments [3], allow high efficiencies of nonlinear-optical frequency conversion to be achieved by phase-matching the light pulses involved in FWM in a hollow fiber. The results of our experimental studies for such processes will be presented below in this paper.

Suppose that fundamental radiation and its second frequency (pump pulses) propagate along the z axis of a hollow fiber with an inner radius a. We assume that the hollow fiber is filled with a gas with a cubic nonlinearity and a refractive index n. The dielectric constant of the cladding of the hollow fiber meets the condition $\varepsilon > n^2$. The fields of the pump and FWM pulses can then be represented as

$$E_1 = \frac{1}{2} f_1^q(\rho) A_0^q \exp[-i\omega t + (iK_1^q - \alpha_1^q/2)z] + \text{c.c.,} \quad (1)$$
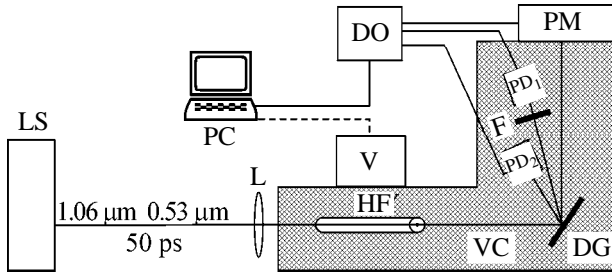
Fig. 1. Diagram of the experimental setup for studying the influence of the gas pressure on FWM processes in a gas-filled hollow fiber: LS, picosecond laser system; L, achromatic lens; VC, vacuum chamber; HF, hollow fiber; DG, diffraction grating; PM, photomultiplier; F, filter blocking pump beams; PD_1 and PD_2, photodiodes measuring the energy of fundamental radiation and the second harmonic, respectively; DO, digital oscilloscope; V, computer-controlled valve for gas delivery.

$$E_2 = \frac{1}{2}\sum_l f_2^1(\rho) B_0^l \exp[-2i\omega t + (iK_2^l - \alpha_2^l/2)z] + \text{c.c.,} \quad (2)$$

$$E_3 = \frac{1}{2} f_3^m(\rho) C^m(z) \exp[-3i\omega t + iK_3^m z] + \text{c.c.,} \quad (3)$$

where $f_1^q(\rho)$, $f_2^1(\rho)$, and $f_3^m(\rho)$ are the transverse field distributions corresponding to the EH_{1q}, EH_{1l}, and EH_{1m} hollow-fiber modes of the fundamental radiation, the second harmonic, and the FWM pulse, respectively (see [15, 16]); ρ is the distance from the axis of the hollow fiber; A_0^q and B_0^l are the amplitudes of the pulses of the fundamental radiation and the second harmonic at the input of the fiber; $C^m(z)$ is the slowly varying amplitude of the FWM signal; K_1^q, K_2^l, and K_3^m are the propagation constants of the fundamental radiation, the second harmonic, and the FWM signal in the hollow fiber, respectively; and α_1^q and α_2^l are, respectively, the attenuation coefficients for the EH_{1q} waveguide mode at the fundamental frequency and the EH_{1l} waveguide mode at the frequency of the second harmonic (see [15]). Representing the field of the second harmonic in Eq. (2) as a sum of hollow-fiber modes, we extend our analysis to FWM processes where two of the four waves have equal frequencies 2ω but different transverse field distributions corresponding to different waveguide modes $EH_{1l'}$ and $EH_{1l''}$ (i.e., $l = l', l''$).

Using standard assumptions concerning the properties of hollow fibers employed for nonlinear optical frequency conversion and analyzing the equation for the slowly varying envelope of the FWM signal using an approach similar to that described in [10, 11, 14], we arrive at the following expression for the amplitude of the FWM signal produced in the EH_{1m} mode of the hollow fiber:

$$C^m = i\beta^{ml'l''q} A_0^{q*} B_0^{l'} B_0^{l''} \left\{ \exp\left[-\frac{\alpha_3^m}{2}L\right] \right.$$

$$- \exp\left[\left(-\frac{\alpha_1^q + \alpha_2^{l'} + \alpha_2^{l''}}{2}\right.\right. \quad (4)$$

$$\left.\left. - i\Delta k^{ml'l''q}\right)L\right] \right\} \bigg/ \left(\frac{\alpha_3^m - \alpha_1^q - \alpha_2^{l'} - \alpha_2^{l''}}{2} - i\Delta k^{ml'l''q}\right),$$

where α_3^m is the attenuation coefficient for the EH_{1m} mode of the hollow fiber at a frequency of the FWM signal and L is the fiber length. Taking into consideration the dispersion of waveguide modes, we can represent the phase mismatch $\Delta k^{ml'l''q}$ involved in Eq. (4) as

$$\Delta k^{ml'l''q} = K_3^m - K_2^{l'} - K_2^{l''} + K_1^q \approx \Delta k^g + \Delta k'^{ml'l''q}, \quad (5)$$

where Δk^g and $\Delta k'^{ml'l''q}$ are the components of the phase mismatch due to the dispersion of the gas and waveguide dispersion, respectively. The fact that the wave-vector mismatch entering Eq. (4) and determining the efficiency of the FWM process depends not only on the gas dispersion but also on the dispersion of waveguide modes provides an opportunity to improve phase matching for a certain quadruple of waveguide modes of pump pulses and the FWM signal. The nonlinear coefficient $\beta^{ml'l''q}$ can be expressed in terms of the relevant nonlinear optical susceptibility [14]:

$$\beta^{ml'l''q} = \frac{27\pi\omega^2}{K_3^m c^2}$$

$$\times \chi^{(3)} \frac{\iint f_3^m(\rho) f_2^{l'}(\rho) f_2^{l''}(\rho) f_1^q(\rho) \rho \, d\rho \, d\theta}{\iint [f_3^m(\rho)]^2 \rho \, d\rho \, d\theta}, \quad (6)$$

where $\chi^{(3)}$ is the third-order nonlinear optical susceptibility responsible for the FWM process.

Expression (4) allows us to examine the dependence of the FWM-signal power on the geometric sizes of a hollow fiber and the type and pressure of the gas filling the fiber. Below, this expression will be used to analyze the results of our experiments.

The experimental setup for studying FWM processes in gas-filled hollow fibers (Fig. 1) consisted of a picosecond laser, a vacuum chamber with a hollow fiber inside, and a detection system based on a photomultiplier. The Nd:YAG picosecond laser generated 50-ps pump pulses at 1.06 µm (pump frequency ω) and 0.53 µm (pump frequency 2ω). The maximum energy of 1.06-µm radiation reached 100 mJ. A KDP crystal was used to produce the second harmonic of fundamen-

tal radiation. An achromatic lens was used to couple the laser beams into a hollow fiber. Two photodiodes were used to monitor the energies of both of these laser beams transmitted through the fiber. The energies of fundamental radiation and the second harmonic in these experiments were equal to 1 and 0.1 mJ, respectively. The signal produced through the FWM process in a hollow fiber was detected with a photomultiplier and then processed and displayed with a digital oscilloscope. The result of averaging over 30 FWM pulses was stored in a personal computer.

Comparison of the experimental data presented in Figs. 2 and 3 with the results of calculations performed with the use of Eq. (4) reveals a noticeable role of higher order waveguide modes in the FWM process in a hollow fiber. It is instructive in this context to consider in greater detail the results obtained for the FWM process $3\omega = 2\omega + 2\omega - \omega$ in an argon-filled hollow fiber with a length of 17.4 cm and an inner diameter $a = 100\ \mu m$ (Fig. 2). A satisfactory agreement between the experimental data (dots) and theoretical predictions (solid line) is achieved when effects related to higher order waveguide modes are included in the analysis. In particular, a satisfactory agreement between the experimental data in Fig. 2 and the results of calculations performed with the use of Eq. (4) was achieved when not only the FWM process occurring in the fundamental waveguide mode (i.e., the FWM process involving the EH_{11} hollow-fiber modes of the fundamental radiation, the second harmonic, and the FWM signal) but also the FWM process involving the EH_{12} mode of fundamental radiation, EH_{11} and EH_{13} modes of the second harmonic, and the EH_{12} mode of the FWM signal was included in calculations. The maximum of the FWM signal for an argon pressure of about 0.7 atm is observed within the pressure range where the FWM interaction in the fundamental waveguide modes is phase-matched (the dashed line in Fig. 2 shows the phase mismatch for this process). At lower pressures, the FWM interaction of the EH_{12} mode of fundamental radiation, EH_{11} and EH_{13} modes of the second harmonic, and the EH_{12} mode of the FWM signal begins to play a more important role (the phase mismatch for this process is shown by the dash-dotted line in Fig. 2). Thus, higher order waveguide modes of a hollow fiber may have a noticeable influence on FWM processes.

The results of our experiments also show that the role of higher order waveguide modes in nonlinear optical processes in a hollow fiber becomes more significant with an increase in the inner diameter of the fiber. Figure 3 presents the results of experiments performed for the FWM process $3\omega = 2\omega + 2\omega - \omega$ in an argon-filled hollow fiber with a length of 20.1 cm and an inner diameter of $a = 203\ \mu m$. To achieve a reasonable agreement between the experimental data (dots) and the results of calculations (solid line 1) in this case, we have to take into consideration FWM processes involving the EH_{11} and EH_{13} waveguide modes of fun-
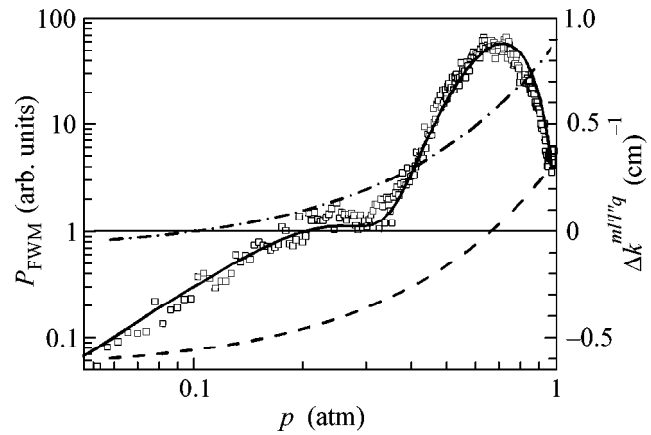
Fig. 2. The power of the FWM signal (the dots show the experimental data, and the solid line represents the results of calculations) and the phase mismatch for the FWM process $3\omega = 2\omega + 2\omega - \omega$ in an argon-filled hollow fiber as functions of the argon pressure p. The dashed line shows the phase mismatch for the FWM process occurring in the fundamental waveguide mode EH_{11}. The dash-dotted line represents the phase mismatch for the FWM process involving the EH_{12} mode of fundamental radiation, EH_{11} and EH_{13} modes of the second harmonic, and the EH_{12} mode of the FWM signal. The length of the hollow fiber is 17.4 cm, and the inner diameter is 100 μm.
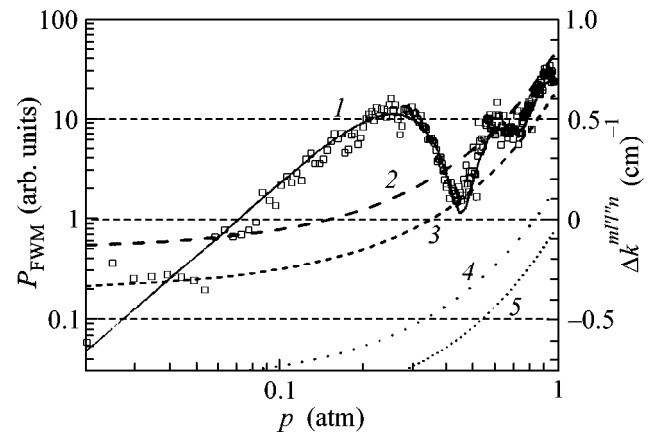
Fig. 3. The power of the FWM signal (the dots show the experimental data, and solid line 1 represents the results of calculations) and the phase mismatch for the FWM process in an argon-filled hollow fiber as functions of the argon pressure p. Dashed line 2 shows the phase mismatch for the FWM process occurring in the fundamental waveguide mode EH_{11}. Dashed and dotted lines 3–5 represent the phase mismatches for FWM processes involving (3) the EH_{13} mode of fundamental radiation, the EH_{11} and EH_{14} modes of the second harmonic, and the EH_{11} mode of the FWM signal; (4) the EH_{11} modes of fundamental radiation and the second harmonic and the EH_{12} mode of the FWM signal; and (5) the EH_{11} mode of fundamental radiation, the EH_{11} and EH_{12} modes of the second harmonic, and the EH_{13} mode of the FWM signal. The length of the hollow fiber is 20.1 cm, and the inner diameter is 203 μm.
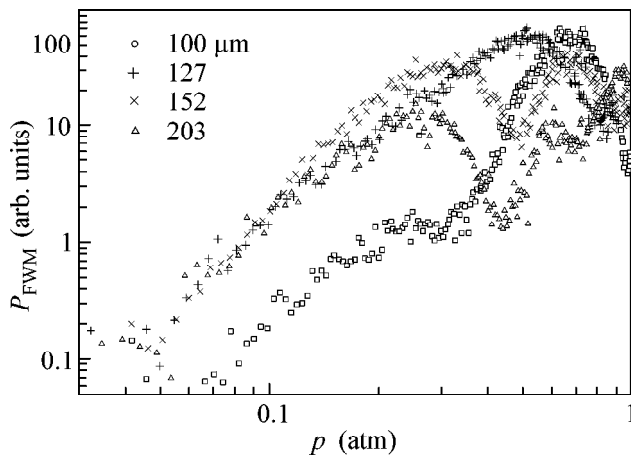
Fig. 4. The power of the FWM signal in argon-filled hollow fibers with different inner diameters as a function of the argon pressure p. The length of hollow fibers in all experiments was approximately equal to 20 cm. The inner diameter of the hollow fiber was ($\square$) 100, (+) 127, ($\times$) 152, and ($\triangle$) 203 μm.

damental radiation; the EH_{11}, EH_{12}, and EH_{14} waveguide modes of the second harmonic; and the EH_{11}, EH_{12}, and EH_{13} modes of the FWM signal (the phase mismatches for these FWM processes are shown by dashed lines *2–5* in Fig. 3). The maximum of the FWM signal observed for an argon pressure of about 0.25 atm then corresponds to the phase matching of the FWM process in the fundamental waveguide mode (the phase mismatch for this process is shown by dashed line *2* in Fig. 3). For an argon pressure of 0.6 atm, the chosen length of the fiber is close to a tripled coherence length of the FWM process ($L = 3L_{coh}$). The maximum of the FWM signal observed for an argon pressure of about 0.9 atm corresponds to the phase matching of the FWM process involving the EH_{11} modes of fundamental radiation and the second harmonic and the EH_{12} mode of the FWM signal (the phase mismatch for this process is shown by dashed line *4* in Fig. 3), as well as the FWM process involving the EH_{11} mode of fundamental radiation, the EH_{11} and EH_{12} modes of the second harmonic, and the EH_{13} mode of the FWM signal (the phase mismatch for this process is shown by dashed line *5* in Fig. 3). The four-wave mixing of the EH_{13} mode of fundamental radiation, the EH_{11} and EH_{14} modes of the second harmonic, and the EH_{11} mode of the FWM signal makes a noticeable contribution to the total FWM signal within the range of argon pressures from 0.3 up to 0.4 atm, where this FWM process is phase-matched (dashed line *3* in Fig. 3).

Figure 4 displays the power of the FWM signal generated in argon-filled hollow fibers with different inner diameters and a length of $\approx$20 cm as a function of the argon pressure p. As can be seen from Fig. 4, the maximum of the FWM signal related to the FWM process

in the fundamental mode of a hollow fiber is shifted toward lower pressures with an increase in the inner diameter of the hollow fiber, approaching its limiting position corresponding to the FWM process in collimated beams. In this limiting case, the maximum power of the FWM signal is achieved, in accordance with Eqs. (4)–(6), for a gas pressure of 0.16 atm in the fiber (at this pressure, the coherence length of the FWM process $L_{ph} = \pi/\Delta k^g$ becomes equal to the fiber length). Thus, the results of these measurements agree well with our expectations based on the analysis of Eqs. (4)–(6). The maximum of the FWM signal observed at an argon pressure of about 0.7 atm for a hollow fiber with an inner diameter of 152 μm can be attributed, by analogy with the cases considered above, to the FWM process involving higher order waveguide modes of pump and signal pulses.

Thus, the results of experimental and theoretical studies presented in this paper reveal several important features of nonlinear optical processes in gas-filled hollow fibers, giving a deeper insight into methodological aspects of the problem and opening new possibilities for practical applications of hollow fibers in nonlinear optics, optics of ultrashort pulses, and nonlinear spectroscopy. Our experimental results indicate that higher order waveguide modes may have a considerable influence on four-wave mixing processes in gas-filled hollow fibers. This effect can be employed to increase the total energy of short-wavelength radiation produced through nonlinear optical processes in hollow fibers. On the other hand, effects related to higher order waveguide modes should be taken into consideration in the optimization of hollow-fiber frequency converters and pulse compressors, where the excitation of higher order waveguide modes may lead to unwanted energy losses.

REFERENCES

1. M. Nisoli, S. De Silvestri, and O. Svelto, Appl. Phys. Lett. **68**, 2793 (1996).

2. M. Nisoli, S. De Silvestri, O. Svelto, *et al.*, Opt. Lett. **22**, 522 (1997).

3. C. G. Durfee III, S. Backus, M. M. Murnane, and H. C. Kapteyn, Opt. Lett. **22**, 1565 (1997).

4. A. Rundquist, C. G. Durfee III, Z. Chang, *et al.*, Science **280** (5368), 1412 (1998).

5. Y. Tamaki, K. Midorikawa, and M. Obara, Appl. Phys. B **B67**, 59 (1998).

6. C. G. Durfee III, A. Rundquist, Z. Chang, *et al.*, in *Proceedings of the International Quantum Electronic Conference, IQEC'98, San Francisco, 1998*, QPD5.

7. E. Constant, D. Garzella, P. Breger, *et al.*, Phys. Rev. Lett. **82**, 1668 (1999).

8. C. G. Durfee III, A. R. Rundquist, S. Backus, *et al.*, Phys. Rev. Lett. **83**, 2187 (1999).

9. R. B. Miles, G. Laufer, and G. C. Bjorklund, Appl. Phys. Lett. **30**, 417 (1977).

10. A. B. Fedotov, F. Giammanco, A. N. Naumov, *et al.*, Appl. Phys. B (in press).

11. A. N. Naumov, A. M. Zheltikov, A. B. Fedotov, *et al.*, J. Opt. Soc. Am. B (in press).

12. N. I. Koroteev and A. M. Zheltikov, Appl. Phys. B **B67**, 53 (1998).

13. C. G. Durfee III, S. Backus, H. C. Kapteyn, and M. M. Murnane, Opt. Lett. **24**, 697 (1999).

14. A. M. Zheltikov, N. I. Koroteev, and A. N. Naumov, Zh. Éksp. Teor. Fiz. **115**, 1561 (1999) [JETP **88**, 857 (1999)].

15. E. A. J. Marcatili and R. A. Schmeltzer, Bell Syst. Tech. J. **43**, 1783 (1964).

16. M. J. Adams, *An Introduction to Optical Waveguides* (Wiley, Chichester, 1981).

Translated by A. Zheltikov

Quasiclassical Analysis of the Spectra of Two Groups of Central Potentials

G. V. Shpatakovskaya

Institute of Mathematical Modeling, Russian Academy of Sciences, Miusskaya pl. 4a, Moscow, 125047 Russia

e-mail: shpat@imamod.ru

A method is suggested for analyzing the spectra of central attractive potentials either with Coulomb singularity (intra-atomic potentials) or finite at zero point (potentials in spherical clusters and nuclei). It is shown that, if the orbital degeneracy is removed, then $\varepsilon_{nl} - \varepsilon_{n0} \cong a_{\varepsilon_{n0}} (l + 1/2)^2$ for small l in the shell n. In atoms and ions, the coefficient a_ε is nonnegative, so that the energy in the n shell increases with l. The validity of this formula for the inner electrons is illustrated by calculating the spectrum of the mercury atom. In cluster potentials, the opposite situation, as a rule, occurs: the larger l, the lower the corresponding level ($a_\varepsilon < 0$). However, in the soft potentials of small clusters, spectral regions with different signs of a_ε coexist and the orbitally degenerate level exists in the spectral region where $a_\varepsilon = 0$. Aluminum clusters Al_N are taken as an example to find out how the position of the region with the degenerate level varies with varying cluster size N, and it is found that this region is "pushed out" to higher energies with an increase in N. In this connection, the presence of multiply ionized Al_N clusters of the corresponding size in a low-temperature aluminum plasma is discussed. © *2001 MAIK "Nauka/Interperiodica".*

PACS numbers: 31.10.+z; 36.40.Cg; 73.22.-f

1. Energy levels $\varepsilon_{n_r l}$ in the central potential depend on two quantum numbers: radial n_r and orbital l. In the quasiclassical approximation, they are determined by the Bohr–Sommerfeld quantization rule[1]

$$S_{\varepsilon\lambda} = \int_{R'_{\varepsilon\lambda}}^{R_{\varepsilon\lambda}} dr\, p_{\varepsilon\lambda}(r) = \pi\left(n_r + \frac{1}{2}\right), \qquad (1)$$

where $S_{\varepsilon\lambda}$ and $p_{\varepsilon\lambda}(r) = \sqrt{p_\varepsilon^2(r) - \lambda^2/r^2}$ are, respectively, the radial action and the radial momentum of an electron with energy ε and angular momentum $\lambda = l + 1/2$ and the integration domain is bounded by the turning points $R'_{\varepsilon\lambda}$ and $R_{\varepsilon\lambda}$. Let us introduce the function $\nu_\varepsilon(\lambda)$ expressed through the radial action as

$$\nu_\varepsilon(0) = \int_0^{R_{\varepsilon 0}} dr\, p_{\varepsilon 0}(r)/\pi, \quad \nu_\varepsilon(\lambda) = S_{\varepsilon\lambda}/\pi, \quad \lambda \neq 0.$$

The quantity $\nu_\varepsilon(\lambda)$ as a function of continuous argument λ decreases monotonically from the value $\nu_\varepsilon(0)$ to $\nu_\varepsilon(\lambda_\varepsilon) = 0$, where λ_ε is the maximal angular momentum for energy ε.

---

[1] Atomic units are used.

Let us examine how the function $\nu_\varepsilon(\lambda)$ depends on λ at small λ,

$$\nu_\varepsilon(\lambda) = \nu_\varepsilon(0) + \nu'_\varepsilon(0)\lambda + \frac{1}{2}\nu''_\varepsilon(0)\lambda^2 + \dots . \qquad (2)$$

For the spherical harmonic oscillator $U(r) = -V_0 + \omega^2 r^2/2$ and Coulomb potential $U(r) = -Z/r$, the function $\nu_\varepsilon(\lambda)$ is linear over the whole range of λ values:

$$Harm.\ osc. \quad \nu_\varepsilon(\lambda) = \nu_\varepsilon(0) - \frac{1}{2}\lambda, \quad \nu'_\varepsilon(0) = -\frac{1}{2}, \qquad (3)$$

$$Coul. \quad \nu_\varepsilon(\lambda) = \nu_\varepsilon(0) - \lambda, \quad \nu'_\varepsilon(0) = -1. \qquad (4)$$

It can easily be shown [1] that for the monotonic attractive potentials finite at zero point the first derivative in Eq. (2) is equal to $-1/2$, as is the case for an oscillator. These (anharmonic) potentials can be assigned to the group of harmonic oscillator. An example of the potential of this type is provided by the self-consistent potentials in spherical clusters and nuclei.

Likewise, the screened potentials having Coulomb singularity at zero point $U(r) \longrightarrow -Z/r\ (r \longrightarrow 0)$ can be assigned to the Coulomb group, for which $\nu'_\varepsilon(0) = -1$

[1]. In particular, the intra-atomic (intraion) potentials belong to this group.[2]

The second derivative at zero point $v_\varepsilon''(0)$ in Eq. (2) characterizes the degree of anharmonic or screening effect. It is precisely the quadratic term with $v_\varepsilon''(0) \neq 0$ that is responsible for removing orbital degeneracy inherent in the spectra of the "generic" potentials (harmonic oscillator and Coulomb).

2. Before proceeding to the analysis of the spectra with removed degeneracy, let us calculate the energy levels for the generic potentials.

For $l = 0$, quantization condition (1) for the harmonic oscillator reads

$$2v_\varepsilon(0) = n' + \frac{1}{2}, \tag{5}$$

because in this case the particle can pass through the center. For $l \neq 0$ one has

$$v_\varepsilon(\lambda) = v_\varepsilon(0) - \frac{\lambda}{2} = n_r + \frac{1}{2}, \quad n_r = 0, 1, 2, \ldots .$$

Substituting $v_\varepsilon(0)$ from Eq. (5) and denoting $n' = n + 1$, one obtains

$$(n - l)/2 = n_r, \tag{6}$$

whence it follows that the principal n ($n = 0, 1, \ldots$) and the orbital l quantum numbers have the same parity and that $2v_\varepsilon(0) = n + 3/2$. The evaluation of the integral $v_\varepsilon(0) = (V_0 - |\varepsilon|)/2\omega$ yields the well-known expression for the spectrum: $\varepsilon_{n,l} = -V_0 + \omega(n + 3/2) = -V_0 + \omega(2n_r + l + 3/2)$.

For the Coulomb potential, quantization condition (1), with regard to Eq. (4), takes the form

$$v_\varepsilon(\lambda) = v_\varepsilon(0) - l - \frac{1}{2} = n_r + \frac{1}{2}, \quad n_r = 0, 1, 2, \ldots,$$

where $v_\varepsilon(0) = Z/\sqrt{2|\varepsilon|}$. Therefore, $\varepsilon_{n,l} = -Z^2/2(n_r + l + l)^2 = -Z^2/2n^2$, $n = 1, 2, \ldots$.

For the anharmonic potential, the energy ε_{n0} of the s level is also determined from the quantization condition of the type (5). Expanding the action $v_\varepsilon(\lambda)$ in powers of energy in the vicinity of this level, one obtains for the left-hand side of Eq. (1)

$$v_\varepsilon(\lambda) \cong v_{\varepsilon_{n0}}(\lambda) + \frac{\partial v_\varepsilon(0)}{\partial \varepsilon}\bigg|_{\varepsilon_{n0}} (\varepsilon - \varepsilon_{n0})$$

$$\cong v_{\varepsilon_{n0}}(0) - \frac{\lambda}{2} + \frac{1}{2}v_{\varepsilon_{n0}}''(0)\lambda^2 + \frac{\tau_{n0}}{\pi}(\varepsilon - \varepsilon_{n0}).$$

---

[2] An example of a potential from this group, namely, the Thomas–Fermi potential of a free atom, was analyzed in detail in [2, 3], where the special case $\varepsilon = 0$ was set apart because the value of the derivative $v_\varepsilon'(0)$ in this case depends on the rate of potential decrease at infinity.

Here, the notation $\tau_\varepsilon = \partial S_\varepsilon/\partial \varepsilon$ is introduced for the classical time, and expansion (2) with $v_\varepsilon'(0) = -1/2$ is used. Note that the λ dependence of the $\partial v_\varepsilon(\lambda)/\partial \varepsilon|_{\varepsilon_{n0}}$ derivative is not taken into account because it would be beyond the adopted accuracy. The right-hand side of quantization condition (1) [cf. Eq. (6)] can be rewritten as $n_r + 1/2 = n/2 + 3/4 - \lambda/2$, after which one gets

$$\varepsilon_{nl} = \varepsilon_{n0} - \Delta\varepsilon_n \frac{1}{2}v_{\varepsilon_{n0}}''(0)\lambda^2, \tag{7}$$

where the value $\Delta\varepsilon_n = \pi/\tau_{n0}$ is the spacing between the s levels of the neighboring n shells.

Similar mathematics for the potentials of the Coulomb group gives the same result (7). Equation (7) provides the quantitative measure for the degeneracy removal in the anharmonic or screened potential and suggests the quadratic dependence of the corresponding splitting on the orbital angular momentum, with the sign of shifting from the s level being dependent on the sign of the $v_{\varepsilon_{n0}}''(0)$ derivative. For the positive sign, the energy decreases with increasing l, and for the negative sign it increases with l. The latter situation occurs in atoms, and both variants may occur in clusters.

3. In an atom (and in an ion in plasma), the screening of the Coulomb potential brings about a constant shift of the deepest energy levels by a value corresponding to the potential of the electron cloud (and environment) at the nucleus. In this energy range, $v_\varepsilon''(0) = 0$, so that the spectrum is Coulomb-like, except that it is shifted by the above-mentioned constant. For higher n shells, the screening becomes substantial. Quantitatively, this is manifested in the $v_\varepsilon''(0)$ value: it is negative [$v_\varepsilon''(0) < 0$] and increases in magnitude (cf. [4] for plasma). If the coefficient of $\Delta\varepsilon_n$ in Eq. (7) becomes larger than unity, the neighboring shells overlap, as is actually observed in the spectra of atoms (and ions).

To demonstrate the domain of applicability of Eq. (7), the electronic spectrum of the mercury atom is taken as an example. The quasiclassical intra-atomic potential corresponds to the Thomas–Fermi model:

$$U(r) = -\frac{Z}{r}\phi\left(\frac{r}{r_0}\right), \quad r_0 = bZ^{-1/3}, \tag{8}$$

where Z is the atomic number, the function $\phi(x)$ is approximated by the Tietz expression [5] $\phi(x) = (1 + x)^{-2}$, and $b = 4.5^{1/3}$. The results of the calculations of the spectrum of the mercury atom ($Z = 80$) by Eq. (7) and directly from quantization condition (1) are presented in the table. The data for the inner p and d electrons are in good agreement. The Hartree–Fock energies of inner electrons are also given in the table. These data also confirm that the dependence is close to Eq. (7), because the coefficients $a_{n0} = -(\varepsilon_{nl} - \varepsilon_{n0})/(l + 1/2)^2$ are virtually

Spectrum of the mercury atom ($Z = 80$)

nl	$-\varepsilon_{nl}$ (HF)	$-\varepsilon_{nl}$ (1)	$-\varepsilon_{nl}$ (7)	nl	$-\varepsilon_{nl}$ (HF)	$-\varepsilon_{nl}$ (1)	$-\varepsilon_{nl}$ (7)
$1s$	2778.6	2803.6	2803.6	$4s$	25.6	23.4	23.4
$2s$	470.7	477.1	477.1	$4p$	21.7	19.9	19.6
$2p$	452.2	464.2	462.7	$4d$	14.6	13.2	12.7
$3s$	113.1	110.6	110.6	$4f$	5.0	3.7	2.3
$3p$	104.3	102.8	102.2	$5s$		3.7	3.7
$3d$	88.1	87.8	87.3	$5p$		2.34	2.34
				$6s$		0.257	0.257

constant within the n shells considered: $a_{30} = 3.95 \pm 0.05$ and $a_{40} = 1.72 \pm 0.04$.

4. A more complicated situation occurs for the spectra of the cluster potentials belonging to the anharmonic group. As a rule, clusters exhibit quite the reverse behavior: the larger l, the lower the corresponding level in the shell, and the derivative is positive [$v_\varepsilon''(0) > 0$]. However, a subgroup of "soft" potentials [6] for which the $v_\mu''(0) < 0$ value is negative (μ is the chemical potential, i.e., Fermi energy at zero temperature) in small clusters with $N < N_F$ should be considered separately. The upper portion of the spectra of such clusters has a region displaying the "abnormal" behavior with the negative $v_\varepsilon''(0)$ value. In clusters of a fixed size, the derivative $v_\varepsilon''(0)$ increases with lowering energy ε and changes sign at a certain energy. In the region where $v_\varepsilon''(0) = 0$, an l-degenerate level appears. As the cluster size increases (the number N of its atoms increases), the region where $v_\varepsilon''(0) = 0$ "moves" to higher energies, so that the degenerate level in a cluster

with $N = N_F$ proves to be the highest (near the Fermi energy μ). As for the clusters with $N > N_F$, their spectra have the "normal" shape [with $v_\varepsilon''(0) > 0$] over the whole range of ε values.
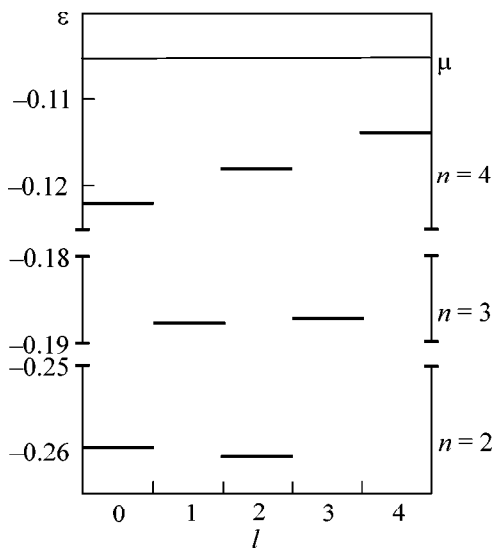
The calculations carried out in this work for the spectra of the Al_N clusters using Eq. (1) and the Woods–Saxon potential (the corresponding parameters are given, e.g., in [6]) confirm these conclusions. The abnormal region of the spectrum of Al_{33} near the Fermi energy μ ($n = 4$) is shown in the figure. The presence of a nearly degenerate level ($n = 3$) and the normal l dependence below it ($n = 2$) are clearly seen in the figure. The calculations predict $N_F = 57$; in the Al_{57} cluster, the level energies in the highest almost degenerate shell with the principal quantum number $n = 5$ are $\varepsilon_{51} = \varepsilon_{53} = -0.126$, $\varepsilon_{55} = -0.127$, and $\mu = -0.105$.

The presence of a degenerate level near the Fermi energy with ionization potential approximately half the first ionization potential of the aluminum atom ($I_1 = 0.22$) indicates that the clusters of size $N \sim N_F$ may be multiply ionized even at not too high a temperature and that multiply charged clusters may present in a low-temperature aluminum plasma.

Electronic spectrum in the Woods–Saxon potential for the Al_{33} cluster.

REFERENCES

1. D. A. Kirzhnits and G. V. Shpatakovskaya, Zh. Éksp. Teor. Fiz. **62**, 2082 (1972) [Sov. Phys. JETP **35**, 1088 (1972)].
2. B. G. Englert and J. Schwinger, Phys. Rev. A **32**, 26 (1985).
3. B. G. Englert, in *Lecture Notes in Physics*, Vol. 300: *Semiclassical Theory of Atoms* (Springer-Verlag, Berlin, 1988).
4. D. A. Kirzhnits and G. V. Shpatakovskaya, Preprint No. 33, Fiz. Inst. Ross. Akad. Nauk im. P.N. Lebedeva (Lebedev Institute of Physics, Russian Academy of Sciences, Moscow, 1998).
5. T. Tietz, J. Chem. Phys. **22**, 2094 (1954).
6. G. V. Shpatakovskaya, Pis'ma Zh. Éksp. Teor. Fiz. **72**, 394 (2000) [JETP Lett. **72**, 269 (2000)]; cond-mat/0011393.

Translated by V. Sakun

Kossel Lines in Extremely Asymmetric Diffraction Schemes

A. M. Afanas'ev[1], M. V. Koval'chuk[2], and M. A. Chuev[1]

[1] *Institute of Physics and Technology, Russian Academy of Sciences, Nakhimovskiĭ pr. 36, Moscow, 117218 Russia*

[2] *Shubnikov Institute of Crystallography, Russian Academy of Sciences, Leninskiĭ pr. 59, Moscow, 117333 Russia*

Received February 18, 2001

It is demonstrated theoretically that the intensity distribution within the Kossel lines in an extremely asymmetric X-ray diffraction scheme has an anomalous shape of a sharp peak exceeding the background intensity by several hundred times. The possibility of experimental observation of this phenomenon is discussed. © *2001 MAIK "Nauka/Interperiodica".*

PACS numbers: 61.10.Dp

A unique possibility associated with the use of Kossel lines in determining the scattering phase amplitudes and in X-ray structural analysis was pointed out as early as the 1960s [1]. More recently, this problem was theoretically explored in detail in [2, 3], and a series of experiments were carried out in the last five years [4, 5]; this approach was eventually given the name X-ray holography method. Although the method of Kossel lines has long been known [6], the main physical phenomena arising upon the escape of this radiation from perfect crystals are still not fully understood. It was shown in [7] that the diffraction of an X-ray beam in a extremely asymmetric scheme (see Fig. 1) is accompanied by the formation of a strongly compressed beam at a certain depth in the crystal. This beam propagates parallel to the crystal surface, and the degree of compression may be as high as several hundred times. This prediction was experimentally confirmed by the X-ray standing-wave method with the detection of photoelectrons [8, 9] by a specially designed proportional gas counter [10]. One can naturally expect that this phenomenon should affect the intensity distribution within the Kossel line. It is shown below that the Kossel lines in this diffraction scheme have an entirely different structure and that the intensity distribution in the secondary X-radiation has the shape of a sharp peak, whose intensity exceeds the background intensity by several hundred times.

An extremely asymmetric diffraction occurs in the so-called Bragg–Laue geometry, for which the diffracted wave propagates nearly parallel to the crystal surface, so that the diffraction geometry may be changed from the Laue geometry to the Bragg geometry by a small change in the angle of incidence of the initial X-ray beam on the crystal (Fig. 1). To determine the wave-field distribution in the crystal for this diffraction scheme, one should take into account not only the diffraction scattering but also the mirror reflection of

the diffracted wave from the crystal surface. In this case, the wave fields in crystal are determined by the following expression:

$$D(z) = \sum_{j=1,2} (D_0^{(j)} e^{i\mathbf{k}_{0j}\mathbf{r}} + D_h^{(j)} e^{i\mathbf{k}_{hj}\mathbf{r}}), \qquad (1)$$

where the wave vectors of the incident and diffracted waves in crystal

$$\mathbf{k}_{0j} = \boldsymbol{\kappa}_0 + \frac{\kappa\chi_0}{2\varphi_0}\mathbf{n} + \kappa y_j\mathbf{n} \qquad (2)$$

and

$$\mathbf{k}_{hj} = \mathbf{k}_{0j} + \mathbf{K}_h \qquad (3)$$

($\boldsymbol{\kappa}_0$ is the wave vector of the incident wave in a vacuum, and $\mathbf{K}_h$ is the reciprocal lattice vector) are determined by the roots of the third-order equation [7]

$$y[(y + \eta_h)^2 - \tilde{\varphi}_h^2] - \delta_0^3 = 0, \qquad (4)$$
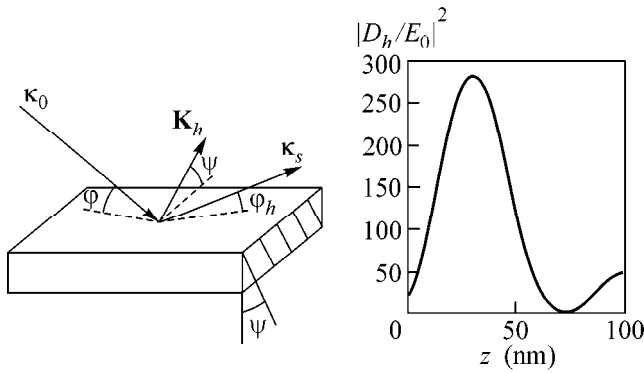
where

$$\tilde{\varphi}_{0,h} = \sqrt{\varphi_{0,h}^2 + \chi_0}, \quad \eta_h = \tilde{\varphi}_0 - |\tilde{\Psi}|,$$

$$\delta_0 = \left(\frac{c^2\chi_h\chi_{\bar{h}}}{2\varphi_0}\right)^{1/3}, \qquad (5)$$

$$\varphi_h^2 = (\tilde{\varphi}_0 - |\tilde{\Psi}|)^2 + 2\sin(2\theta_B)\Delta\theta, \qquad (6)$$

$|\tilde{\Psi}| = 2|\Psi|\sin\theta_B$ is the effective misorientation angle, θ_B is the Bragg angle, $\Delta\theta$ is the deviation from the Bragg angle, χ_h is the Fourier component of polarizability for a given reflection, and c is the polarization factor. Dispersion Eq. (4) has three roots, two of which, satisfying the condition $\text{Im}(y_{1,2} + \chi_0/2\varphi_0) > 0$, deter-

Fig. 1. The diffraction scheme in the extremely asymmetric Bragg–Laue geometry and the depth distribution of the squared modulus of diffracted wave amplitude inside a Ge crystal, as calculated for the (220) reflection of GeK_α ($\Psi = 30°$, $\varphi = 1128'$, and $\Delta\theta = 3.2''$). Ψ is the angle between the normal to the surface and the reflecting planes.

mine extinction modes (1). The field amplitudes $D_0^{(j)}$ and $D_h^{(j)}$ are given by

$$D_h^{(1)} = \frac{\varphi_h + \eta_h + y_2}{y_2 - y_1} E_h^s,$$

$$D_h^{(2)} = -\frac{\varphi_h + \eta_h + y_1}{y_2 - y_1} E_h^s, \qquad (7)$$

$$D_0^{(j)} = \frac{c\chi_{\bar{h}}}{2\varphi_0 y_j} D_h^{(j)},$$

where

$$E_h^s = \frac{c\chi_h}{y_3(\varphi_h - \eta_h - y_3)} E_0 \qquad (8)$$

is the amplitude of the reflected wave and y_3 is the root of Eq. (4) with $\mathrm{Im}(y_3 + \chi_0/2\varphi_0) < 0$.

One can see from these expressions that the $D_h^{(j)}$ amplitudes far exceed E_h^s if the roots of dispersion Eq. (4) are close to each other. In the absence of absorption, one can readily find the degeneracy point at

$$\eta_h = -\frac{3}{2}\delta_0 \quad \text{and} \quad \varphi_h^2 = \varphi_c^2 - \frac{3}{4}\delta_0^2, \qquad (9)$$

where all three roots are equal:

$$y_{1,2,3} = \delta_0. \qquad (10)$$

For the amplitude of the diffracted wave in crystal, one obtains at this point

$$D_h(z) = E_h^s + i\frac{c\chi_h}{\delta_0}\kappa z E_0; \qquad (11)$$

i.e., the amplitude $D_h(z)$ grows indefinitely with depth z.

After inclusion of the absorption effect, the $D_h(z)$ amplitude ceases to grow indefinitely, and a maximum appears for the compressed diffracted wave at a depth of

$$L_0 = \lambda/\pi a\delta_0, \qquad (12)$$

where $a = [\mathrm{Im}(\chi_0)/\delta_0^2]^{1/3}$ and λ is the radiation wavelength. The intensity of radiation field inside the crystal is

$$I(z, \Delta\theta, \varphi_0)$$
$$= \left| \sum_{j=1,2} (D_0^{(j)}(z) + D_h^{(j)}(z)) \exp\left[i\left(y_j + \frac{\kappa\chi_0}{2\varphi_0}\right)z\right] \right|^2. \qquad (13)$$

The calculated intensity distribution of X-rays inside the crystal is shown in Fig. 1 for the (220) reflection of characteristic GeK_α radiation from germanium crystal and the incident-wave direction corresponding to the "degenerate" point given by Eqs. (9) and (10). One can see from this figure that the incident beam is almost 300-fold compressed at a depth on the order of 30 nm. This phenomenon was experimentally observed using the X-ray standing-wave method for a Si single crystal cut at an angle of $\Psi = 8°$ to the (111) direction. In these experiments, the photoelectron yield from Si crystal was enhanced by more than 20 times for the (422) reflection [8]. This effect was later confirmed in experiments with a Ge crystal, where the photoelectron yield in the asymmetric diffraction scheme was more than tenfold higher than the radiation yield for incidence angles away from the Bragg angle [9].

The X-radiation intensity distribution within the Kossel line for the radiation source located inside the crystal can also be easily calculated by using Eqs. (1)–(8) and (13) and the reciprocity principle [11]. According to this principle, the distribution of radiation from the excited atoms in crystal is determined for the Kossel line by the equation

$$\bar{I}(\Delta\theta, \varphi) = \int_0^\infty I(z, \Delta\theta, \varphi)P(z)dz, \qquad (14)$$

where $P(z)$ is the depth distribution of radiating atoms in crystal.

Figure 2 presents the GeK_α radiation distribution within the Kossel line in a Ge crystal cut in the (110) direction. The calculation is carried out for the (022) reflection under the assumption that the excited radiating germanium atoms are concentrated near the surface with the exponential density

$$P(z) = e^{-z/L}, \qquad (15)$$

where the characteristic depth L of excited atoms in crystal is taken to be 50 nm. It is seen from this figure that the intensity distribution within the Kossel line has a pronounced peak, whose intensity is more than 100-fold higher than the background intensity. The diver-
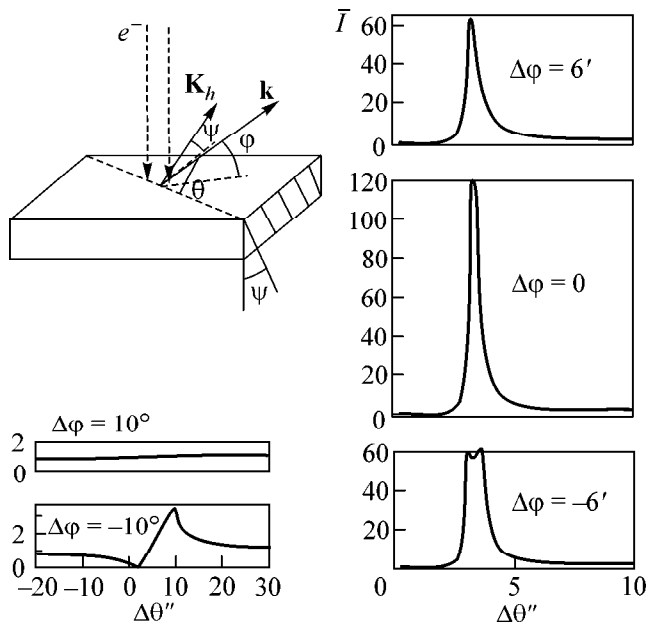
Fig. 2. Kossel diffraction in an extremely asymmetric diffraction scheme and the intensity distribution of the GeK_α radiation from a Ge crystal ($\Psi = 30°$), as calculated for the (220) reflection (right) in the vicinity of the degenerate point $\varphi = 1128' + \Delta\varphi$ and (left) far away from it in the Bragg ($\Delta\varphi = -10°$) and Laue ($\Delta\varphi = 10°$) geometries. The scale for the left curves is increased tenfold.

gence in the θ angle is as small as several seconds of arc and in the φ angle is tens of angular minutes. These are precisely the parameters which are achieved for a sharply collimated beam formed using multiple monochromators. The predicted effect can easily be observed with the use of such monochromators as an analyzer of the radiation distribution within the Kossel line.

Note that in the usual diffraction schemes, symmetric or slightly asymmetric, the Bragg geometry (see Fig. 2, $\Delta\varphi = -10°$) provides relatively small changes in the radiation intensity, and the distribution maximum only several times exceeds the background intensity. These variations are quite sufficient to fix the alternating light and black fringes (Kossel effect) on the photographic plate. With the Laue geometry (Fig. 2, $\Delta\varphi =$

10°), the changes in radiation intensity within the Kossel line are very weak, so that this geometry is rarely used.

Naturally, it remains to solve the problem of atomic excitation in a narrow near-surface layer. If the excitation is provided by an electron beam, this problem is solved through lowering the energy of incident electrons. In the case of an X-ray beam, this problem is solved by decreasing the angle of incidence of the exciting beam on the crystal. If the incident beam starts to suffer mirror reflection, the excitation of the Ge atoms, say, by the characteristic MoK_α radiation occurs at a depth on the order of 20 nm. Therefore, the experimental implementation of the idea seems not to be a challenge.

REFERENCES

1. J. M. Cowley, Acta Crystallogr. **17**, 33 (1964).
2. J. P. Hannon, N. J. Carron, and G. T. Trammel, Phys. Rev. B **9**, 2810 (1974).
3. J. T. Hutton, G. T. Trammel, and J. P. Hannon, Phys. Rev. B **31**, 743 (1985).
4. T. Gog, P. M. Len, G. Materlik, *et al.*, Phys. Rev. Lett. **76**, 3132 (1996).
5. B. Adams, T. Hiort, E. Kossel, *et al.*, Phys. Status Solidi B **215**, 757 (1999).
6. W. Kossel, V. Loeck, and H. Voges, Z. Phys. **94**, 139 (1935).
7. A. M. Afanas'ev and A. V. Esayan, Phys. Status Solidi A **126**, 303 (1991).
8. A. M. Afanas'ev, R. M. Imamov, É. Kh. Mukhamedzhanov, *et al.*, Fiz. Tverd. Tela (Leningrad) **32**, 650 (1990) [Sov. Phys. Solid State **32**, 383 (1990)].
9. A. M. Afanas'ev, R. M. Imamov, and É. Kh. Mukhamedzhanov, Kristallografiya **40**, 567 (1995) [Crystallogr. Rep. **40**, 521 (1995)].
10. N. Hertel, M. V. Kovalchuk, A. M. Afanas'ev, and R. M. Imamov, Phys. Lett. A **75A**, 501 (1980).
11. M. von Laue, *Roentgenstrahl-interferentzen* (Academische Verlagsgesellschaft, Frankfurt, 1960).

Translated by V. Sakun

Centrifugal-Dissipative Instability of Rossby Vortices and Their Cyclonic–Anticyclonic Asymmetry

S. G. Chefranov

Oboukhov Institute of Atmospheric Physics, Russian Academy of Sciences, Pyzhevskiĭ per. 3, Moscow, 109017 Russia

Institute of Fundamental Problems of Biology, Russian Academy of Sciences, Pushchino, Moscow region, 142292 Russia

A new linear centrifugal-dissipative mechanism is proposed that explains the vortex asymmetry observed, in particular, in the structure of low-frequency anticyclonic Rossby vortices. It is shown that the relevant centrifugal-dissipative instability, which spontaneously breaks the chiral symmetry of the vortices, takes place only in the range $\omega < \Omega$, where ω is the frequency of small oscillations corresponding to the effective solid-body rotation of a vortex and Ω is the rotation rate of a noninertial frame of reference. The onset of the instability is associated with the existence of an optimum magnitude of the frictional force. In the vortex model based on a two-dimensional oscillator with the natural frequency ω in a noninertial reference frame rotating at the rate Ω, the instability shows up as an exponential increase in the total angular momentum. It is noted that the centrifugal-dissipative instability may also manifest itself in the seismically active regions of the world. © *2001 MAIK "Nauka/Interperiodica".*

PACS numbers: 47.32.Cc; 47.20.-k

It is well known that fairly stable low-frequency (large-scale) vortices observed in the atmospheres of rapidly rotating planets (like Jupiter, Saturn, and Earth) are, as a rule, anticyclonic whirls; i.e., they usually rotate in the direction opposite to the direction of rotation of the planet [1]. The characteristic rate ω of the effective solid-body rotation of such vortices is always lower than the rotation rate Ω_p of a planet. Analogously, broken chiral symmetry dominated by anticyclonic circulations is characteristic of vortex lenses in the oceans [1] and vortices observed in laboratory experiments with liquids in rotating vessels [1–3]. These observations of broken chiral symmetry in nonequilibrium vortex systems supplement the well-known observations made since Louis Pasteur (1862) of the left–right spatial dissymmetry in objects of animate nature [4–6].

In the present-day nonlinear theory of Rossby vortices (see [1] and the literature cited therein), the chiral symmetry breaks due to the predominance of a certain type of nonlinearity. In this context, it is proposed to describe the centrifugal-dissipative instability (CDI) by a fundamentally new model that is based on a two-dimensional oscillator in a rotating noninertial reference frame. According to this model, the chiral symmetry of the developing low-frequency anticyclonic vortices is spontaneously broken by a linear mechanism for the CDI. The validity of this model is proved by the fact that exact vortex solutions to the hydrodynamic equations of an incompressible fluid can be adequately

described by solid-body rotations (including those on a spherical surface [7]) with the help of the equations of a two-dimensional oscillator. The proposed model of a two-dimensional oscillator in a rotating noninertial frame can also be used to describe other physical phenomena: from low-frequency ($\omega < \Omega_p$) large-scale seismically active geophysical wave processes to submolecular oscillators in the corresponding microsystems rotating at the rates $\Omega \gg \Omega_p$.

1. For simplicity, we start by considering a two-dimensional oscillator in the plane (x, y) in a coordinate system rotating at an arbitrary angular velocity Ω about the z axis. In spherical geometry, the vortices at an arbitrary latitude $\tilde{\varphi}_0$ will be described later [see formula (8)].

The problem as formulated is a generalization of the familiar classical problem [8] of how the Earth's rotation affects the small oscillations of a two-dimensional oscillator—the Foucault pendulum—in the corresponding rotating noninertial reference frame. In fact, according to [8], a mathematical Foucault pendulum of length l always satisfies the relationship $\omega = \sqrt{g/l} \gg \Omega_p \simeq 10^{-5}\,\text{s}^{-1}$, so that the centrifugal acceleration, which is proportional to $O(\Omega_p^2)$, can definitely be neglected (as is the case in [8]). On the other hand, the centrifugal acceleration should be taken into account when analyzing other kinds of oscillations, specifically, those at low frequencies $\omega < \Omega_p$. With allowance for the frictional

force, which is proportional to velocity (the proportionality coefficient being α), the equation of motion for a two-dimensional oscillator in the frame of reference rotating at a constant angular speed Ω has the form

$$\ddot{\xi} + 2\dot{\xi}(\alpha + i\Omega) + (\omega^2 - \Omega^2)\xi = 0, \qquad (1)$$

where $\xi \equiv x + iy \equiv r\exp(i\varphi)$, $\dot{\xi} \equiv d\xi/dt$, and $\alpha > 0$. In particular, in an inertial frame, Eq. (1) with $\alpha = \Omega = 0$ describes the solid-body rotation (at the rate ω) of the cores of different types of vortices [1, 7]. The solution to Eq. (1) is

$$\xi = C_1 \exp[\tau\beta_+(\tilde{\alpha}, \tilde{\omega})] + C_2 \exp[-\tau\beta_-(\tilde{\alpha}, \tilde{\omega})], \quad (2)$$

where $C_\alpha = \text{const}$ ($\alpha = 1, 2$), $\tau \equiv t\Omega$, $\tilde{\alpha} \equiv \alpha^2/\Omega^2$, and

$$\tilde{\omega} \equiv \omega^2/\Omega^2, \quad \beta_\pm = \lambda_0(\tilde{\alpha}, \tilde{\omega}) \mp \sqrt{\tilde{\alpha}} + i\left(\frac{\sqrt{\tilde{\alpha}}}{\lambda_0} \mp 1\right),$$

$$\lambda_0 = \left[\frac{\tilde{\alpha} - \tilde{\omega} + \sqrt{(\tilde{\alpha} - \tilde{\omega})^2 + 4\tilde{\alpha}}}{2}\right]^{1/2}.$$

Obviously, solution (2) implies that the zero equilibrium state ($x = 0$, $y = 0$) of the system described by Eq. (1) possesses chiral symmetry and is unstable against arbitrarily small seed perturbations such that $\tilde{\omega} < 1$, in which case the quantity λ_0 in solution (2) satisfies the condition

$$\lambda_0(\tilde{\alpha}, \tilde{\omega}) > \sqrt{\tilde{\alpha}}. \qquad (3)$$

The unstable state ($x = 0$, $y = 0$) corresponds to an unstable focal point, and, for arbitrary chirally symmetric initial conditions, circulation along the trajectories in the (x, y) plane under the condition $\tau \gg 1$ is anticyclonic; i.e., the circulation direction is opposite to the direction of rotation of the reference frame (with the angular speed Ω). In fact, for $\tau \gg 1$, which indicates that the first term on the right-hand side of solution (2) dominates over the second term, condition (3) implies that the circulation frequency $\dot{\varphi}$ (which is generally different from the frequency ω of the seed perturbations) is equal to

$$\dot{\varphi} = -\Omega(1 - \sqrt{\tilde{\alpha}}/\lambda_0) \qquad (4)$$

and satisfies the inequality $|\dot{\varphi}| < \Omega$ by virtue of $(\lambda_0 - \sqrt{\tilde{\alpha}})/\lambda_0 < 1$. Under condition (3), the frequencies $\dot{\varphi}$ and Ω in Eq. (4) have opposite signs. The most unstable perturbation mode is that with $\omega = 0$, for which the quantity λ_0 is maximum. From solution (2) and condition (3), one can see that the seed perturbations are unstable only when $\alpha \neq 0$, in which case the solution ξ

increases exponentially with time. In particular, we have

$$\lambda_0 - \sqrt{\tilde{\alpha}}$$

$$= \begin{cases} \sqrt{\tilde{\alpha}/\tilde{\omega}}(1 - \sqrt{\tilde{\omega}}) + O((\tilde{\alpha}/\tilde{\omega})^{3/2}), & \tilde{\alpha} \ll \tilde{\omega} \\ \sqrt{\tilde{\alpha}}\left[\left(\frac{1 + \sqrt{1 + 4/\tilde{\alpha}}}{2}\right)^{1/2}\right. \\ \left. \times\left(1 - \frac{\tilde{\omega}}{2\tilde{\alpha}\sqrt{1 + 4/\tilde{\alpha}}} + O\left(\frac{\tilde{\omega}^2}{\tilde{\alpha}^2}\right)\right) - 1\right], & \tilde{\alpha} \gg \tilde{\omega} \\ \frac{1}{2\sqrt{\tilde{\alpha}}}[1 - \tilde{\omega} + O(\tilde{\omega}/\tilde{\alpha})], & \tilde{\alpha} \gg \tilde{\omega}, \quad \tilde{\alpha} \gg 1 \\ \tilde{\alpha}^{1/4} + O(\tilde{\alpha}^{1/2}), & \tilde{\alpha} \gg \tilde{\omega}, \quad \tilde{\alpha} \ll 1. \end{cases} \quad (5)$$

Although the general case is that with $|\dot{\varphi}| \neq \omega$, it is of interest to consider the main frequency-demultiplication resonance $\omega = \Omega/2$. Taking the limit $\tilde{\alpha} \ll \tilde{\omega}$, we can see that formulas (4) and (5) give the equality $|\dot{\varphi}| = \omega$, which is valid for the unstable state ($x = 0$, $y = 0$) under condition (3). As in the case of parametric resonance [8], solution (2) and condition (3) imply that, for the dissipative vibrating system (1), it is precisely the modes with $\omega \simeq \Omega/2$ that grow exponentially in time.[1] On the other hand, for $\omega \simeq \Omega/2$, we have $|\dot{\varphi}| \leq \omega$.

Hence, in order for the chirally symmetric state to be linearly unstable in the range $\tilde{\omega} < 1$, the dissipation in the system should be finite. This stems from the fact that the quantity $\lambda_0 - \sqrt{\tilde{\alpha}}$ approaches zero in both limits $\tilde{\alpha} \longrightarrow 0$ and $\tilde{\alpha} \longrightarrow \infty$. Note also that, regardless of the values of $\tilde{\omega}$ and $\tilde{\alpha}$, each solution to Eq. (1) in which the centrifugal force is neglected describes a damped Foucault pendulum [8]. For these reasons, the instability in question is actually of centrifugal-dissipative origin. According to the approximate expressions (5) for the dependence of $\lambda_0 - \sqrt{\tilde{\alpha}}$ on $\tilde{\alpha}$, there is an optimum rate of dissipation $\tilde{\alpha} = \tilde{\alpha}_0(\tilde{\omega})$ at which the quantity $\lambda_0 - \sqrt{\tilde{\alpha}}$ is maximum. In particular, for $\tilde{\omega} = 0$, we have $\sqrt{\tilde{\alpha}_0} \simeq 0.49$; for $\tilde{\omega} = 1/3$, we have $\sqrt{\tilde{\alpha}_0} \simeq 0.405$; and for $\tilde{\omega} \longrightarrow 1$, we have $\tilde{\alpha}_0 \longrightarrow 0$, so that $\sqrt{\tilde{\alpha}_0} \simeq 3(1 - \tilde{\omega})$. In other words, the quantity $\tilde{\alpha}_0$ decreases as $\tilde{\omega}$ increases from zero to unity.

The above-described dissipative effects, which play an important role in triggering the instability that drives

---

[1] However, in contrast to the case of parametric resonance, solution (2) and condition (3) imply that not only the mode with $\omega = \Omega/2$ grows exponentially with time but also all modes with $\omega < \Omega$ are unstable. In addition, in the case at hand, the instability is associated precisely with the effects of the frictional force, while parametric resonance can also occur for $\alpha = 0$ [8].

the anticyclonic circulation of particles in a rotating frame of reference, may also manifest themselves in any rotating noninertial system, i.e., in the system that initially has no chiral symmetry.

This conclusion is supported, e.g., by the following two examples. First, let us mention the Andronikashvili central vortex that arises in a rotating He I during the transition into the superfluid phase (into He II) and is in fact observed to dissipate gradually immediately after the transition, while detaching itself from the bottom of a rotating vessel and becoming progressively lower in height [9]. Also, Chkhetiani and Moiseev [10] showed that, in a medium in which the mean chirality of a small-scale electromagnetic field is nonzero (in particular, because of the left–right spatial dissymmetry of molecules), the possible exponential increase in the magnetic field may stem, among other things, from a finite dissipation in the low-conductivity limit.

If we consider Eq. (1) with $\alpha = \nu k^2/2$ (where ν is the kinematic viscosity) as a linearized approximation to the hydrodynamic equations, then the quantity $\tilde{\alpha}_0$ corresponds to the most unstable mode with $k \simeq k_0 \equiv (2\tilde{\alpha}_0^{1/2}\Omega/\nu)^{1/2}$, i.e., the mode whose amplitude grows exponentially in time at the highest rate.

2. In order to provide a clearer insight into the physics of the CDI of a chirally symmetric state, we can turn to the corresponding representations of the total energy and total angular momentum in rotating and nonrotating (immobile) reference frames [8] and of their time derivatives at $\alpha \neq 0$. It turns out that, during the onset of the CDI, the angular momentum is not an invariant of motion (as is definitely the case with Eq. (1) at $\alpha \neq 0$) but can increase exponentially in time, as can be inferred from the equation $\dot{M}_z = -2\alpha r^2\dot{\phi}$ for the angular momentum component of a unit mass rotating about the z axis orthogonal to the (x, y) plane. Under condition (3) with $\tilde{\omega} < 0$, relationship (4) gives $\dot{\phi} < 0$ and solution (2) yields $r = r_0\exp[\tau(\lambda_0 - \sqrt{\tilde{\alpha}})]$, so that we have $M_z = r^2(\dot{\phi} + \Omega) > 0$ [see formula (4)]. Note also that the quantity $M_z/2\pi$ describes the vortex circulation of the velocity field **v** of an incompressible fluid in the (x, y) plane in the reference frame rotating at the rate Ω.

In order to obtain equations for the total energy, we supplement Eq. (1) with the equation for oscillations along the z axis,

$$\ddot{z} + 2\alpha\dot{z} + \omega^2 z = 0, \qquad (6)$$

and consider a rotating frame of reference such that $\dot{\Omega} \neq 0$, in which case we must add the term $-i\dot{\Omega}\xi$ to the right-hand side of Eq. (1). As a result, Eqs. (1) and (6) yield the following equations for the total energy E_n per unit mass in a rotating noninertial reference frame and the total energy E_0 in the corresponding immobile (non-

rotating) frame [8] (these energies are related to each other as $E_0 = E_n + (\mathbf{\Omega} \cdot \mathbf{M})$):

$$\begin{aligned}
\dot{E}_0 &= -2\alpha[\dot{z}^2 + \dot{r}^2 + r^2\dot{\phi}(\Omega + \dot{\phi})], \\
\dot{E}_n &= -2\alpha(\dot{z}^2 + \dot{r}^2 + r^2\dot{\phi}^2) - \dot{\Omega}M_z,
\end{aligned} \qquad (7)$$

where $\dot{E}_0 > 0$, provided that the CDI occurs, i.e., that inequality (3) and the condition $0 < \tilde{\omega} < 1$, which is imposed by this inequality on $\tilde{\omega}$, are both satisfied.

Hence, during the onset of the CDI under condition (3), the total energy E_0 can increase at the expense of the energy that maintains the circulation at a constant rate (4) and is associated with the increase in the angular momentum M_z resulting from dissipative forces with $\alpha > 0$.

3. In geophysics, the above-described mechanism for transforming the rotational energy of the Earth, together with the energy-related phenomena resulting from both nonuniform (in latitude) mean heat balance and other local manifestations of the nonuniform insolation [11], may be responsible for the formation of large-scale vortex structures in the atmosphere and the oceans. The above analysis is also applicable to some other problems. In particular, in Newtonian mechanics, the model developed here can be used to explain the principles of operation of the actual mechanical devices aimed at converting the energy of the inertial forces of rotational motions [including those at a rate $\dot{\Omega} \neq 0$; see Eqs. (7)] into the energy of translational motion [12, 13]. The above model can also provide a new insight into the experimentally observed asymmetry of the chemical reactions in rotating vessels [5, 14] (in the context of looking for physical causes for deracemization of the biological objects [4–6]). However, these problems, as well as the problems of the formation of vortex structures and the problems of intermediacy and turbulent diffusion [15], in which the CDI can also play an important role, require a separate study, so that we restrict ourselves here to discussing some possible geophysical consequences of the CDI.

Indeed, Eq. (1) and the above analysis can be simply generalized to geophysical systems on a rotating sphere. Thus, if we apply the f-plane approximation [11] but choose a coordinate system with the z axis directed parallel to the rotation axis of the sphere (the z axis is aligned with the direction of the normal to the sphere only at the pole), then we arrive at Eq. (1), which should be supplemented with Eq. (6) for oscillations along the z axis. The remaining coordinates of this system are as follows. The x coordinate corresponds [11] to the distance toward the east in the zonal direction along the axis lying in the tangent plane to the sphere at the latitude $\tilde{\phi} = \tilde{\phi}_0$ and at a fixed longitude. The y and z coordinates are related to the y' and z' coordinates that are traditionally introduced in the f plane (the y' axis is

directed northward in a meridional plane, and the z'-axis coincides with a local normal to the sphere) [11] by

$$z = y'\cos\tilde{\varphi}_0 + z'\sin\tilde{\varphi}_0, \quad y = y'\sin\tilde{\varphi}_0 - z'\cos\tilde{\varphi}_0; \quad (8)$$

these relationships correspond to the rotation of the (x, y', z') coordinates through the angle $\pi/2 - \tilde{\varphi}_0$ about the x axis in a poleward direction. Equations (1) and (6) can be regarded, in particular, as a linearized form of the hydrodynamic equations for Lagrangian particles on a sphere in the f-plane approximation, with the representations $\nu\Delta\mathbf{v} \simeq -2\alpha\mathbf{v}$ and $\nabla p/\rho_0 - \omega^2\mathbf{x}$, where ∇p is the pressure gradient and Δ is the Laplacian operator. In this case, the solution for x, y, and z coincides with the above solution to Eqs. (1) and (6) and, under condition (3) (i.e., for $\tilde{\omega} < 1$), describes anticyclonic [see formula (4)] circulation of liquid particles about the z axis, which is inclined at an angle $\tilde{\varphi}_0$ to the tangent plane. Consequently, in the plane perpendicular to the tangent plane, the particle trajectories are ellipses (rather than circles, as is the case in the plane parallel to the z axis) with their minor axes in the meridional direction. In fact, in laboratory experiments on modeling Rossby vortices in a rotating parabolic vessel, the photographs taken precisely in the direction parallel to the vessel's rotation axis show that the passive particles, which visualize a vortex, move along circles [1]. The above analysis of Eq. (1) with $\tilde{\omega} < 1$ shows that, under the condition $\tau \gg 1$, the CDI drives liquid particles only into anticyclonic circulation. This conclusion agrees with the observations according to which long-lived anticyclones predominate in the atmospheres of rapidly rotating large planets (such as the Earth, Jupiter, and Saturn), whose rotation rate Ω_p is much higher than the anticyclonic circulation rate ω [1].

Thus, Jupiter's Great Red Spot, which has survived at least 300 years, is an oval-shaped huge anticyclone, which drifts westward at a mean speed of about 3.5 m/s, is centered at about latitude $\tilde{\varphi}_0 \approx -22°$, and is flattened in the meridional direction (according to the *Voyager* photographs of Jupiter).

In fact, with allowance for the dependence of the Coriolis parameter $f = 2\Omega\sin\tilde{\varphi}$ on the latitude $\tilde{\varphi}$, the solution of hydrodynamic equations on a sphere in the inertial wind approximation (for a zero pressure gradient in the horizontal direction) shows that liquid particles should inevitably experience anticyclonic circulation: the particles move along trochoids that are, on average, deflected westward (see [11]). In order to incorporate the β effect [$\tilde{\varphi} \simeq \tilde{\varphi}_0 + y'/R + o(y'R)$] into the above model of the CDI of Rossby vortices circulating at rate (4) in the case $\tau \gg 1$, the right-hand side of Eq. (1) for ξ should be supplemented with the term $(2\Omega/R)\sin\tilde{\varphi}_0[\dot{z}y + \dot{y}z + i(\dot{x}z - \dot{z}\dot{y}/\Omega)]$, where R is the radius of a sphere rotating at an angular speed Ω. Applying the method of successive approximations in

the small parameter $r/R \ll 1$ [i.e., substituting the solutions obtained in the f-plane approximation into the right-hand side of Eq. (1)], we can derive the following estimate for the mean velocity of a vortex that drifts westward in the zonal direction for $\tilde{\omega} \ll 1$, $\tau \gg 1$, and $\tilde{\alpha} \ll 1$:

$$\langle \bar{v}_x \rangle \simeq -\frac{\sin^2\tilde{\varphi}_0\cos\tilde{\varphi}_0}{\omega R}\langle v_{0y'}^2 \rangle, \quad (9)$$

where the root-mean-square initial speed $\langle v_{0y'}^2 \rangle^{1/2}$ in the meridional direction corresponds to the vortex circulation at the rate $\dot{\varphi} = \omega$, the angular brackets indicate statistical averaging over the initial conditions such that $\langle v_{0y'} \rangle = 0$, and the overbar stands for averaging over the period of circulation $2\pi/\Omega$. With the parameter values characteristic of Jupiter and its Great Red Spot ($\Omega \simeq 10^{-4}$ s^{-1}, $\omega \simeq 10^{-5}$ s^{-1}, $\langle v_{0y'}^2 \rangle^{1/2} \simeq 10^2$ m/s, and $R = 700000$ km), relationship (9) yields the estimate $\langle \bar{v}_x \rangle \simeq -2$ m/s, which agrees well with the above-mentioned value of the observed velocity of the westerly drifting Great Red Spot, $\bar{v}_x \simeq -(3.4–3.8)$ m/s.

It would be worthwhile to study the effect of the nonlinear drift described by the nonlinear terms in the expansion $\nabla p/\rho_0 = \omega\mathbf{x}(1 + O(|\mathbf{x}|)\ldots)$ and to compare the CDI of a chirally symmetric vortex state with the diffusive [16] and stochastic [17] instabilities of a spatially uniform state, which result in the formation of nonuniform structures.

In conclusion, let us estimate the conditions under which the CDI plays the role of a possible driving force for seismic activity in the Earth's crust and in the upper mantle in the form of seismic waves whose frequencies are sufficiently low, $\omega < \Omega_p \simeq 10^{-5}$ s^{-1} [see condition (3)], and which are associated with the Earth's rotation and with the existence of the optimum dissipation rate for the onset of the CDI. We assume that free small-amplitude waves of the Earth's crust satisfy the same dispersion relation as the flexural waves of a plate of thickness h, $\omega = c_0h/\lambda^2$ (see formulas (25) and (8) in [18]), where $c_0 \simeq 6$ km/s is the speed of the longitudinal waves and λ is the wavelength or, equivalently, the characteristic horizontal length scale of the process. Condition (3) for the onset of the CDI such that $\omega < \Omega_p$ yields the estimate $\lambda > \lambda_{cr} = \sqrt{hc_0/\Omega_p} \simeq 2500$ km of the actual horizontal characteristic scale length of seismically active zones. In contrast to an isotropic medium, in which the critical wavelength λ_{cr} is two orders of magnitude longer ($\lambda_{cr} \simeq c_0/\Omega_p$), this estimate agrees fairly well with the observed period (of about 3000 km) of large-scale lithospheric magnetic anomalies of unknown origin, as well as with the actually observed effects of rotation of the contraction axes near the focus of an impending severe earthquake [19].

REFERENCES

1. M. V. Nezlin and E. N. Snezhkin, *Rossby Vortexes and Spiral Structures* (Nauka, Moscow, 1990).

2. B. M. Bubnov and H. J. Fernando, Izv. Akad. Nauk, Fiz. Atmos. Okeana **35**, 487 (1999).

3. V. F. Tarasov and V. G. Makarenko, Dokl. Akad. Nauk SSSR **305**, 297 (1989) [Sov. Phys. Dokl. **34**, 199 (1989)].

4. B. Ya. Zel'dovich, D. B. Saakyan, and I. I. Sobel'man, Pis'ma Zh. Éksp. Teor. Fiz. **25**, 106 (1977) [JETP Lett. **25**, 94 (1977)].

5. V. I. Gol'danskiĭ and V. A. Kuz'min, Usp. Fiz. Nauk **157**, 3 (1989) [Sov. Phys. Usp. **32**, 1 (1989)].

6. A. S. Presman, *Organization of Biosphere and Its Cosmic Relations* (Nauka, Moscow, 1997).

7. S. G. Chefranov, Izv. Akad. Nauk SSSR, Fiz. Atmos. Okeana **21**, 1026 (1985).

8. L. D. Landau and E. M. Lifshitz, *Mechanics* (Nauka, Moscow, 1982; Pergamon, New York, 1988).

9. Dzh. S. Tsakadze, Zh. Éksp. Teor. Fiz. **44**, 105 (1963) [Sov. Phys. JETP **17**, 72 (1963)].

10. O. G. Chkhetiani and S. S. Moiseev, Pis'ma Zh. Éksp. Teor. Fiz. **70**, 268 (1999) [JETP Lett. **70**, 277 (1999)].

11. G. J. Haltiner and F. L. Martin, *Dynamical and Physical Meteorology* (McGraw-Hill, New York, 1957; Nauka, Moscow, 1960).

12. N. Dean, US Patent No. 2886, 976, class 74-112 (1959).

13. V. I. Tolchin, *Inertioid and Inertial Forces as Source of Motion* (Perm, 1977).

14. R. C. Dougherty, D. Edwards, and K. Cooper, J. Am. Chem. Soc. **102**, 381 (1980); **102**, 730 (1980).

15. S. G. Chefranov, Zh. Éksp. Teor. Fiz. **108**, 2010 (1995) [JETP **81**, 1096 (1995)].

16. G. Nicolis and I. Prigogine, *Self-Organization in Nonequilibrium Systems* (Wiley, New York, 1977; Mir, Moscow, 1979).

17. S. G. Chefranov, Izv. Vyssh. Uchebn. Zaved., Radiofiz. **28**, 1516 (1985).

18. L. D. Landau and E. M. Lifshitz, *Theory of Elasticity* (Nauka, Moscow, 1987; Pergamon, New York, 1986).

19. M. A. Sadovskiĭ, I. L. Nersesov, *et al.*, Tectonophysics **14**, 295 (1972).

Translated by G. Shepekina

Spiral-Logarithmic Structures in a Heisenberg Ferromagnet

E. Sh. Gutshabash

Institute of Physics (Petrodvorets Branch), St. Petersburg State University,
ul. Ulyanovskaya 1, Petrodvorets, 198504 Russia
* e-mail: gutshab@EG2097.spb.edu
Received February 7, 2001

Spiral-logarithmic structure is suggested as a stationary solution of a modified equation for the Heisenberg model, and the single- and N-soliton solutions are constructed on this base. © *2001 MAIK "Nauka/Interperiodica".*

PACS numbers: 75.10.-b

Spiral (incommensurate) structures in ferromagnets have long been studied and are well understood [1, 2]. They are formed due to the reconstruction of a Fermi surface as a result of the interaction of magnetic moments with conduction electrons.[1] Mathematically, they were used in the context of the inverse scattering problem, e.g., as boundary conditions when solving the nonlinear $(2 + 0)$-dimensional $O(3)$-sigma model (two-dimensional stationary Heisenberg ferromagnet) [4].

In this work, a special model is invoked to demonstrate theoretically that new magnetic structures can exist which may naturally be called spiral-logarithmic structures.

Let us consider cylindrically symmetric configurations in the model of a "modified" Heisenberg magnet [5]:

$$\mathbf{S}_t = \mathbf{S} \times \left(\mathbf{S}_{xx} + \frac{1}{x}\mathbf{S}_x\right), \qquad (1)$$

where $\mathbf{S}(x, t) = (S_1, S_2, S_3)$ is the magnetization vector ($\mathbf{S}^2 = 1$) and $x = \sqrt{x_1^2 + x_2^2}$, where x_1 and x_2 are the Cartesian coordinates on a plane. The Cauchy problem for Eq. (1) was solved in [5] by the inverse scattering method on a trivial background, and it was shown that any perturbation localized at $t = 0$ spreads out.

However, one can readily verify by a direct calculation that the vector $\mathbf{S} = \mathbf{S}^{(1)}$ with components

$$\begin{aligned} S_1^{(1)}(x) &= \sin(\ln x + \theta_0), \\ S_2^{(1)}(x) &= \cos(\ln x + \theta_0), \quad S_3^{(1)}(x) = 0, \end{aligned} \qquad (2)$$

where $\theta_0 \in \mathbb{R}$ is a constant and $x > 0$, is also a (stationary) solution of Eq. (1). Now, using the fact that this equation is quite solvable, let us construct its exact solutions on the background of structure (2). To this

end, let us represent Eq. (1) in the form of a condition for compatibility of the following linear matrix system:

$$\Psi_x = U_1 \Psi \Lambda, \quad \Psi_t = V_1 \Psi \Lambda + V_2 \Psi \Lambda^2, \qquad (3)$$

where $U_1 = -(i/2)S$, $V_1 = (1/2)S_x S + i(AS + SA)$, $V_2 = (i/2)S$, $S = \sum_{i=1}^{i=3} S_i \sigma_i$, σ_i are the Pauli matrices, $\Lambda = \mathrm{diag}(\lambda, \bar{\lambda})$, $\lambda \in \mathbb{C}$ is a parameter, matrix $A = A(S)$ is determined from the condition

$$[A(S)S + SA(S)]_x = -\frac{1}{4ix}[S, S_x], \qquad (4)$$

and it is additionally assumed that the elements of the matrix $(S - S^{(1)})$ properly decrease at $x \longrightarrow \infty$.

Equation (1) will be solved by the Darboux matrix-transformation method [6]. Let

$$\tilde{\Psi} = \Psi - L_1 \Psi \Lambda, \qquad (5)$$

where $L_1 = \Psi_1 \Lambda_1^{-1} \Psi_1^{-1}$ and Ψ_1 is a certain fixed solution of Eqs. (3) corresponding to the choice $\mathbf{S} = \mathbf{S}^{(1)}$ and $\lambda = \lambda_1$.

Checking for the covariance of system (3) about transformation (5) yields the dressing relations ($U_1 = -(i/2)S^{(1)}$)

$$\tilde{U}_1 = L_1 U_L L_1^{-1}, \quad \tilde{U}_1 = U_1 - L_{1x}, \qquad (6)$$

$$\tilde{V}_2 = L_1 V_2 L_1^{-1}, \quad \tilde{V}_1 = V_1 - L_{1t}, \qquad (7)$$
$$\tilde{V}_2 = V_2 - L_1 V_1 + \tilde{V}_1 L_1.$$

The equivalence of all these expressions can be proved by simple mathematics. The second relation in Eqs. (6) can be conveniently rewritten as

$$\tilde{U}_1 = U_1 - \Psi_1 [\Psi_1^{-1} \Psi_{1x}, \Lambda_1^{-1}] \Psi_1^{-1}. \qquad (8)$$

---

[1] The spiral structures in non-Abelian gauge theories are discussed in recent publication [3].

From the property $\sigma_2 S \sigma_2 = -\bar{S}$ of matrix S, one has $\sigma_2 U_1 \sigma_2 = \bar{U}_1$. The matrix Ψ_1 then takes the form

$$\Psi_1 = \begin{pmatrix} \varphi_1 & -\bar{\chi}_1 \\ \chi_1 & \bar{\varphi}_1 \end{pmatrix}, \tag{9}$$

where $\varphi_1 = \varphi_1(x, t, \lambda_1)$ and $\chi_1 = \chi_1(x, t, \lambda_1)$ are complex functions to be determined.

The A matrix in Eq. (4) must satisfy the condition $\mathrm{Tr}(AS + SA) = g(t)$ for any S, where $g(t)$ is an arbitrary function [in what follows, $g(t) = 0$]. Furthermore, considering that $\sigma_2 S S_x \sigma_2 = \bar{S} \bar{S}_x$ and using Eq. (4), one obtains $\bar{A} = \sigma_2 A \sigma_2$. It can easily be seen that Eq. (1) and the right-hand side of Eq. (4) are invariant about the substitution $S \longrightarrow S^{(f)} = S + f(x)I$, where $f(x)$ is an arbitrary complex function and I is 2×2 unit matrix. By setting $A(S) = (a_{ij}(S))$ and using condition (2), let us bring Eq. (4) to the form $\mathrm{diag}((2ia_{11}^0(S^{(f)})f)_x,$ $-(2ia_{11}^0(S^{(f)})f)_x) = \mathrm{diag}(1/2x^2, -1/2x^2)$, where $a_{11}(S^{(f)}) = ia_{11}^0(S^{(f)})$, $a_{11}^0 = \bar{a}_{11}^0$, and the $a_{21}(S^{(f)})$ element is zero. Hence it follows that $f(x) = i/4x$ and $a_{11}^0 = 1$; one also has $A(S^{(f)})S^{(f)} + S^{(f)}A(S^{(f)}) = A(S)S + SA(S)$, so that all properties of the matrix S are retained in the final formulas.

To construct the explicit solutions, note that on bare solution (2) the system of Eqs. (3) transforms, with regard to Eq. (4), into the following system of scalar equations ($\theta = \ln x + \theta_0$):

$$\varphi_{1x} = -\frac{1}{2}\lambda_1 e^{i\theta}\chi_1, \quad \chi_{1x} = \frac{1}{2}\lambda_1 e^{-i\theta}\varphi_1,$$

$$\varphi_{1t} = -\frac{1}{2}\lambda_1^2 e^{i\theta}\chi_1, \quad \chi_{1t} = \frac{1}{2}\lambda_1^2 e^{-i\theta}\varphi_1. \tag{10}$$

It follows from Eq. (10) that

$$\varphi_{1t} - \lambda_1\varphi_{1x} = 0, \quad \chi_{1t} - \lambda_1\chi_{1x} = 0. \tag{11}$$

Therefore, $\varphi_1(x, t) = F(x + \lambda_1 t)$ and $\chi_1(x, t) = G(x + \lambda_1 t)$, where functions F and G are constant on the characteristic $x + \lambda_1 t = \mathrm{const}$. They can be found by solving the system of Eqs. (10), e.g., for $t = 0$. The corresponding equation for $\varphi_1(x, 0)$ is reduced to

$$x\varphi_{1xx} - i\varphi_{1x} + \frac{1}{4}\lambda_1^2\varphi_1 = 0. \tag{12}$$

The solution to this equation is [7] $\varphi_1(x, 0) = x^{i/2 + 1/2}Z_{i/2 + 1/2}(-\lambda_1 x/2)$, where $Z_\nu(s) = C_1 I_\nu(s) + C_2 Y_\nu(s)$; I_ν and Y_ν are Bessel functions of the first and second kind, respectively; and C_1 and C_2 are arbitrary constants. The requirement that the solution be finite at

zero gives $C_2 = 0$. Then, the solution to the system of Eqs. (10) takes the form

$$\varphi_1(x, t) = C_1 q^{i/2 + 1/2}I_{i/2 + 1/2}\left(-\frac{\lambda_1}{2}q\right),$$

$$\chi_1(x, t) \tag{13}$$

$$= -\frac{2}{\lambda_1}C_1 e^{-i\theta(x, t)}\frac{\partial}{\partial x}\left[q^{i/2 + 1/2}I_{i/2 + 1/2}\left(-\frac{\lambda_1}{2}q\right)\right],$$

where $q = q(x, t) = x + \lambda_1 t - x_0$, $\theta(x, t) = \ln q + \theta_0$, and x_0 is the initial point.

One can now construct the simplest one-soliton solution. Nevertheless, it is still rather cumbersome, so that it is pertinent to use Eq. (8) and write the solution in the form[2] ($S_+ = S_1 + iS_2$ and $S_+[1] \equiv \tilde{S}_+$):

$$S_+[1](x, t) = ie^{-i\theta}$$

$$- \frac{4\lambda_{1I}\rho_1[(\ln\rho_1)_x - |\rho_1|^2(\ln\bar{\rho}_1)_x]}{|\lambda_1|^2(1 + |\rho_1|^2)^2}, \tag{14}$$

$$S_3[1](x, t) = \frac{8\lambda_{1I}|\rho_1|^2\mathrm{Re}(\ln\rho_1)_x}{|\lambda_1|^2(1 + |\rho_1|^2)^2},$$

where[3]

$$\rho_1 = \rho_1(x, t) = \chi_1/\varphi_1$$

$$= -(2/\lambda_1)e^{-i\theta(x, t)}\{\ln[q^{(i+2)/2}I_{(i+2)/2}(-\lambda_1 q/2)]\}_x.$$

This solution is nonsingular. It depends on four parameters λ_{1R}, λ_{1I}, x_0, and θ_0, where $\lambda_1 = \lambda_{1R} + i\lambda_{1I}$, and includes a single complex function $\rho_1(x, t)$. Note also that the spectrum of excitations in model (1) contains satellites of the "fundamental harmonic" with an incommensurate (and variable) "frequency." By using the asymptotic form of the Bessel function, one can show that solution (14) converges to Eq. (2) at $x \longrightarrow \infty$.

Let now obtain the N-soliton solution. For this purpose, let us use Eq. (5). One can easily show that

$$\Psi[N] = \Psi - Q_1\Psi\Lambda - \ldots - Q_N\Lambda^N, \tag{15}$$

with the matrix functions $Q_1, \ldots, Q_N$ being determined from the linear matrix system of equations

$$\Psi_1 - Q_1\Psi_1\Lambda_1^2 - \ldots - Q_N\Psi_1\Lambda_1^N = 0,$$

$$\Psi_2 - Q_1\Psi_2\Lambda_2^2 - \ldots - Q_N\Psi_2\Lambda_2^N = 0,$$

$$\ldots\ldots\ldots \tag{16}$$

---

[2] It is more convenient to use the matrix $\Psi_1\sigma_3$ instead of Ψ_1 [it is also a solution of system (3)].

[3] In this expression, as also in Eqs. (13) and (14), the logarithms are taken on their major branches and the appropriate cuts on the plane of parameter $\lambda \in \mathbb{C}$ are assumed to be made to provide solution uniqueness.

$$\Psi_N - Q_1\Psi_N\Lambda_N^2 - \ldots - Q_N\Psi_N\Lambda_N^N = 0,$$

where $\Lambda_i = \mathrm{diag}(\lambda_i, \bar{\lambda}_i)$; $i = 1, \ldots, N$; and Ψ_i are the solutions to Eq. (3) corresponding to $\lambda = \lambda_i$. At the same time, one has from Eq. (8)

$$U_1[N] = U_1 - \sum_{i=1}^{N} L_{ix} = U_1 - Q_{1x}. \qquad (17)$$

The expression for the N-soliton solution can readily be obtained from Eqs. (16) and (17):

$$S_3[N] = 1 - 2i(\Delta_1/\Delta)_x,$$
$$S_+[N] = -2i(\Delta_2/\Delta)_x, \qquad (18)$$

where $S_+[N] = S_1[N] + iS_2[N]$,

$$\Delta = \begin{vmatrix} \lambda_1\varphi_1 & \lambda_1\chi_1 & \lambda_1^2\varphi_1 & \lambda_1^2\chi_1 & \ldots & \lambda_1^N\varphi_1 & \lambda_1^N\chi_1 \\ -\bar{\lambda}_1\bar{\chi}_1 & \bar{\lambda}_1\bar{\varphi}_1 & -\bar{\lambda}_1^2\bar{\chi}_1 & \bar{\lambda}_1^2\bar{\varphi}_1 & \ldots & -\bar{\lambda}_1^N\bar{\chi}_1 & \bar{\lambda}_1^N\bar{\varphi}_1 \\ \ldots & \ldots & \ldots & \ldots & \ldots & \ldots & \ldots \\ \lambda_N\varphi_N & \lambda_N\chi_N & \lambda_N^2\varphi_N & \lambda_N^2\chi_N & \ldots & \lambda_N^N\varphi_N & \lambda_N^N\chi_N \\ -\bar{\lambda}_N\bar{\chi}_N & \bar{\lambda}_N\bar{\varphi}_N & -\bar{\lambda}_N^2\bar{\chi}_N & \bar{\lambda}_N^2\bar{\varphi}_N & \ldots & -\bar{\lambda}_N^N\bar{\chi}_N & \bar{\lambda}_N^N\bar{\varphi}_N \end{vmatrix},$$

and Δ_1 and Δ_2 are obtained by replacing the first and second columns in the determinant Δ by $(\varphi_1, -\chi_1, \ldots\varphi_N, -\chi_N)^T$ and $(\chi_1, \bar{\varphi}_1, \ldots\chi_N, \bar{\varphi}_N)^T$, respectively. The fact that Eq. (18) is an N-soliton solution can be proved in the standard way [6, 8] {it should be noted that the explicit determinant representation is difficult to obtain by the inverse scattering method for this model, as also for the standard model of Heisenberg magnetic, i.e., for Eq. (1) without the second term [8]}. Similar to Eq. (14), this solution converges to the bare solution at $x \longrightarrow \infty$, while at finite x values the spectrum of excitations has

on this background $N!$ coupled satellites with incommensurate frequencies.

In conclusion, let us present a quite soluble nonlinear equation gauge-equivalent to Eq. (1) [9]:

$$i\psi_t + (x\psi)_{xx} + 2\psi[x\int|\psi|^2 dx]_x = 0. \qquad (19)$$

Due to the gauge equivalence, the analysis applied to Eq. (1) can also be used in this case.

REFERENCES

1. Yu. A. Izyumov, *Neutron Diffraction by Long-Periodic Structures* (Nauka, Moscow, 1987).
2. L. D. Landau and E. M. Lifshitz, *Course of Theoretical Physics*, Vol. 8: *Electrodynamics of Continuous Media* (Nauka, Moscow, 1982; Pergamon, New York, 1984).
3. R. Jackiw and So-Young Pi, hep-th/9911072.
4. E. Sh. Gutshabash and V. D. Lipovskiǐ, Teor. Mat. Fiz. **90**, 175 (1992).
5. A. V. Mikhaǐlov and A. I. Yaremchuk, Pis'ma Zh. Éksp. Teor. Fiz. **36**, 78 (1982) [JETP Lett. **36**, 95 (1982)].
6. M. A. Salle and V. B. Matveev, *Darboux Transformation and Solitons* (Springer-Verlag, Berlin, 1991).
7. E. Kamke, *Differentialgleichungen; Lösungsmethoden und Lösungen* (Geest and Portig, Leipzig, 1959; Nauka, Moscow, 1961).
8. L. D. Faddeev and L. A. Takhtajan, *Hamiltonian Methods in the Theory of Solitons* (Nauka, Moscow, 1986; Springer-Verlag, Berlin, 1987).
9. S. P. Burtsev, V. E. Zakharov, and A. V. Mikhaǐlov, Teor. Mat. Fiz. **70**, 373 (1987).

Translated by V. Sakun

Lysine IR Emission Spectrum Excited
by Moderately Intense Visible Radiation

E. L. Terpugov* and O. V. Degtyareva

Institute of Cell Biophysics, Russian Academy of Sciences, Pushchino, Moscow region, 142290 Russia
* e-mail: terpugov@icb.psn.ru
Received February 8, 2001

The excitation of IR emission is observed for thin films illuminated by continuous visible light in the absence of light absorption in the sample. The effect is demonstrated by the example of the lysine molecule and explained by the resonant combined action of optical photons with frequencies ω_i and ω_j, whose differences $\omega_i - \omega_j = \Omega$ coincide with the frequencies of the lysine vibrational modes. © *2001 MAIK "Nauka/Interperiodica".*

PACS numbers: 78.30.-j; 78.45.+h; 33.20.Ea; 42.65.Ky

Thermally stimulated IR emission from the surfaces of solids and thin films is analyzed in detail in [1–4]. The then cumbersome measurements of low "positive" and "negative" [5] light fluxes have not been developed further since that time. In addition, when dealing with the positive fluxes, one was forced to heat samples up to a relatively high temperature ($\approx 150°$), which could lead to the sample destruction. The emergence of high-sensitivity Fourier transform infrared (FT-IR) spectrometers greatly facilitated this problem and, in addition, made it possible to excite the IR emission of films by illuminating them in the visible region [6]. This communication is devoted just to this issue. In our experiments, the IR emission was excited in the range of chromophore absorption, as described in [7, 8]. In this work, the IR emission was recorded for the samples not absorbing in the visible region. The observed effects are illustrated by the example of lysine, whose low-frequency IR spectrum shows well-defined absorption bands. As in our previous experiments, the IR emission was excited by a moderately intense visible (nonmonochromatic) light. An attempt is also undertaken to explain the observed effect by the resonant combined action of optical photons with frequencies ω_i and ω_j, whose differences $\omega_i - \omega_j = \Omega$ coincide with the frequencies of the lysine vibrational modes. The emission spectra were recorded on a domestic FT-IR spectrometer FS-02 designed at the TsUP UP RAN and equipped with low-temperature MST detectors (described in detail in [9]). The emission was recorded after removing the standard IR source from the instrument. A sample illuminated by continuous visible light from a 100-W xenon lamp was placed instead. The light was almost normally incident on the sample surface and focused into a 4×1-mm spot using a short-focus glass lens. With the geometry used, the IR emission from the sample did not mix with the exciting visible light (useless light did not fall on the detector). Broadband or interference glass filters were used in the experiments. The sample was a film of lysine amino acid precipitated as a thin layer from the concentrated aqueous solution onto a substrate (KRS-5, CaF_2, or silicon). The sample did not absorb in the visible region. The spectra were recorded at room temperature with a spectral resolution of 4 cm^{-1} and averaged over 400 scans. Figure 1 shows the IR emission spectra of lysine on a KRS-5 substrate in the range from 500 to 3500 cm^{-1}. The absorption spectrum of lysine is shown for comparison. One can see that the IR emission spectrum (curve 1b) recorded with the use of a broadband filter ($\lambda > 560$ nm) reproduces almost all bands at the same frequencies as in the absorption spectrum. Although the set of emission bands is identical to that observed in the absorption spectrum, there is a difference between them primarily in the intensity distribution among the bands. For example, a weak absorption band near 540 cm^{-1} becomes one of the strongest in the emission spectrum in the range from 500 to 1300 cm^{-1}, whereas a strong and broad absorption band at 2500–3300 cm^{-1} is practically absent in the emission spectrum. It is notable that the strongest bands occur only in the low-frequency range and that the envelope of these bands monotonically drops at higher frequencies and resembles in this respect the equilibrium Boltzmann distribution. According to this distribution, the number of molecules vibrationally excited at a given temperature depends on the ratio between the vibrational energy $\hbar\omega$ and the thermal energy kT as

$$n_1 \sim \exp(-\hbar\omega/kT),$$

where k is the Boltzmann constant. The higher the vibrational energy compared to the thermal energy, the lower the number of molecules having this vibrational energy. Because of this, the number of excited molecules decreases rapidly with increasing frequency. For instance, the number of vibrationally excited molecules

with $\omega = 1000$ cm^{-1} should be small at room temperature (~0.7% of all molecules [10]). However, the intensity of a band at 1004 cm^{-1} in the emission spectra of lysine is higher than that given by the Boltzmann distribution. Apart from this band, the other rather intense bands are also seen in the high-frequency range. Thus, the recorded IR emission differs in character from the thermal equilibrium emission and, hence, cannot be characterized by comparing it with the blackbody radiation. It should be noted that the absorption in the substrate (e.g., KRS-5) may also cause heating of the sample even if the film does not absorb in the visible region. However, the low-intensity light beams used in our experiments cannot excite the thermal emission, in contact to the laser radiation [6]. It will be shown in what follows that the origin of IR emission can be understood on the basis of the principles formulated previously for active Raman spectroscopy. Although both the recording method and the observed effects are quite specific in our case, there are grounds to assume that they are based on the physical processes similar to those underlying stimulated Raman scattering. This is primarily related to the fact that, under certain conditions, namely, when the frequency difference between two light waves ω_i and ω_j converging into a beam is at resonance with the vibrational mode $\Omega = \omega_i - \omega_j$ (this situation occurs in our experiments because of the use of a broadband excitation), a selective action (i.e., biharmonic "pumping") takes place, which, as is well known, can phase elementary excitations and alter the population difference between the vibrational levels. This phenomenon was first observed for intense light beams [11]. However, shortly after, a method called active Raman spectroscopy was developed, in which the light beams were considerably less intense and incapable of exciting stimulated Raman scattering [12]. This gives grounds to assume that such a population mechanism may be operative in our case as well, with the sole difference that the population is less intense than in the case of Raman scattering but is sufficient for being detected using the sensitive FT-IR technique.

The validity of this assumption is confirmed by our other experiments. In these experiments, the IR emission was excited by the light monochromatized in a high-quality interference filter or by a copper vapor laser. The signal was detected in neither of these cases. However, the use of interference filters with more than one passband (low-quality filters) allowed the IR emission to be detected with certainty for even less intense light (see, e.g., Fig. 1c). Therefore, the absence of a signal for both monochromatic and a more intense laser radiation gives evidence that not the intensity of exciting radiation but its spectral composition is the governing factor in the excitation of IR emission in our experiments.

Let us consider the experiments with nonstandard interference filters in more detail. The lysine IR emission spectrum recorded with one of such filters is
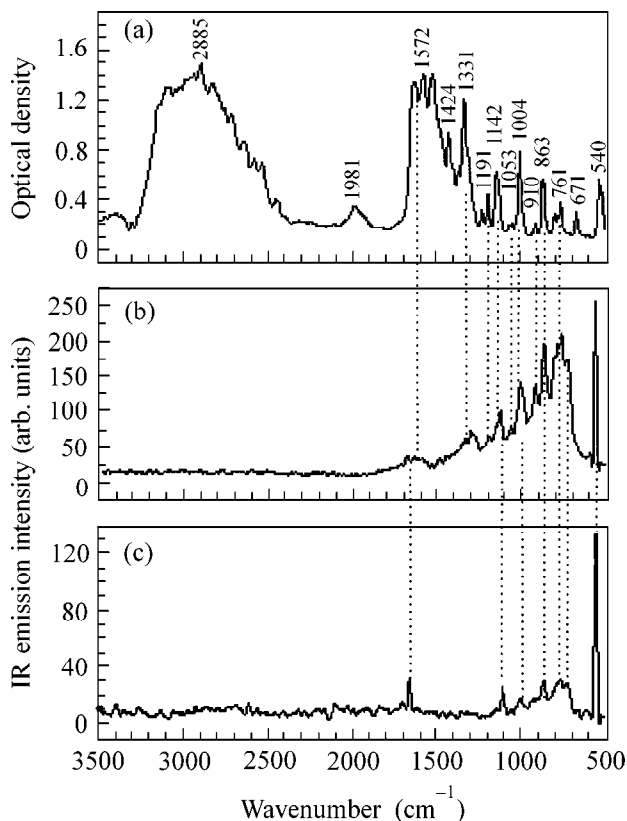
Fig. 1. IR (a) absorption and (b, c) emission spectra of a lysine thin film, as recorded on a two-channel double-beam IR Fourier spectrometer FS-02 at room temperature. The emission spectra are recorded using the (b) broadband ($\lambda > 560$ nm and a power of 320 mW) and (c) nonstandard interference ($\lambda = 633$ nm and a power of 136 mW) filters.

shown in Fig. 1c. Let us compare it with the spectrum obtained using a broadband filter (Fig. 1b). One can see that these spectra differ not in the set of bands but in the intensity distribution that is determined by the spectral characteristic of the filter. For instance, besides the overall decrease in band intensities, the most intense narrow bands (e.g., at 1673, 1115, and 540 cm^{-1}) in the spectrum recorded with the nonstandard interference filter (Fig. 1c) are other than in the spectrum recorded with the broadband filter (Fig. 1b). Some of the intense bands in the spectrum in Fig. 1b completely disappeared in the spectrum in Fig. 1c (e.g., the band at 1331 cm^{-1}). We attempted to model this situation using the spectral distribution of exciting light and assuming that the intensity of stimulated IR emission is proportional to the intensity of exciting light. By choosing a certain frequency of the lysine vibrational mode, we specified the interval $\Delta\omega = \omega_i - \omega_j = \Omega$. Then, we used the spectral distribution of exciting light to determine the possible combinations matching this difference and the corresponding intensities, as shown in Fig. 2a for the frequency $\Omega = 1004$ cm^{-1}. The resulting intensities were summed and then used for determining the intensity of the corresponding band. The intensity distribu-
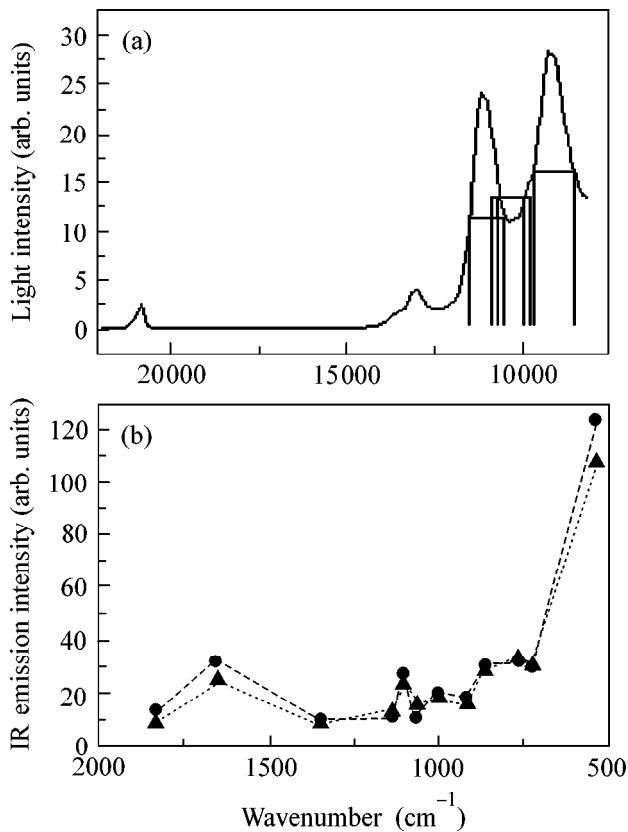
Fig. 2. (a) Spectral distribution of exciting light in the sample for the nonstandard interference filter ($\lambda = 633$ nm); the lengths of horizontal lines correspond to the interval $\Delta\omega = \omega_1 - \omega_2 = 1004$ cm^{-1} (three frequency combinations giving this difference are shown). (b) (●) The experimental band intensities obtained with the interference filter and (▲) the scaled calculated band intensities obtained from the curve in Fig. 2a; the normalization coefficient was determined by the comparison of the intensities (experimental and calculated from the curve in Fig. 2a) for the frequency of 1004 cm^{-1}.

tion (the band intensity corresponded best to the square of intensity of a combined radiation exciting this vibration) is depicted in Fig. 2b by the dashed line with triangles. The circles stand for the real band intensities (Fig. 1c). It is seen from the figure that the experimental and calculated data are in good agreement. Therefore, these results confirm that the IR emission recorded in our experiments is caused by the Raman resonance $\omega_i - \omega_j = \Omega$ of two fields ω_i and ω_j, as a result of which the system is transferred to the nonequilibrium excited state through the biharmonic pumping. Consequently, the emission can be regarded as a process of emitting IR photons upon the transition from the excited vibrational levels to the equilibrium level of the electronic ground state. The possibility of such a transition occurring in the case of intense light beams was demonstrated in [13, 14]. Unfortunately, no data on the processes of vibrational relaxation upon the excitation by low-intensity light beams are known to us. We assume that our data can serve as an indication that these effects

also occur for light intensities less than 500 mW/cm^2, provided that the radiation is not monochromatized.

Note in conclusion that the fact that the angular distribution of visible-light-stimulated IR emission is different for different spectral components—i.e., the emission is not uniform throughout the solid angle (as in the case of thermally stimulated emission) but has a preferential direction—counts in favor of the mechanism suggested and the analogy between the observed effect and stimulated Raman scattering. This issue will be considered elsewhere in more detail.

REFERENCES

1. E. A. Vinogradov and G. N. Zhizhin, Pis'ma Zh. Éksp. Teor. Fiz. **24**, 84 (1976) [JETP Lett. **24**, 71 (1976)].
2. E. A. Vinogradov and G. N. Zhizhin, Fiz. Tverd. Tela (Leningrad) **18**, 2826 (1976) [Sov. Phys. Solid State **18**, 1652 (1976)].
3. E. A. Vinogradov, G. N. Zhizhin, T. A. Leskova, *et al.*, Zh. Éksp. Teor. Fiz. **78**, 1030 (1980) [Sov. Phys. JETP **51**, 520 (1980)].
4. E. A. Vinogradov, G. N. Zhizhin, and V. I. Yudson, in *Surface Polaritons: Electromagnetic Waves at Surfaces and Interfaces*, Ed. by V. M. Agranovich and D. L. Milas (North-Holland, Amsterdam, 1982; Nauka, Moscow, 1985).
5. V. I. Stepanov, *Principles of Spectroscopy of Negative Quantum Luminous Fluxes* (Nauka i Tekhnika, Minsk, 1961).
6. F. J. DeBlase and S. Compton, Appl. Spectrosc. **45**, 611 (1991).
7. E. L. Terpugov and O. V. Degtyareva, Proc. SPIE **4129**, 97 (2000).
8. E. L. Terpugov and O. V. Degtyareva, J. Mol. Struct. 565–566, 287 (2001).
9. A. A. Balashov, V. A. Vagin, A. V. Viskovatich, *et al.*, Proc. SPIE **1575**, 182 (1991).
10. M. M. Sushchinskiĭ, *Raman Scattering and Matter Structure* (Nauka, Moscow, 1981).
11. E. S. Woodbary and W. K. Ng, Proc. IRE **50**, 2367 (1962); N. I. Koroteev and I. L. Shumaĭ, *Physics of High-Power Laser Radiation* (Nauka, Moscow, 1991).
12. S. A. Akhmanov and N. I. Koroteev, *Methods of Nonlinear Optics and Light Scattering Spectroscopy* (Nauka, Moscow, 1981).
13. G. V. Venkin, B. V. Zubov, and A. P. Sukhorukov, in *Proceedings of the II All-Union Symposium on Nonlinear Optics* (Nauka, Novosibirsk, 1968), p. 471.
14. A. Lauberau, A. Seimeier, and W. Kaiser, Chem. Phys. Lett. **36**, 235 (1975).

Translated by V. Sakun

A New Type of Peak Effect in the Magnetization of Anisotropic Superconductors

I. F. Voloshin*, A. V. Kalinov*, L. M. Fisher*, S. A. Derevyanko**, and V. A. Yampol'skiĭ**

* Russian Research Center All-Russia Electrical Engineering Institute, Moscow, 111250 Russia
** Institute for Radiophysics and Electronics, National Academy of Sciences of Ukraine, Kharkov, 61085 Ukraine
Received February 9, 2001

Experimental and theoretical studies of the magnetization curves $M(H)$ obtained for plates of an anisotropic hard superconductor are performed. The samples are YBCO single-domain textured crystals with the **c** axis lying in the sample plane. It is shown that, for some orientations of the magnetic field in the sample plane, the magnetization curves contain additional extrema; at the same time, the virgin magnetization curve $M(H)$ exhibits features characteristic of the peak effect. This proves that the anisotropy of the current-carrying ability can give rise to a new type of peak effect. © 2001 MAIK "Nauka/Interperiodica".

PACS numbers: 74.25.Ha; 74.72.Bk

The peak effect in hard superconductors is the object of many experimental and theoretical studies [1–7]. This effect is usually understood as a nonmonotonic dependence of the critical current density J_c on magnetic field [1, 2]. In many cases, this effect manifests itself as a specific dependence of the irreversible static magnetization M of a superconducting plate on the external magnetic field H [3–7]. The virgin magnetization curve $M(H)$ contains two minima, and additional extrema also appear in the stationary curve $M(H)$. The extrema in weak fields are caused by the penetration of magnetic flux into the entire plate volume, and the additional extrema are related to the increase in J_c in strong magnetic fields. The additional extrema in $M(H)$ can also occur as a result of the strong dependence of J_c on the orientation of the magnetic flux density **B** [8] (see also [9]). Most experimental studies of the peak effect were performed with the external magnetic field oriented normally to a single-crystal plate: **H** ∥ **c**.

In this paper, we show that the dependence $M(H)$ with additional extrema is also observed in a superconducting plate when the magnetic field is parallel to its surface, provided that the sample is characterized by a sufficiently large anisotropy of its current-carrying ability. The studies were performed on $Y_1Ba_2Cu_3O_{7-\delta}$ single-domain textured disks with the **c** axis lying in the sample plane. The reason why we began our search for new features of the curves $M(H)$ with these samples was our earlier study [10] that revealed two size-related maxima in the dependence of the imaginary part of the dynamical magnetic susceptibility χ'' on the amplitude h_0 of an alternating magnetic field oriented at an angle to the **c** axis. This phenomenon was interpreted in terms of the critical state model, which was generalized to the anisotropic case by representing the critical current density as a tensor with the principal values J_{cy} and J_{cz} corresponding to the directions across and along the **c** axis. The presence of two maxima of $\chi''(h_0)$ is due to the sequential penetration of the magnetic flux density components B_z and B_y, each independently shielded by the currents J_{cy} and J_{cz}, into the middle of the plate. In the process of measurement of the magnetization curves, the sweeping magnetic field penetrates into the sample according to the same scenario. Therefore, it is natural to expect that the curve $M(H)$ can also exhibit additional extrema.

The phenomenon observed in our study demonstrates that the anisotropy of the current-carrying ability of the superconductor can give rise to a new type of peak effect due to the sequential penetration of the two components of the magnetic field into the sample.

Experiment. The magnetization curves were measured on YBCO single-domain textured crystals (disks or plates). The samples were cut from a large crystal grown by directional crystallization with an oriented seed. They were cut so that the **c** axis was parallel to the plate surface. The typical sample thickness was 0.2–0.5 mm. The main measurements were performed on a disk with a diameter of 1.3 mm and a thickness of 0.23 mm. The magnetization was measured by a vibrating sample magnetometer in a magnetic field produced by an electromagnet. The sample was mounted so that the dc magnetic field was parallel to its surface. The direction of the field in the sample plane (the **yz** plane) could be varied by rotating the electromagnet. The measurements were performed in the temperature interval 65−77 K.

Using a contactless technique, we preliminarily determined for each of the samples the dependences of the principal components J_{cy} and J_{cz} of the critical cur-
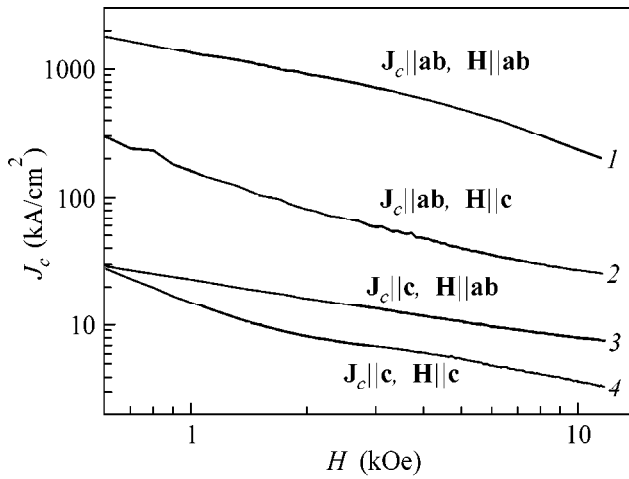
Fig. 1. Critical current densities J_c in the **ab** plane and along the **c** axis versus the magnetic field oriented in the **ab** plane and along the **c** axis at a temperature of 66 K for a superconducting disk with a diameter of 1.3 mm and a thickness of 0.23 mm: (*1*) $J_c \parallel$ **ab** and **H** $\parallel$ **ab**; (*2*) $J_c \parallel$ **ab** and **H** $\parallel$ **c**; (*3*) $J_c \parallel$ **c** and **H** $\parallel$ **ab**; and (*4*) $J_c \parallel$ **c** and **H** $\parallel$ **c**.
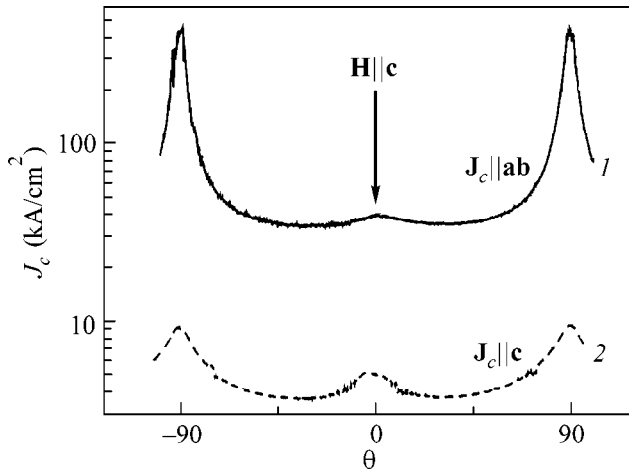
Fig. 2. Angular dependences of the critical current density J_c (*1*) in the **ab** plane and (*2*) along the **c** axis for varying orientation of magnetic field in the disk plane. The disk diameter is 1.3 mm, and its thickness is 0.23 mm; T = 66 K; the angle is measured relative to the **c** axis.

rent density on the magnetic field **H** for its orientations along the principal directions of the crystal, as well as the dependences of J_{cy} and J_{cz} on the orientation of the vector **H** for different values of its magnitude H and different temperatures T. The dependences obtained at T = 66 K are shown in Figs. 1 and 2. The method used for determining the critical current density from the measurements of the low-frequency surface impedance is described in [11, 12].

The magnetization was measured on the zero-field cooled samples. We studied both the virgin magnetization curve and the stationary hysteresis loops of $M(H)$.

Figure 3 shows the dependences of the projection of the magnetization vector onto the direction of the external magnetic field on H for the orientations of **H** along the principal directions of the crystal. One can see that the upper parts of the magnetization loops contain one maximum each, as in isotropic samples with a monotonically decreasing dependence $J_c(B)$. When the field is oriented along the **c** axis, the loops are much wider and the maximum of $M(H)$ occurs in much higher fields than in the case of the field orientation in the **ab** plane. The difference in the curves $M(H)$ is caused by the fact that the critical current density in the **ab** plane far exceeds J_c in the direction of the **c** axis.

When the vector **H** deviates from the principal directions, the magnetization curves are deformed. An example of such a dependence is shown in Fig. 4. After a change in the direction of the field variation, the curve $M(H)$ exhibits a segment with a much smaller slope than the slope of the virgin curve. The most interesting feature of the virgin curve $M(H)$ in a tilted magnetic field is the presence of two minima. This behavior is clearly visible in the inset in Fig. 4. The first minimum occurs approximately at the same values of H as the minimum in the virgin curve *1* in Fig. 3 corresponding to the field orientation in the **ab** plane. The second minimum occurs at the same field values as the minimum in the virgin curve *2*. As the thickness of the sample and the temperature vary, the extrema analogous to those shown in Figs 3 and 4 are shifted according to the changes in the penetration fields H_{py} and H_{pz}. This fact agrees with our assumption that, in a tilted magnetic field **H**, the penetration of the magnetic flux into the sample occurs sequentially: at first, the component B_y penetrates into the sample, because this component is shielded by the weak current J_{cz} [virgin curve $M(H)$ exhibits the first minimum], and then, at much greater values of H, the component B_z penetrates into the sample [the second minimum in $M(H)$]. Two minima in the virgin curve are observed for the angles between the field **H** and the **c** axis within the interval 63°–68°. This interpretation of the effect observed in the experiment is illustrated below by the theoretical calculation of the magnetization curves. The calculation is performed within the framework of the critical-state model generalized to the anisotropic case.

Theoretical calculation of magnetization curves and discussion. To describe the experimental results, we use the simple model [10] that generalizes the known Bean model of the critical state. The Bean model adequately describes the static and low-frequency electrodynamic properties of isotropic hard superconductors. Let us consider an infinite superconducting plate in an external field **H** parallel to its surface. We assume that all fields and currents depend on only one spatial coordinate x directed normally to the plate. The origin of the coordinate $x = 0$ is at the sample surface. We study the simplest type of anisotropy characterized by two principal directions y and z lying in the

plane of the plate. These directions coincide with the crystallographic axes of the sample or with the characteristic directions of the defect structure. If the external field $\mathbf{H}(t)$ is oriented along one of the principal directions, we have only one component of the shielding currents that is perpendicular to $\mathbf{H}(t)$. In this case, only the magnitude $B(x, t)$ of the magnetic field varies in the sample. The spatial distribution of $\mathbf{B}(x)$ is determined by the Bean equation

$$\text{curl } \mathbf{B} = \frac{4\pi}{c} J_c \frac{\mathbf{E}}{E}. \quad (1)$$

In contrast to the isotropic case, we assume that the parameter J_c is a second-rank symmetric tensor J_{cik} ($i, k = y, z$) with the principal values J_c^y and J_c^z. This means that the ith component of the current density is determined by the convolution of the tensor J_{cik} with the vector E_k. Such a model represents the simplest generalization of the Bean model to the anisotropic case.

In the anisotropic model, the equations describing the critical state have the form

$$-\frac{\partial B_z}{\partial x} = \frac{4\pi}{c} J_c^y(B_y, B_z)\cos(\phi(x))\operatorname{sgn}E_y,$$
$$\frac{\partial B_y}{\partial x} = \frac{4\pi}{c} J_c^z(B_y, B_z)\sin(\phi(x))\operatorname{sgn}E_z, \quad (2)$$

where $\phi(x)$ is the angle between the vector $\mathbf{E}(x)$ and the y axis. Similar equations were used in [13] in an electrodynamic description of composite materials.

Like the conventional model of the critical state, the system of Eqs. (2) takes into account the important property of hard superconductors. The density of the current flowing in a certain direction decreases if an orthogonal current component is excited at the same point of the sample. The factors $\cos\phi$ and $\sin\phi$ in Eqs. (2) allow for this fact. This property of hard superconductors leads to an interesting phenomenon consisting in the collapse of the transport current [14] and magnetic moment [15] under the effect of a magnetic field.
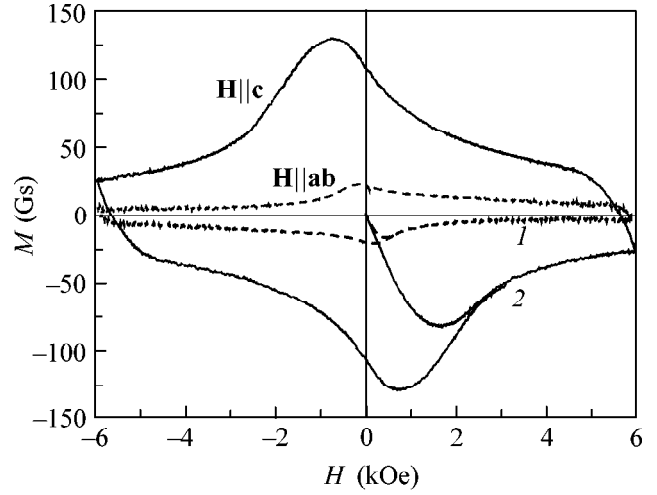
To determine the projection M_H of the magnetic moment onto the direction of the external magnetic field

$$M_H = \frac{1}{4\pi}\left[\frac{1}{d}\int_0^d dx B_y(x)\sin(\theta) + B_z(x)\cos(\theta) - H\right], \quad (3)$$

where θ is the angle between the vector $\mathbf{H}$ and the z axis, we have to solve Eqs. (2) with the boundary conditions

$$B_y(0) = B_y(d) = H\sin(\theta),$$
$$B_z(0) = B_z(d) = H\cos(\theta). \quad (4)$$

These conditions hold when H far exceeds the first critical field, $H \gg H_{c1}$. The signs of the projections of the

Fig. 3. Magnetization curves for a superconducting disk with a diameter of 1.3 mm and thickness of 0.23 mm for two principal directions of the magnetic field: (*1*) $\mathbf{H} \perp \mathbf{c}$ and (*2*) $\mathbf{H} \parallel \mathbf{c}$; $T = 66$ K.
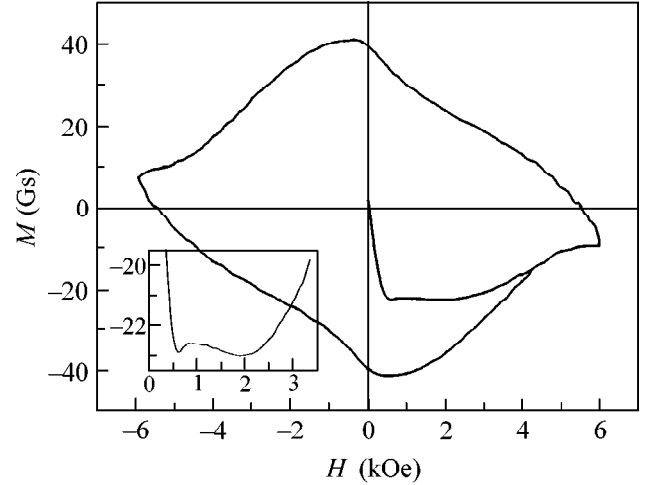
Fig. 4. Magnetization curve for a superconducting disk with a diameter of 1.3 mm and thickness of 0.23 mm in a tilted magnetic field (oriented at an angle of 65° to the **c** axis). The inset shows the virgin magnetization curve with two minima on an enlarged scale.

electric field in Eqs. (2) (the electric field is excited when scanning the magnetic field $\mathbf{H}$) are determined by Faraday's law.

Figure 5 shows the magnetization curve calculated numerically for the conditions close to the experimental ones with the magnetic field making an angle of 65° with the **c** axis. To specify the magnetic-field dependences of the critical current densities $J_c^y(B_y, B_z)$ and $J_c^z(B_y, B_z)$, we used the model expressions corresponding to the sample (see Figs. 1 and 2) for which the main measurements were performed. As a result, we obtained a fairly good qualitative agreement between
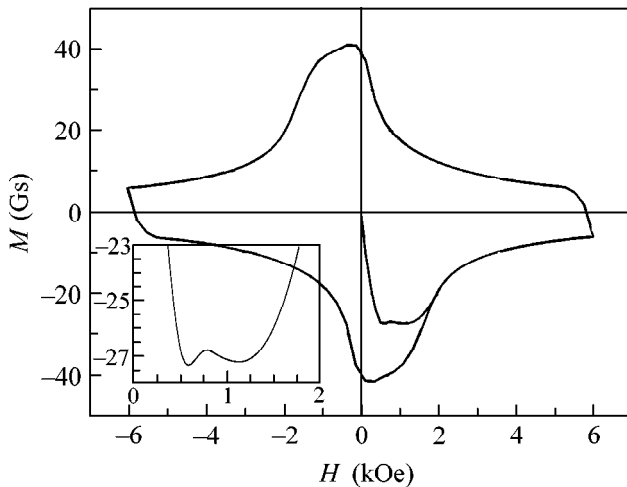
Fig. 5. Calculated magnetization curve of a model sample with the parameters close to the experiment.

the theoretical and experimental virgin magnetization curves (see Figs. 4 and 5). Each curve contains two minima.

The agreement between the calculations and the measured magnetization testifies to the validity of our model and the proposed interpretation of the observed effect. Thus, this paper shows that the anisotropy of the current-carrying ability can give rise to a new type of peak effect that occurs in the magnetization of hard superconductors. The virgin magnetization curve obtained in the experiment contains two minima, as in the case of the peak effect. The calculations show that the anisotropy-related additional extrema of $M(H)$ can also occur in the stationary hysteresis loop of $M(H)$ at a higher value of the anisotropy parameter $\alpha = J_c^y/J_c^z$ in weak magnetic fields.

Thus, the additional extrema observed in the magnetization curves of hard superconductors can be caused by different physical reasons. This fact should be taken into account in interpreting the experimental results.

REFERENCES

1. A. M. Campbell and J. E. Evetts, *Critical Currents in Superconductors* (Taylor and Francis, London, 1972; Mir, Moscow, 1975).
2. R. W. Wördenweber and P. Kes, Phys. Rev. B **34**, 494 (1986).
3. M. Dümling and D. C. Larbalestier, Phys. Rev. B **40**, 9350 (1989).
4. M. Dümling, J. M. Seuntjens, and D. C. Larbalestier, Nature **346**, 332 (1990).
5. V. V. Moshchalkov, A. A. Zhukov, *et al.*, J. Magn. Magn. Mater. **90–91**, 611 (1990).
6. A. A. Zhukov, H. Kupfer, H. Claus, *et al.*, Phys. Rev. B **52**, R9871 (1995).
7. I. F. Voloshin, A. V. Kalinov, K. I. Kugel', *et al.*, Zh. Éksp. Teor. Fiz. **111**, 2158 (1997) [JETP **84**, 1177 (1997)].
8. I. M. Babich and G. P. Mikitik, Phys. Rev. B **58**, 14207 (1998).
9. L. W. Conner, A. P. Malozemoff, and I. A. Campbell, Phys. Rev. B **44**, 403 (1991).
10. L. M. Fisher, A. V. Kalinov, S. E. Savel'ev, *et al.*, Physica C (Amsterdam) **350**, 152 (2000).
11. I. F. Voloshin, L. M. Fisher, N. M. Makarov, and V. A. Yampol'skiĭ, Pis'ma Zh. Éksp. Teor. Fiz. **51**, 225 (1990) [JETP Lett. **51**, 255 (1990)].
12. L. M. Fisher, V. S. Gorbachev, N. M. Makarov, *et al.*, Phys. Rev. B **46**, 10986 (1992).
13. W. J. Carr, Jr., *AC Loss and Macroscopic Theory of Superconductors* (Gordon and Breech, New York, 1983).
14. I. V. Baltaga, L. M. Fisher, N. M. Makarov, *et al.*, Fiz. Nizk. Temp. **21**, 411 (1995) [Low Temp. Phys. **21**, 320 (1995)].
15. L. M. Fisher, A. V. Kalinov, I. F. Voloshin, *et al.*, Solid State Commun. **97**, 833 (1996).

Translated by E. Golyamina

Observation of Andreev–Pushkarov Vacancy Clusters in Phase-Separated Solid Solutions of ^{4}He in ^{3}He

A. N. Ganshin, V. N. Grigor'ev, V. A. Maĭdanov, A. A. Penzev, É. Ya. Rudavskiĭ, and A. S. Rybalko, and E. V. Syrnikov

Verkin Institute for Low Temperature Physics and Engineering, National Academy of Sciences of Ukraine, Kharkov, 61103 Ukraine
* e-mail: rudavskii@ilt.kharkov.ua
Received February 9, 2001

New features are observed for the pressure in a phase-separated dilute solid solution of ^{4}He in ^{3}He subjected to multiple temperature cycling within the phase-separation region. The results are explained within the framework of the hypothesis of A.F. Andreev and D.I. Pushkarov that the vacancies in a crystal without ideal periodicity are surrounded by clusters with a periodic structure. The equation for determining the radius of a cluster of pure ^{4}He in a solution of ^{4}He in ^{3}He is refined. This hypothesis is shown to provide quantitative agreement between the calculated and experimental data under the assumption that the homogenization of the phase-separated solution is accompanied by the formation of metastable vacancies with a concentration of ~$(4–5) \times 10^{-5}$. © 2001 MAIK "Nauka/Interperiodica".

PACS numbers: 67.80.-s

Vacancies in solid helium are quantum objects, so that they can move in a gaslike manner within the energy band formed in a crystal with ideal periodicity. The bottom of this band lies at a distance of its half-width $\Delta/2$ below the ground state [1, 2]. In the absence of strict periodicity, vacancies are localized. Thermodynamic considerations suggest that there is a tendency toward the formation of clusters with periodic structure around the vacancies, because this extends the localization size and, correspondingly, lowers the energy.

A.F. Andreev showed in [3] that, since the periodicity in the ^{3}He crystals is broken because of the chaotic orientations of nuclear spins at temperatures higher than the temperature of nuclear ordering, a ferromagnetic cluster forms around the vacancy. The formation of such clusters provides strong evidence for the quantum nature of vacancies, and the revelation of these clusters may conclusively resolve the as yet persisting controversy over the broad- or narrowband character of the vacansion spectrum (cf. [4–6]). However, attempts at the experimental observation of the effects caused by the formation of such clusters have not yet furnished unambiguous results (see, e.g., [7, 8]).

The periodicity in solid ^{3}He–^{4}He solutions is broken because of the random distribution of the ^{3}He and ^{4}He atoms over the crystal sites. In such a situation, the formation of a cluster consisting only of the ^{4}He atoms around the vacancy is most favorable. Such a situation was considered by D.I. Pushkarov in [9], where the following formula was deduced for the cluster radius:

$$R = \frac{r}{a} = \left(\frac{\pi \Delta}{2T|S|} \right)^{1/5}, \qquad (1)$$

where a is the interatomic distance and S is the entropy of the surrounding solution. For a dilute solution with impurity concentration x, the entropy is

$$S = x \ln x + (1-x) \ln(1-x) \approx x(\ln x - 1). \qquad (2)$$

Any experimental attempts at observing this effect are unknown to us.

In this work, the phenomena occurring in phase-separated dilute solutions of ^{4}He in solid ^{3}He are discussed and explained within the framework of the hypothesis about clustering around metastable vacancies that appear in the course of homogenization of a phase-separated solution. These experiments continue our previous investigations into the phase-separation kinetics in solid ^{3}He–^{4}He solutions [10–12]. The pressure in the solid solution was the main measured parameter. At low temperatures and low impurity content, the pressure depends linearly on the impurity concentration in matrix, which varies during the course of phase separation or solution homogenization [13]. The sample was a disk 9 mm in diameter and 1.5 mm in height. A detailed description of the experimental setup and the method may be found in [11]. The main measurements were performed in the range of 0.1–0.3 K for two samples with close molar volumes V_m and ^{4}He concentrations x_0 ($V_m = 23.99$ cm^3/mol and $x_0 = 2.2\%$ in
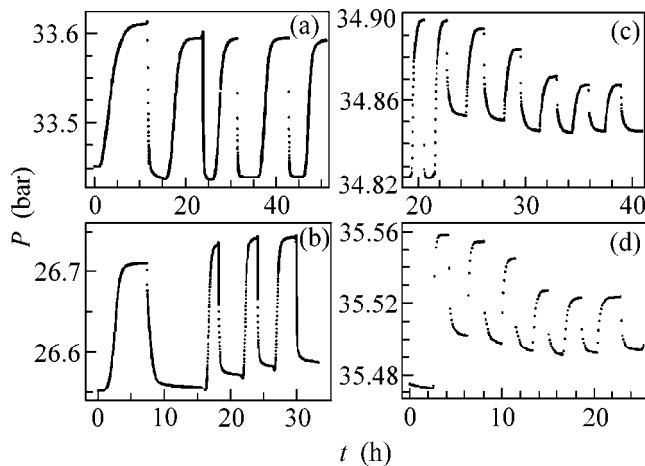
Fig. 1. Behavior of pressure in the phase-separated ^{3}He–^{4}He solid solutions upon temperature cycling in the phase-separation range from $T_i = 110$ mK: (a) solution of 2.05% ^{3}He in ^{4}He, $V_m = 20.44$ cm^3/mol, and $T_f = 204$ mK; (b) solution of 2.05% ^{3}He in ^{4}He, $V_m = 20.92$ cm^3/mol, and $T_f = 204$ mK; (c) solution of 2.2% ^{4}He in ^{3}He, $V_m = 23.99$ cm^3/mol, and $T_f = 190$ mK; and (d) solution of 2.8% ^{4}He in ^{3}He, $V_m = 23.90$ cm^3/mol, and $T_f = 204$ mK.

sample I and $V_m = 23.90$ cm^3/mol and $x_0 = 2.8\%$ in sample II). The samples were prepared by the crystallization of the initial solution with a ^{4}He concentration of about 2% in the gas phase. The concentration x_0 of ^{4}He in the crystal was estimated from the Mullin formula [13] and the pressure change ΔP_0 after complete phase separation in the initial solution,

$$x_0 = \frac{\Delta P_0 \beta V_m}{0.4}, \qquad (3)$$

where the compressibility β of the solution was taken equal to the compressibility of pure ^{3}He, according to the data in [14]. The phase-separation temperatures $T_{s1} = 198$ mK and $T_{s2} = 210$ mK calculated for these concentrations by using the Edwards and Balibar formula [15] coincided with our experimental values to within instrumental accuracy.

It was established in our previous experiments with dilute solutions of ^{3}He in ^{4}He [11] that two types of dependences can be obtained for the pressure in a sample subjected to several cooling and heating cycles within the phase-separation region (as a rule, between 0.1 and 0.2 K).

(a) If the phase separation results in a solid phase of concentrated ^{3}He inclusions, this procedure leads to pressure lowering and provides reproducible growth rates of the new phase. This was considered as evidence of the improvement of crystal quality. The character of pressure variation is illustrated for this case in Fig. 1a.

(b) If the same procedure is applied to a sample with larger molar volume, for which the inclusions of nearly pure ^{3}He are in the liquid state [16], then the pressure increases monotonically with increasing cycle number at both high and low temperatures (Fig. 1b). Such a behavior can be explained by the deterioration of crystal quality because of high stresses arising due to the increased mismatch ΔV between the molar volumes of the initial crystal and the inclusions (in this case, ΔV is approximately four times larger than in the case of the solid ^{3}He inclusions). It is likely that the stresses caused by ΔV values as large as those exceed the yield point of a crystal and give rise to plastic deformation that appear near the inclusion boundaries and are enhanced upon cycling.

Quite a different character of pressure variation was observed in our experiments with a dilute solution of ^{4}He in ^{3}He (Figs. 1c, 1d). A strong decrease in the pressure amplitude at the first cycles and its further stabilization is the most remarkable feature in this case. The stationary amplitude is approximately one-third of its initial value. It is also notable that the initial pressure amplitude is restored only after heating of the phase-separated solution to a temperature appreciably (by several tens of millikelvin) exceeding the phase-separation temperature.

The observed effects may be qualitatively explained within the framework of the following evolution picture. After the first cooling run from the homogeneity region, a certain amount of inclusions of concentrated ^{4}He are separated in the ordinary way. On subsequent heating, these inclusions rapidly dissolve, resulting in a rather sharp pressure decrease. A pressure decrease in the course of heating is favorable to the formation of nonequilibrium vacancies likely in the region of inclusion boundaries, around which, according to the Pushkarov proposal [9], the clusters of pure ^{4}He are formed. Such a structure is poorly mobile and rather stable. In accordance with Eq. (1), the cluster size only decreases slightly upon further increase in temperature, so that the clusters contain a noticeable amount of ^{4}He even near T_s. As a result, the surrounding solution is incompletely saturated, leading to the intense dissolution of ordinary inclusions of concentrated ^{4}He. A decrease in both maximum and minimum pressures at the subsequent cycles (Figs. 1c, 1d) may be considered as a consequence of this process because it leads to the increased mean concentration in the matrix. After several cycles, only those inclusions are retained which are ^{4}He clusters around the vacancies.

For the quantitative analysis of this process, let us make the following assumptions: (i) the vacancy concentration x_v and, hence, the number of clusters at the late stage of the process are constant; (ii) a change in the concentration in the matrix with temperature is determined only by a change in the cluster radius; and

(iii) the vacancies make an independent contribution to the pressure,

$$P_v = \frac{\Delta V_v}{V_m \beta} = \frac{x_v}{\beta}. \tag{4}$$

It follows from Eqs. (3) and (4) that $P_v \approx 60 P_x$ per one particle at $V_m \approx 24$ cm³/mol.

Using the above-mentioned assumptions, one can readily obtain for the directly measured pressure change

$$\frac{P(T) - P_0}{\Delta P_0} = \frac{x_v}{x_0}\left(\frac{V_m}{0.4} + \frac{4\pi}{3}R^3\frac{N_A}{V_m}\right) \approx \frac{x_v}{x_0}(60 + 5.9R^3), \tag{5}$$

where P_0 is the pressure in a homogeneous solution, $P(T)$ is the measured pressure at a given temperature, and N_A is Avogadro's number.

This relationship can be used to calculate the temperature dependence of pressure if the $R(T)$ values are known. The relevant dependences were obtained in experiments where the temperature changed stepwise immediately after cycling, as shown in Figs. 1c and 1d. The results of such an experiment are illustrated in Fig. 2. Note that the pressures corresponding to the minimum and maximum cycling temperatures in this experiment are reproduced rather well, in accordance with the assumption about the quasistationarity of the process. It should also be emphasized that the pressure corresponding to the homogeneous solution is achieved only at a temperature far exceeding T_s.

For the comparison with the experiment to be adequate, one must primarily refine the equation for cluster radius. Equation (1) was obtained in [9] by minimizing the free energy that included only the entropic contribution. However, estimates showed that a change in the ⁴He energy upon clustering makes a comparative contribution.[1] A difference in the ⁴He energies in solution and in pure substance was calculated by Mullin [13], who found that the corresponding contribution to the free energy of dilute ⁴He solutions is $\Delta F = 0.86x$ (K) at a pressure of 35.8 atm close to that used in our experiments.

Mullin's calculations were carried out under the assumption that the crystal structure does not change. Assuming that the cluster has the hcp structure, while the matrix has the bcc structure, one should introduce an additional correction δ_4 for a change in the free energy. According to [15], $\delta_4 \approx 0.026$ K in our case. An additional contribution to the free energy, $\Delta F_\sigma = 4\pi r^2 \sigma$, may also come from the cluster–matrix interfacial ten-

---

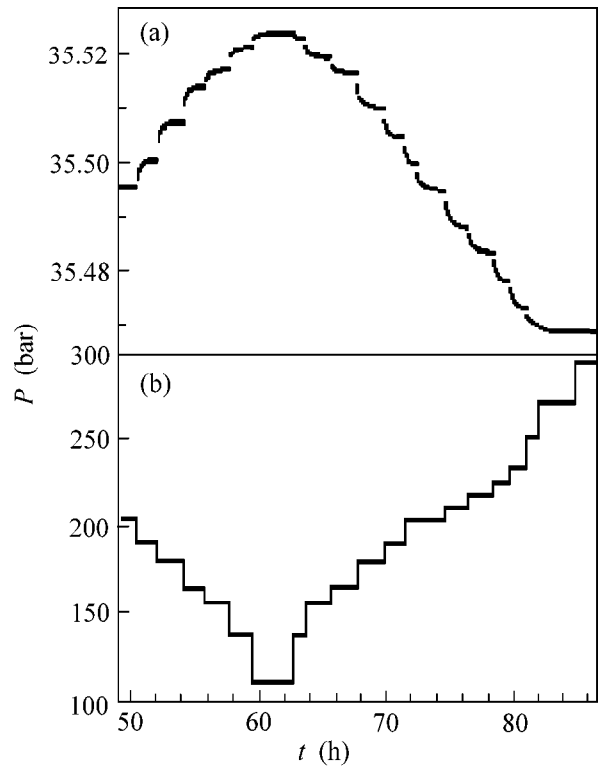[1] Our attention to the possible important role of this component was drawn by A.F. Andreev.

Fig. 2. Pressure (a) and temperature (b) as a function of time (for a stepwise temperature change).

sion σ. The resulting equation for the cluster radius has the form

$$-\frac{\pi\Delta}{R^3} + 2(Tx|\ln x - 1| + 0.86x - 0.026)R^2$$

$$+ 4\frac{a^2}{k}\sigma R = 0, \tag{6}$$

where k is the Boltzmann constant. The negative sign of the last term in brackets is caused by the energetic preferableness of the hcp structure.

Equations (5) and (6) can be used to carry out a comparison with the experiment. The optimization of the calculated and experimental data for sample I with $\Delta = 4$ K [4] gave the following parameters: $x_v \approx (4 \pm 0.4) \times 10^{-5}$ and $\sigma \approx (3.7 \pm 0.3) \times 10^{-3}$ erg/cm² (the errors correspond to the increase in standard deviation by a factor of two). The cluster radius evaluated with these parameters changes from $3.0a$ to $3.6a$.

A comparison between the experimental and calculated data shows a rather good agreement (Fig. 3). The maximum discrepancy is observed at high temperatures, where the cluster radius decreases markedly, leading to the increased probability of cluster decay and, hence, breaking the condition $x_v = $ const that was used in our calculations. The resulting x_v values are quite reasonable. As to the interfacial tension in the phase-separated solid solutions, the relevant data are as
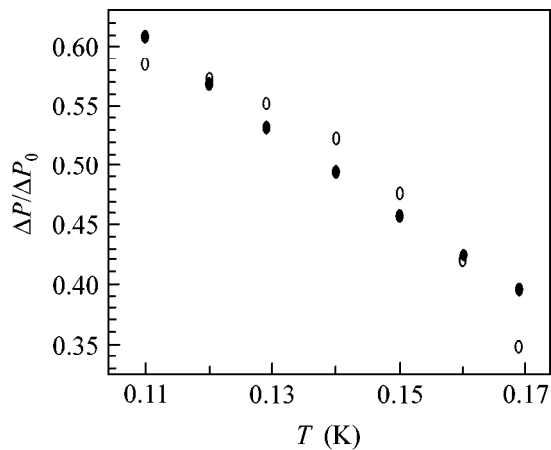
Fig. 3. Comparison of the (○) experimental and the (●) calculated temperature dependences of pressure change in sample I; $V_m = 23.99$ cm^3/mol and $T_f = 190$ mK.

yet lacking. One can see that the values obtained are approximately an order of magnitude smaller than the ones measured for liquid solutions (see, e.g., [17]). In our case, the small value may be due to the expected decrease in σ as the cluster radius approaches the interatomic distance.

A similar processing of a series of experiments carried out for sample II with a higher cycling temperature (204 mK) yielded almost the same results: $x_v \approx (5 \pm 0.5) \times 10^{-5}$ and $\sigma \approx (2.8 \pm 0.4) \times 10^{-3}$ erg/cm^2. The fact that the standard deviation from the experimental data in this case proved to be twice as large as for sample I can presumably be caused by the increased contribution of the above-mentioned high-temperature data.

Inasmuch as the hcp cluster structure is not evident because the matrix can "obtrude" its own structure upon such a small formation, the data were also processed under the assumption of the bcc cluster structure. This gave the following parameters: $x_v = 3 \times 10^{-5}$, $\Delta \approx 10$ K, and $\sigma < 10^{-4}$ erg/cm^2. The fact that the Δ value is larger for the bcc phase correlates with the results obtained in [4]. The smaller σ value at the interface of two bcc structures is also expectable.

The ^{4}He concentration in the matrix can be determined from the measured pressure values by using the ^{4}He conservation law and the Mullin formula [13]. At low temperatures, it was found to be appreciably higher than the concentration corresponding to the phase equilibrium diagram. The difference diminishes with increasing temperature and changes sign near the demixing point. After this, the concentration other than x_0 is retained in the matrix up to $T \approx 270$ mK, which is 60–70 mK higher than T_s of the initial solution.

It is still unclear why the presence of an excess ^{4}He concentration in the matrix at low temperatures is stable and does not initiate the formation of ordinary ^{4}He-enriched phase nuclei upon cooling. It may well be that the depletion of the solution because of ^{4}He clustering prevents the degree of supersaturation from achieving, upon cooling, a level that is sufficient for obtaining an appreciable nucleation rate. As to the formation of a new phase on the cluster, it seems to be unfavorable because of the appearance of one more interface.

Another problem is associated with estimating the probability that the nonequilibrium vacancies appear upon a pressure decrease in the crystal. This process, undoubtedly, should be stimulated by a large amplitude of atomic zero-point vibrations and a high (~10^{-6} s^{-1}) rate of relative density decrease during the course of the sample homogenization, but it is still unclear whether this would suffice to provide the required vacancy concentration.

In conclusion, let us point out some facts that are presented in other works and qualitatively comply with the picture suggested in this paper. Among these is, primarily, the observation of the hysteretic effects and the delay of homogenization to $T > T_s$ in dilute solutions of ^{4}He in ^{3}He. This was most clearly demonstrated in the work of A.S. Greenberg and G. Armstrong [18], where the heat conductivity was measured. The assumption about the formation of vacancy clusters upon homogenization can be invoked to explain a quite paradoxical fact, observed by S.N. Ehrlich and R.O. Simmons in [19], that the lattice parameters in both phases of the phase-separated solution increase upon heating from 0.12 to 0.14 K.

In summary, it is established in this work that the pressure in a phase-separated dilute solid solution of ^{4}He in ^{3}He behaves abnormally upon temperature cycling. It is also demonstrated that this effect can be quantitatively explained within the framework of the Andreev–Pushkarov hypothesis about the formation of clusters of pure ^{4}He around the metastable vacancies in the course of solution homogenization.

REFERENCES

1. A. F. Andreev and I. M. Lifshits, Zh. Éksp. Teor. Fiz. **56**, 2057 (1969) [Sov. Phys. JETP **29**, 1107 (1969)].
2. J. H. Hetherington, Phys. Rev. **176**, 231 (1968).
3. A. F. Andreev, Pis'ma Zh. Éksp. Teor. Fiz. **24**, 608 (1976) [JETP Lett. **24**, 564 (1976)].
4. N. E. Dyumin, N. V. Zuev, V. V. Boĭko, and V. N. Grigor'ev, Fiz. Nizk. Temp. **19**, 980 (1993) [Low Temp. Phys. **19**, 696 (1993)].
5. G. A. Lengua and J. M. Goodkind, J. Low Temp. Phys. **79**, 251 (1990).
6. L. P. Mezhov-Deglin, A. A. Levchenko, and A. B. Trusov, J. Low Temp. Phys. **111**, 545 (1998).
7. N. S. Sullivan and P. Kumar, Phys. Rev. B **35**, 3162 (1987).
8. M. E. R. Bernier and E. Suaudeau, Phys. Rev. B **38**, 784 (1988).

9. D. I. Pushkarov, Pis'ma Zh. Éksp. Teor. Fiz. **27**, 359 (1978) [JETP Lett. **27**, 337 (1978)].

10. V. A. Shvarts, N. P. Mikhin, É. Ya. Rudavskiǐ, *et al.*, Fiz. Nizk. Temp. **21**, 717 (1995) [Low Temp. Phys. **21**, 556 (1995)].

11. A. N. Gan'shin, V. N. Grigor'ev, V. A. Maǐdanov, *et al.*, Fiz. Nizk. Temp. **25**, 796 (1999) [Low Temp. Phys. **25**, 592 (1999)].

12. A. Ganshin, V. Grigor'ev, V. Maidanov, *et al.*, J. Low Temp. Phys. **116**, 349 (1999).

13. W. J. Mullin, Phys. Rev. Lett. **20**, 254 (1968).

14. G. S. Straty and E. D. Adams, Phys. Rev. **169**, 235 (1968).

15. D. O. Edwards and S. Balibar, Phys. Rev. B **39**, 4083 (1989).

16. A. N. Gan'shin, V. N. Grigor'ev, V. A. Maǐdanov, *et al.*, Fiz. Nizk. Temp. **26**, 550 (2000) [Low Temp. Phys. **26**, 401 (2000)].

17. K. Ohishi, H. Yamamoto, and M. Suziki, J. Low Temp. Phys. **112**, 199 (1998).

18. A. S. Greenberg and G. Armstrong, Phys. Rev. B **22**, 4336 (1980).

19. S. N. Ehrlich and R. O. Simmons, J. Low Temp. Phys. **68**, 125 (1987).

Translated by V. Sakun

Gyroscopic Dynamics of Antiferromagnetic Vortices in Domain Boundaries of Yttrium Orthoferrite

M. V. Chetkin, Yu. I. Kurbatova, and T. B. Shapaeva

Faculty of Physics, Moscow State University, Vorob'evy gory, Moscow, 119899 Russia
e-mail: chetkin@magn145.phys.msu.su
Received February 12, 2001

It is established experimentally that the magnetic field directed along the *b* axis has little effect on the velocities of antiferromagnetic vortices in the domain boundary (DB) of yttrium orthoferrite and fails to explain the presence of an appreciable gyroscopic force acting on these vortices. This force is induced by the dynamic canting of magnetic sublattices proportional to the DB velocity. Due to the canting, the velocities of antiferromagnetic vortices depend initially quadratically on the DB velocity, as was experimentally found in this work. The dynamics of antiferromagnetic vortices in the yttrium orthoferrite DBs is gyroscopic and quasi-relativistic, with the limiting velocity of 20 km/s equal to the velocity of spin waves at the linear portion of their dispersion curve. © 2001 MAIK "Nauka/Interperiodica".

PACS numbers: 75.60.Ch

The possibility of antiferromagnetic vortices existing in the domain boundaries of rare-earth orthoferrites was theoretically predicted by Farztdinov *et al.* in [1] and Malozemov and Slonchzewski in [2]. The generation, the dynamics, and the results of head-on binary collisions of antiferromagnetic vortices in the domain boundaries of yttrium orthoferrite were experimentally observed by us in [3–5]. It was established that the absolute velocities of the antiferromagnetic vortices and antivortices in a domain boundary (DB) moving at a speed of 12 km/s are very close to the limiting DB velocity, which is close to the velocity of spin waves at the linear portion of their dispersion curve. This led us to the conclusion that the gyroscopic force was large under conditions of our experiments. The presently existing theory of gyroscopic force in orthoferrites was developed on the basis of the Andreev and Marchenko Lagrangian [6] and predicted that this force is nonzero only if the antiferromagnetic vector is offset from the *ac* plane in a magnetic field directed along the orthoferrite *b* axis [7, 8]. This result is valid if the velocity is small compared to its limiting value. This work is devoted to studying quasi-relativistic dynamics of antiferromagnetic vortices in the yttrium orthoferrite DBs by the method of real-time two-snap high-speed photography.

In connection with the abovesaid, it was of interest to measure experimentally velocities of the antiferromagnetic vortices and antivortices in an external magnetic field applied along the *b* axis of yttrium orthoferrite. In our experiments, the external magnetic field H_b was taken to be ±400 Oe.

The experiments were accomplished by the method of two-snap high-speed photography using the Faraday effect and two red-light laser pulses with a duration of 250 ps and a time delay of 6–10 ns between them. A two-snap high-speed photograph of a 40 μm-thick yttrium orthoferrite plate with a moving DB and flexural solitary waves propagating along the DB is shown in Fig. 1. The solitary flexural waves attend the antiferromagnetic vortices in which the phase transition $G_z F_x \longleftrightarrow G_y$ occurs [4, 5].

In Fig. 1, the domain boundary moves from bottom to top. The velocity of its left part is equal to the speed of transverse sound, and its right part moves with supersonic speed. The transition from light to dark indicates the first position of the dynamic DB, and the transition from dark to light indicates its second position 10 ns later. It is seen from the photograph that pairs of solitary flexural waves with steep leading and extended trailing edges propagate in the opposite directions and lag as a whole from the DB. These real-time photographs can be used to determine the DB velocity *v*, the velocities *u* of the antiferromagnetic vortices and antivortices along the DB, and their absolute velocities.

The time dependences of the distances traversed by the vortices and antivortices along the DB are presented in Fig. 2. The corresponding data are obtained from two-snap high-speed photographs similar to those shown in Fig. 1. It follows from these data that the velocity of antiferromagnetic vortices in a magnetic field of ±400 Oe differs from the velocity of antivortices by no more than 15%. Consequently, the magnetic field used in the experiment was much lower than the effective magnetic field violating the Lorentz-invariant dynamics of topological magnetic solitons to produce the gyroscopic force.

To check these conclusions, the velocity of antiferromagnetic vortex was experimentally studied as a function of the DB velocity. For this purpose, after the generation of antiferromagnetic vortices, a DB with the initial velocity of 12 km/s was either decelerated or accelerated by a magnetic field of an additional coil that was run off a separate pulse generator.

The experimental $u(v)$ curves are shown in Fig. 3. One can see from this figure that the $u(v)$ dependence is quadratic in v ranging from 6 to 9 km/s. At higher v values, an inflection appears in the curve and the velocity of antiferromagnetic vortex reaches at $v = 12$ km/s a maximum value of 16 km/s, which corresponds to the absolute velocity equal to the limiting value $c = 20$ km/s. Thereafter the vortex velocity starts to decrease and tends to zero as $v \longrightarrow c$. In the range of $u(v)$ maximum, the relationship $u^2 + v^2 = c^2$ is strictly obeyed for all experimentally observed amplitudes (from 1 to 10 μm) of solitary flexural waves attending the vortices. The same relationship also holds at higher velocities up to $v = c = 20$ km/s. True enough, the measurements in this range involve difficulties because the amplitudes of flexural waves decrease as $v \longrightarrow c$. The dependence $u = 0.11 v^2$ fits well the initial portion of the experimental $u(v)$ curve.

The experimental dependence $u(v)$ is considerably simpler than the one found for the DB velocity on the magnetic field. Apart from the regions where the velocity is constant and coincides with the speed of longitudinal or transverse sound, the dependence for the domain boundary shows additional features that are associated with its retardation by Winterian magnons.

The absolute velocity of antiferromagnetic vortex was also experimentally studied as a function of the DB velocity. The curve first rises quadratically, then passes through an inflection and flattens out at a level corresponding to the saturation velocity of 20 km/s, which is equal to the velocity of spin waves at the linear portion of their dispersion curve. Therefore, the experiment suggests that the dynamics of antiferromagnetic vortices is quasi-relativistic and gyroscopic.

To explain the appearance of gyroscopic force and the initial quadratic $u(v)$ dependence, dynamic canting of the orthoferrite sublattices [9–11] should be taken into account. In [9–11], this canting was invoked to explain the quasi-relativistic DB dynamics in orthoferrites. The expression for the dynamic canting of sublattices in orthoferrite can be derived using the Lagrangian obtained in [6]. The m_b component of a weak ferromagnetic moment in an ac-type domain boundary moving with a velocity of v was calculated by Bar'yakhtar et al. in [11, 12]:

$$m_b = \frac{v/g \delta M_o \Delta_{01}(v)}{\cosh(x - vt/\Delta_{01}(v))}. \tag{1}$$

Here, M_o is the magnetization of the orthoferrite sublattices, $\Delta_{01}(v)$ is the width of the moving DB, δ is the
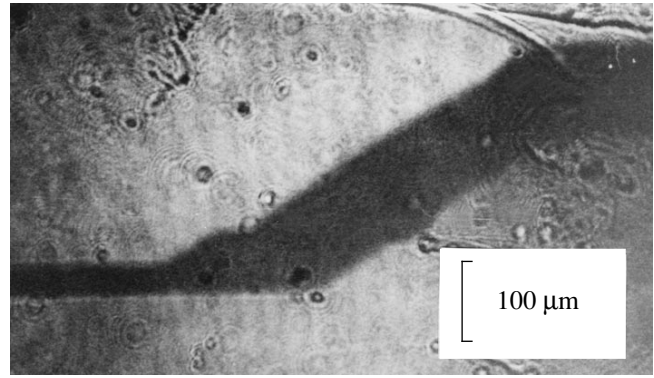

Fig. 1. A two-snap high-speed photograph of a moving domain boundary in an yttrium orthoferrite plate with the flexural solitary waves attending the antiferromagnetic vortex and antivortex and propagating along the domain boundary.
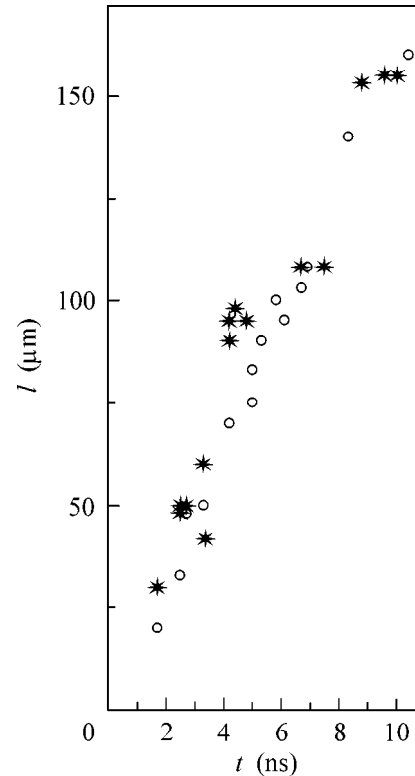
Fig. 2. Experimental time dependence of the distances traversed by the antiferromagnetic (○) vortices and (+) antivortices along the domain boundary in a magnetic field of ±400 Oe directed along the b axis.

parameter of uniform exchange, and g is the gyromagnetic ratio. Similar results were obtained afterwards in [13].

This canting is comparable with the canting induced by the Dzyaloshinski field. The ratio of Eq. (1) to the analogous value caused by the sublattice canting in a
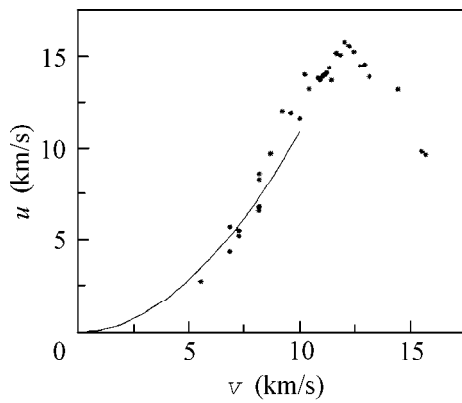
Fig. 3. Experimental dependence of the velocity u of antiferromagnetic vortices along the domain boundary on the boundary velocity v. The $u(v) = 0.11v^2$ dependence is shown by the solid line.

b-directed magnetic field is also large:

$$\frac{m_{b_{\text{dyn}}}}{m_{b_{\text{stat}}}} = \frac{\sqrt{H_A H_E}}{H_b} = 10^2\text{--}10^3.$$

Here, H_A is the anisotropy field in the ac plane, H_E is the exchange field, and H_b is the magnetic field along the b axis. Hence, the dynamic canting of magnetic sublattices, proportional to v/c, is likely the main cause for the appearance of the gyroscopic force in orthoferrites. The gyroscopic force is also proportional to v.

It follows from above that the gyroscopic force acting on the antiferromagnetic vortices in orthoferrites must be proportional to the square of the ratio of the DB velocity to its limiting value, v^2/c^2 [14]. This ratio is not small in our experiment. The gyroscopic force proportional to v^2/c^2 does not follow from [6] and thus calls for theoretical analysis. The presently known theoretical expressions for the magnitude of gyroscopic force in orthoferrites are valid for $v/c \ll 1$ [7, 8, 15]. For the stationary moving antiferromagnetic vortices, the retarding force must be counterbalanced by the gyroscopic force. If the main contribution to the retarding force comes from the leading edge of the solitary wave, then this contribution is proportional to u. For this reason, the relation $u \cong b(v/c)^2$ should hold, as was observed in our experiment.

REFERENCES

1. M. M. Farztdinov, M. A. Shamsutdinov, and A. A. Khalfina, Fiz. Tverd. Tela (Leningrad) **21**, 1522 (1979) [Sov. Phys. Solid State **21**, 878 (1979)].

2. A. P. Malozemov and J. C. Slonchzewski, *Magnetic Domain Walls in Babbles Materials* (Academic, New York, 1979).

3. M. V. Chetkin, Yu. N. Kurbatova, and V. N. Filatov, Pis'ma Zh. Éksp. Teor. Fiz. **65**, 760 (1997) [JETP Lett. **65**, 797 (1997)].

4. M. V. Chetkin, Yu. N. Kurbatova, A. I. Akhutkina, and T. B. Shapaeva, Zh. Éksp. Teor. Fiz. **115**, 2160 (1999) [JETP **88**, 1179 (1999)].

5. M. V. Chetkin and Yu. N. Kurbatova, Phys. Lett. A **260**, 108 (1999).

6. A. F. Andreev and V. I. Marchenko, Usp. Fiz. Nauk **130**, 39 (1980) [Sov. Phys. Usp. **23**, 21 (1980)].

7. Yu. V. Melekhov and O. A. Perekhod, Fiz. Tverd. Tela (Leningrad) **26**, 924 (1984) [Sov. Phys. Solid State **26**, 564 (1984)].

8. M. M. Farztdinov, M. A. Shamsutdinov, and E. G. Ekomasov, Fiz. Tverd. Tela (Leningrad) **30**, 1866 (1988) [Sov. Phys. Solid State **30**, 1076 (1988)].

9. M. V. Chetkin and A. de la Campa, Pis'ma Zh. Éksp. Teor. Fiz. **27**, 168 (1978) [JETP Lett. **27**, 157 (1978)].

10. A. K. Zvezdin, Pis'ma Zh. Éksp. Teor. Fiz. **29**, 605 (1979) [JETP Lett. **29**, 553 (1979)].

11. V. G. Bar'yakhtar, B. A. Ivanov, and M. V. Chetkin, Usp. Fiz. Nauk **146**, 417 (1985) [Sov. Phys. Usp. **28**, 563 (1985)].

12. V. G. Bar'jakhtar, M. V. Chetkin, B. A. Ivanov, and S. N. Gadetskiy, in *Springer Tracts in Modern Physics*, Vol. 129: *Dynamics of Topological Magnetic Solitons: Experiment and Theory* (Springer-Verlag, Berlin, 1994).

13. N. Papanicolaou, Phys. Rev. B **55** (18), 12290 (1997).

14. M. V. Chetkin and Yu. N. Kurbatova, Fiz. Tverd. Tela (St. Petersburg) **43** (2001) (in press) [Phys. Solid State **43** (2001) (in press)].

15. A. K. Zvezdin, Kratk. Soobshch. Fiz., No. 6, 28 (1999).

Translated by V. Sakun

Raman E_1, $E_1 + \Delta_1$ Resonance in Unstrained Germanium Quantum Dots

A. B. Talochkin, S. P. Suprun, A. V. Efanov, I. G. Kozhemyako, and V. N. Shumskiĭ

Institute of Semiconductor Physics, Siberian Division, Russian Academy of Sciences,
pr. Akademika Lavrent'eva 13, Novosibirsk, 630090 Russia

Received February 12, 2001

Raman scattering by optical phonons in unstrained Ge quantum dots obtained in GaAs/ZnSe/Ge/ZnSe structures was studied using molecular beam epitaxy. A shift in the E_1, $E_1 + \Delta_1$ resonance energy due to the quantization of the spectrum of electron and hole states in quantum dots was observed. The properties observed were explained with the use of a simplest model of localization with allowance for the spectrum of Ge electron states. © 2001 MAIK "Nauka/Interperiodica".

PACS numbers: 73.21.La; 78.67.Lt

Semiconductor quantum dots are obtained using molecular beam epitaxy in InAs/GaAs, Ge/Si, and other systems. The mechanical strains in these systems caused by a mismatch of lattice constants of the film and substrate materials (InAs and GaAs, Ge and Si, etc.) lead to a breakdown of the two-dimensional growth mechanism and to the formation of self-organized three-dimensional islands (quantum dots) [1, 2]. The quantum dots obtained in such a process are strongly strained. The deformation of InAs quantum dots obtained in GaAs reaches 7% [2], and that of Ge quantum dots in Si reaches 4% [1]. Such strong deformations lead to large shifts in the spectrum of electron states in the quantum dots and also to significant changes in other parameters [3]. Theoretical calculations [3, 4] and experimental data [5] showed that the strain distribution in quantum dots is nonuniform, which hampers the analysis of the spectrum of electron states. In this work, unstrained Ge quantum dots were obtained in GaAs/ZnSe/Ge/ZnSe structures. The study of resonance Raman scattering by optical phonons showed that the energies of the E_1, $E_1 + \Delta_1$ transitions change as a result of size quantization of the spectrum of Ge electron states and are determined by the quantum dot sizes.

The structures studied were obtained in a molecular beam epitaxy setup with a residual gas pressure of $\sim 10^{-8}$ Pa. The setup was equipped with a high-energy electron diffractometer for determining the surface structure. GaAs wafers with the (110) and (001) orientations were used as substrates. The substrates were passed through a standard chemical treatment, after which they were attached to a molybdenum support with an indium–gallium eutectic. Thermal evaporators served as sources of germanium and zinc selenide, and ZnSe was grown from the compound [6]. An atomically clean surface was obtained in the process of ther-

mal cleaning of the GaAs substrate in a high-vacuum chamber at $T = 580$°C, which was monitored using a high-energy electron diffractometer by the occurrence of surface superstructures. The growth of an epitaxial ZnSe layer 100–500 Å thick was carried out at $T = 230$°C, which provided the preparation of a surface with a 2×1 superstructure stabilized by selenium. Thereafter, a germanium layer with an effective thickness from 10 to 70 Å was deposited at $T \approx 100$°C. Subsequently, Ge was covered with a thin layer of ZnSe (~ 20–40 Å) at the same temperature. Next, the substrate temperature was raised to 230°C, and a ZnSe layer ~ 500 Å thick was grown.

GaAs, ZnSe, and Ge are characterized by close lattice constants: the mismatch does not exceed 0.2%. Mechanical strains in the structures obtained are negligibly small. The mechanism of the growth of Ge quantum dots in this case differs significantly from the Stranski–Krastanov mechanism, which is realized in strained systems. The Ge atoms are weakly bonded to the ZnSe substrate, because Ge forms weak bonds with ZnSe compounds (GeSe and Ge_3Se_2) [6]. The two-dimensional growing film breaks down into an array of three-dimensional islands under the action of surface tension forces. The necessary conditions for growth are attained by the temperature suppression of surface adatom diffusion and island migration and by choosing an optimal rate of Ge supply to the substrate in the process of island formation. The working temperature range is 70–130°C, and the Ge growth rate is ~ 0.4 Å/min. The Ge islands formed at the initial stages of epitaxy are characterized by a certain critical size. This size depends on the growth conditions and varies insignificantly with increasing effective coating thickness up to the coalescence of islands into a continuous layer. The size in the growth plane of Ge quantum dots obtained at $T = 100$°C on the ZeSe surface with the (10) orientation

(a)

(b)
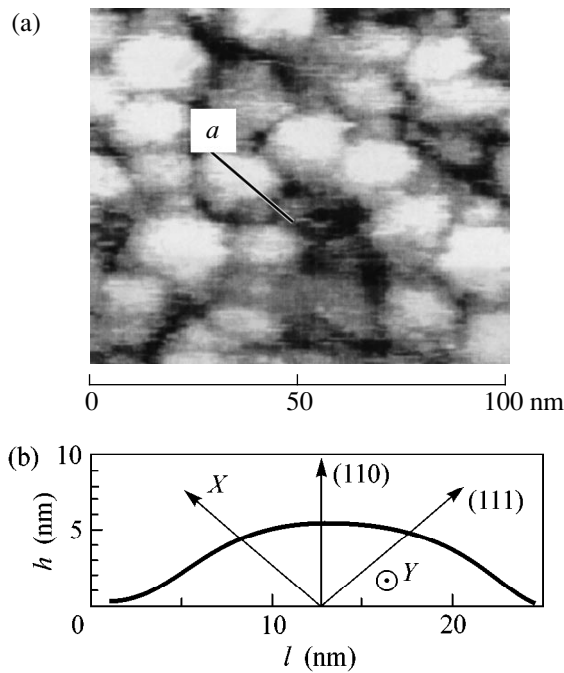
Fig. 1. (a) STM image of the surface of a $(1000 \times 1000$ Å) sample with Ge quantum dots and (b) the profile measured along line *a*; *l* is the size in the growth plane.

is 150–200 Å, and this size for quantum dots obtained on the (100) surface is half as large.

The size and shape of quantum dots were measured using a Riber–Omicron scanning tunneling microscope (STM) for samples that were specially not covered with a ZnSe layer. Figure 1a shows an STM image of the surface of a $(1000 \times 1000$ Å) sample with an effective Ge thickness of 34 Å obtained at a tunneling current of 0.2 nA. The lower part of Fig. 1b demonstrates a profile measured along line *a*. It is clear that the quantum dots are spherical in shape and that the lateral surfaces are not faceted. The characteristic size of quantum dots in the growth plane and their height are 200 and 50 Å, respectively.

Spectra of Raman scattering by optical phonons for the GaAs/ZnSe/Ge/ZnSe structures obtained were studied at temperatures of 300 and 77 K. The spectra were excited by the discrete lines of an Ar laser and were recorded using a DFS-52 spectrometer. The Raman spectra exhibited lines of optical phonons of the GaAs substrate [294 (*LO*) and 268 (*TO*) cm^{-1}] and the ZnSe matrix [250 (*LO*) and 226 (*TO*) cm^{-1}] and the phonon line of Ge [300 cm^{-1} (*LO* + *TO*)]. The position of the Ge phonon peak and the Raman intensities obtained for different polarization geometries coincide with their bulk values, indicating the absence of mechanical strains and significant orientational disorder with respect to the crystallographic directions that are specified by the support. The significant difference between Ge and ZnSe matrix phonon frequencies leads

to the strong localization of optical phonons in quantum dots. Therefore, the electronic states of quantum dots can be investigated using resonance Raman scattering by optical phonons (Raman resonance).

The resonance curves for Raman scattering by optical phonons of Ge in GaAs/ZnSe/Ge/ZnSe structures with quantum dots were studied in the energy range of exciting radiation 2.4–2.7 eV. The curves obtained at $T = 300$ K for three samples are shown in Fig. 2. Experimental points *a*, *b*, and *c* obtained with the Ar laser lines are connected by straight lines, and the intensities are normalized to the scattering volume. Samples *a* and *b* were grown on a surface with the (100) orientation and contained Ge quantum dots with a size of 70–100 Å in the growth plane and a height of 23–28 Å. These samples differ in the effective thickness of the Ge layer, which equals 34 Å for sample *a* and 20 Å for sample *b*. Sample *c* was obtained on a surface with the (110) orientation and contained quantum dots twice as large in size for an effective thickness of the Ge layer of 34 Å. For comparison, Fig. 2 presents a resonance curve obtained in the region of E_1 and $E_1 + \Delta_1$ bulk transitions of Ge [7]. The amplitude of this curve is also normalized to the scattering volume. The vertical arrows in Fig. 2 indicate the positions of the E_1 and $E_1 + \Delta_1$ transitions in Ge. One can see that the resonance position in quantum dots is shifted toward higher energies relative to the bulk position, and the resonance amplitude for sample *a* is three times higher. Note that the density of quantum dots increases with increasing thickness **H** of the effective Ge layer. At $H = 50$–70 Å, the quantum dots coalesce into a continuous layer, the Raman intensity drops sharply, and the shape of the resonance curve follows that of the bulk curve. The behavior observed is due to the quantization of the spectrum of electron and hole states in Ge quantum dots. The direct optical transitions between these states contribute to the E_1, $E_1 + \Delta_1$ Raman resonance.

Let us consider the nature of the resonance in the Ge band structure shown in Fig. 3. The conduction band branch (Λ_1 state) and both branches of the valence band ($\Lambda_{4,5}$ and Λ_6 states) along the $\mathbf{k}_z$ (111) direction are parallel to each other in the major part of the Brillouin zone. The reduced effective mass of the E_1 and $E_1 + \Delta_1$ transitions (indicated by vertical arrows in Fig. 3) is $m = 0.045m_0 = (1/m_e + 1/m_h)^{-1}$ [8] (m_0 is the free electron mass, and m_e and m_h are the electron and hole masses, respectively) in the $(\mathbf{k}_x, \mathbf{k}_y)$ plane perpendicular to the (111) direction. This structure of the spectrum creates a two-dimensional critical point in the interband density of states [9], which reveals itself in optical spectra. Thus, Raman scattering by optical phonons is enhanced when the energy of exciting radiation falls within the region of the E_1, $E_1 + \Delta_1$ transitions (Fig. 2). The three-band processes for which the hole states $\Lambda_{4,5}$ and Λ_6 are mixed by the optical mode deformation potential make the main contribution to the observed

resonance [7]. The two-band contributions from the electron and hole transitions with phonon emission within the same band are much smaller because of the smallness of the intraband deformation potential [7]. The contour of resonance dependence is described by the expression $|\varepsilon_+ - \varepsilon_-|^2$, where ε_+ and ε_- are the contributions to the dielectric constant from the E_1 and $E_1 + \Delta_1$ transitions. This resonance contour is located between the transition energies (Fig. 2). The contribution to Raman scattering from the two-band processes is of the order of $\sim d\varepsilon/d\omega$ for each transition [7], and the resonance contour consists of two peaks at energies E_1 and $E_1 + \Delta_1$.

It is seen in Fig. 3 that the major part of Ge states in the (111) direction are located in the region of the ZnSe band gap. The positions of the ZnSe band edges (valence E_v and conduction E_c) are shown by horizontal lines in Fig. 3. The difference between the energies of these states and the corresponding ZnSe edges forms the localizing potential barrier. As a result, the spectrum of electron states in Ge quantum dots is quantized. The quantization of the carrier motion along the (111) direction does not change the energy of interband transitions, because the electron and hole bands are parallel to each other (Fig. 3). Quantization in the perpendicular ($\mathbf{k}_x$, $\mathbf{k}_y$) plane leads to an increase in the lowest state energy for electrons and holes. The energies of the E_1 and $E_1 + \Delta_1$ transitions are increased by the sum of these energies. The interband density of states, which is a smeared function of energy with a width of Δ_1 in bulk Ge and determines the shape of the resonance (Fig. 2), transforms to a δ function for all $\mathbf{k}_z$. It follows from the frequency dependence $\varepsilon(\omega)$ for a discrete spectrum [9] that the two-band contribution becomes dominant and exceeds the contribution of the three-band processes by a factor of $\sim (\Delta_1/\Gamma)^4 \approx 10^4$, where $\Gamma \sim 20$ meV is the transition broadening in bulk Ge. As a result, the E_1 and $E_1 + \Delta_1$ Raman resonances in Ge quantum dots must manifest themselves as individual peaks. We assign the resonance observed in sample c to the $E_1 + \Delta_1$ transitions in quantum dots. The shift of its position from the bulk value equals 0.13 eV and is shown by a dashed arrow in Fig. 2. The region of the $\mathbf{k}$ space associated with the $E_1 + \Delta_1$ transitions in quantum dots is set off in Fig. 3. With a decrease in size of quantum dots, electron (hole) states occur in the continuous spectrum of ZnSe, resulting in a sharp drop in Raman intensity. When all states from region A (Fig. 3) find themselves in the continuous spectrum, the $E_1 + \Delta_1$ resonance is not observed, whereas the E_1 resonance is now observed for quantum dots half as large in size in the energy range under study (Fig. 2, samples a, b). Its shift equals 0.34 eV, which is marked in Fig. 2 by a dashed arrow. The intensity of the E_1 resonance is three times higher than the $E_1 + \Delta_1$ amplitude because of the larger volume in the $\mathbf{k}$ space (Fig. 3). Thus, the modification of the interband density of states due to spectrum quantization
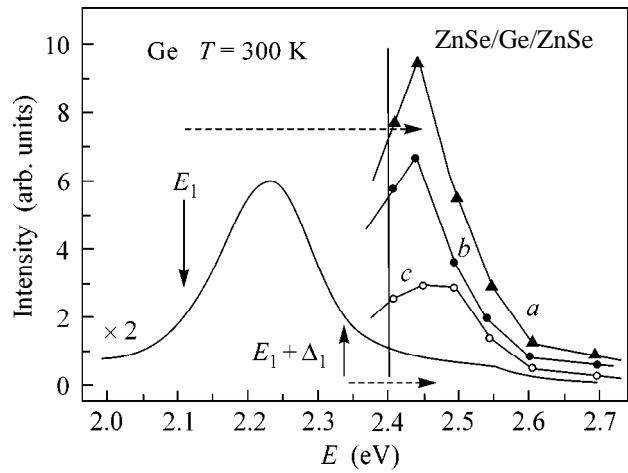
Fig. 2. (a, b, and c) Resonance curves for Raman scattering by Ge optical phonons, as obtained for samples of GaAs/ZnSe/Ge/ZnSe with Ge quantum dots in the energy range of exciting radiation 2.4–2.7 eV. Samples a and b were grown on substrates of the (100) orientation, and sample c was grown on a substrate with the (110) orientation. A resonance curve obtained in [7] for Raman scattering by optical phonons in bulk Ge is shown in the left part by a solid line.

leads to a change of the mechanism of Raman scattering by optical phonons and to an increase in the Raman intensity as compared to bulk Ge.

Let us consider the energies of electron (hole) states in Ge quantum dots. Figure 1b shows the cross section of an island with a plane perpendicular to the base and containing the (111) z and x directions. The y axis is perpendicular to the plane of the figure. The effect of quantum-dot sizes on the motion along the z (111) direction amounts to the quantization of the $\mathbf{k}_z$ momentum of electron (hole) states along this direction. The spectrum will consist of a set of discrete levels with $\mathbf{k}_z = \pi n_1 / h\sqrt{2}$, where n_1 is an integer, h is the island height, and $h\sqrt{2}$ is the size along the (111) direction. The spacing between the levels can be estimated at $\Delta E_z = (dE/dk_z)\Delta k_z \approx 0.1$ eV. The direct transitions between the electron and hole states with the same $\mathbf{k}_z(n_1)$ make a contribution to the observed resonance, and the quantization along the (111) direction does not change its energy. The quantization of electron and hole motion in the (x, y) plane is described by the wavefunction envelope method, because the spectrum depends quadratically on $\mathbf{k}_x$ and $\mathbf{k}_y$. Figure 1b demonstrates that the size of the cross section of a quantum dot in the (x, y) plane varies only slightly in the apex region because of the droplet-shaped form of the island. We will approximate the shape of this cross section by a rectangle with sizes of $\sim h\sqrt{2}$ and $\sim d/2$, where d is the size of the quantum dot base. The energy of a two-dimensional particle of mass m in a rectangular poten-
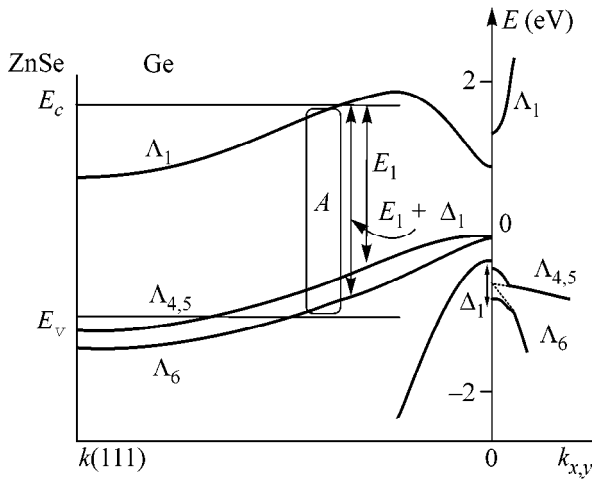
Fig. 3. Band spectrum of bulk Ge calculated in [10] for the (111) direction. Arrows indicate the direct optical transitions associated with the E_1, $E_1 + \Delta_1$ resonance. The dispersion of the electron and hole bands in the $k_{x, y}$ plane perpendicular to the (111) direction in the range of the E_1, $E_1 + \Delta_1$ transitions is shown to the right of the vertical axis.

tial well of an infinite depth is defined by the equation

$$E = (\pi^2 \hbar^2 / 2m)(n_2^2 / 2h^2 + 4n_3^2 / d^2), \qquad (1)$$

where n_2 and n_3 are integers. A system of two-dimensional quantization levels appears for each state with a certain $\mathbf{k}_z(n_1)$. The shift in the ground-state energy ($n_2 = n_3 = 1$) is defined as

$$\Delta E = (\pi^2 \hbar^2 / 2m)(1/2h^2 + 4/d^2). \qquad (2)$$

This equation defines the energy shift of the E_1, $E_1 + \Delta_1$ resonance for $m = (1/m_e + 1/m_h)^{-1}$, thereby allowing for a change in the energy of both the electron and hole states due to size quantization. For the quantum dots of sample *c* (Fig. 2), $h \approx 50$ Å, and the calculated value $\Delta E = 0.163$ eV, in agreement with the observed energy shift of the $E_1 + \Delta_1$ resonance. The average height of quantum dots for samples *a* and *b* is $h \approx 25$ Å. The energy shift defined by Eq. (2) equals $\Delta E = 0.66$ eV, whereas the observed shift of the E_1 resonance is $\Delta E = 0.34$ eV (Fig. 2, sample *a*). This difference is due to the specific features of the dispersion of Ge hole states. The dispersion of hole subbands and the conduction band in the $\mathbf{k}_{x, y}$ plane perpendicular to $\mathbf{k}(111)$ is shown in the right part of Fig. 3 for the range of the E_1, $E_1 + \Delta_1$ transitions. The dispersion of hole bands calculated by the $\mathbf{k} \cdot \mathbf{p}$ method without allowance made for the spin–orbit interaction [10] is shown by the dotted lines. Inclusion of this interaction within a two-dimensional model of the Kane model type [11] removes the degeneracy at $\mathbf{k} = 0$ and also leads to the fact that both subbands are characterized by effective mass $m_h = 2m_e$, where m_e is the mass of the conduction band (Δ_1) in the $\mathbf{k}_{x, y}$ direction. Figure 3 demonstrates that the dispersion goes

into a plateau with a large effective mass at a distance of $\Delta_1/2 = 0.115$ eV from the valence band top. In this case, the mass $m = (2/3)\mathbf{m}_e$ of the E_1 transition increases by a factor of 1.5, and the level shift due to quantization is determined by the electron mass $2m_e$. With allowance made for this fact, Eq. (2) gives $\Delta E = 0.47$ eV. Thus, the use of a simplest model of localization taking into account the properties of the bulk electron-state spectrum of Ge provides an explanation for the observed shifts of the E_1- and $E_1 + \Delta_1$-transition energies in Ge quantum dots.

In this work, Raman scattering by optical phonons in unstrained Ge quantum dots has been studied in the range of the E_1, $E_1 + \Delta_1$ resonance. It is shown that the modification of the interband density of states in quantum dots results in a change of the mechanism of scattering by phonons and in an increase in the resonance amplitude, as compared to bulk Ge. The use of a simplest model of localization taking into account the properties of the bulk electron-state spectrum of Ge provided an explanation for the observed shifts of the E_1- and $E_1 + \Delta_1$-transition energies in Ge quantum dots.

REFERENCES

1. Y.-W. Mo, D. E. Savage, B. S. Swartzentruber, and M. G. Lagally, Phys. Rev. Lett. **65**, 1020 (1990).

2. H. Drexler, D. Leonard, W. Hansen, *et al.*, Phys. Rev. Lett. **73**, 2252 (1994).

3. M. Grundman, O. Stier, and D. Bimberg, Phys. Rev. B **52**, 11969 (1995).

4. A. V. Nenashev and A. V. Dvurechenskiĭ, Zh. Éksp. Teor. Fiz. **118**, 570 (2000) [JETP **91**, 497 (2000)].

5. A. B. Talochkin, V. A. Markov, A. I. Nikiforov, and S. A. Tiĭs, Pis'ma Zh. Éksp. Teor. Fiz. **70**, 279 (1999) [JETP Lett. **70**, 288 (1999)].

6. S. P. Suprun, I. G. Neizvestny, V. N. Sherstyakova, and V. N. Shumsky, J. Phys. Low-Dimens. Struct. **1**, 67 (1995).

7. F. Cerdeira, W. Dreybrodt, and M. Cardona, Solid State Commun. **10**, 591 (1972).

8. K. L. Teo, S. H. Kwok, P.Y. Yu, and Soumyendu Guha, Phys. Rev. B **62**, 1584 (2000).

9. *Light Scattering in Solids*, Ed. by M. Cardona and G. Guntherodt (Springer-Verlag, Berlin, 1982; Mir, Moscow, 1984), Vol. 2.

10. F. Pollak and M. Cardona, Phys. Rev. **142**, 530 (1966).

11. G. L. Bir and G. E. Pikus, *Symmetry and Stain-Induced Effects in Semiconductors* (Nauka, Moscow, 1972; Wiley, New York, 1975).

Translated by A. Bagatur'yants

Condensation of Interwell Excitons in GaAs/AlGaAs Double Quantum Wells

A. V. Larionov and V. B. Timofeev

Institute of Solid State Physics, Russian Academy of Sciences, Chernogolovka, Moscow region, 142432 Russia

Received February 14, 2001

Experimental observations of the collective behavior of interwell excitons in the binary quantum wells with inclined bands under bias are discussed. © *2001 MAIK "Nauka/Interperiodica".*

PACS numbers: 73.21.Fg; 73.20.Mf

Excitons in an intrinsic semiconductor are the lowest energy and electrically neutral electron excitations. Over several decades, excitons have been used as a convenient object for modeling the behavior of a substance in a situation when its density changes or it is exposed to external temperature, pressure, magnetic field, etc. Depending on the density of electron–hole (e–h) excitations and temperature, the situations of weakly interacting exciton gas, molecular exciton gas (biexciton gas), metallic electron–hole liquid, and electron–hole plasma can be realized experimentally.

An exciton consists of two fermions—electron and hole. Therefore, it has an integer spin and is a composite boson. Based on this fact, Moskalenko [1], Blatt *et al.* [2], and Casella [3] assumed in the early 1960s that weakly nonideal and diluted exciton gas in bulk semiconductors can undergo Bose–Einstein condensation (BEC) at low temperatures (in the limit of rarefied exciton gas, $na_{\text{exc}}^3 \ll 1$, where n is the exciton density and a_{exc} is the exciton Bohr radius). Bose–Einstein condensation of excitons in three-dimensional systems implies the macroscopic occupation of the ground state with zero total angular momentum and appearance of a spontaneous order parameter (coherence) in the exciton condensate. In the limit of high e–h density ($na_{\text{exc}}^3 \gg 1$), excitons were treated by direct analogy with the Cooper pairs, while a condensed exciton state or exciton insulator state was described in the mean-field approximation by analogy with the Bardeen–Cooper–Schrieffer superconducting state, with the only difference that the pairing in the exciton insulator is determined by the e–h interaction, while the Cooper pairs are excitons themselves [4–6]. Noticeable Coulomb gaps in the exciton insulator state can arise when electron–hole Fermi surfaces are conformal. Comte and Nozieres [7] demonstrated that the transition between the low- and high-density limits is smooth.

Bose–Einstein condensation in a weakly nonideal Bose gas of given density occurs at critical temperature T_c inversely proportional to the boson mass. This phenomenon was recently observed in rarefied strongly cooled gases of alkali-metal atoms with an integer spin [8–11]. This discovery became possible due to an elegant implementation of atom laser cooling in a gas and to selective accumulation of atoms in small volumes by using magnetic traps. The critical temperatures T_c for these gases proved to be extremely low (tenths of microkelvin) because atomic masses are large and densities are relatively low due to unavoidable losses in cooling and trapping of atoms. In view of the discovery of BEC in rarefied gases of boson atoms, this phenomenon becomes of current interest for excitons. The effective translational masses of excitons in semiconductors are usually low—about or less than the free-electron mass. Therefore, in contrast to the gas of alkali-metal atoms, BEC in the exciton gas at experimentally attainable densities can occur at considerably higher (liquid-helium) temperatures. However, the exciton gas, being a photoexcited and, therefore, nonequilibrium system, also must be cooled to the temperatures of a lattice which plays the role of a thermostat. Because of finite exciton lifetime, the temperature of quasiequilibrium exciton gas in actual experiments is always slightly higher than the temperature of the lattice in which excitons are "immersed." This overheating of the exciton system becomes particularly appreciable at $T < 1$ K because of a small lattice heat capacity and the existence of a narrow small-momentum-transfer region that is insurmountable to one-phonon exciton relaxation ($K < ms/h$, where K is the exciton momentum and s is the speed of sound). In view of this, the objects in which the exciton annihilation (in particular, radiative annihilation) rates are several orders of magnitude lower than the rates of exciton energy relaxation are most appropriate for BEC observation. These conditions are met, in particular, in semiconductors with a indirect gap because the radiative recombination in them involves short-wavelength phonons and, therefore, is slow compared to the relaxation processes establishing thermal equilibrium with the lattice. How-

ever, because of highly degenerate (multivalley) electron and hole spectra and strongly anisotropic effective carrier masses, the lowest state of the interacting $e-h$ system in these semiconductors is an electron–hole liquid into which excitons and exciton molecules are condensed [12, 13]. The exciton condensation into electron–hole liquid droplets was predicted by Keldysh [12] and most comprehensively studied for Ge and Si [13]. The gas of excitons and exciton molecules in equilibrium with the $e-h$ liquid droplets obviously remains a classical Boltzmann gas. By contrast, for direct-gap semiconductors with allowed interband dipole transitions, the exciton recombination is very rapid. Moreover, some other difficulties associated with the dispersion and dynamics of exciton polaritons near $K = 0$ emerge for these semiconductors [14]. Experimental attempts to discover BEC in the exciton gas were undertaken for Cu_2O [15], where the paraexciton ground state is forbidden in zero order in K and is long-lived, and for uniaxially deformed Ge crystals [16] with broken symmetry in the spin degrees of freedom. In Ge, experimentalists dealt with the spin-oriented excitons by direct analogy with spin-aligned hydrogen atoms. In both cases, the degenerate Bose statistics of excitons was quite pronounced at high densities. In our opinion, the critical conditions for the exciton BEC have not been realized for these substances as yet (see, e.g., [17]). However, the investigations are being continued.

In recent years, the exciton BEC has extensively been searched for in two-dimensional (2D) systems based on semiconductor heterostructures. An interest in 2D systems with spatially separated electron–hole layers was stimulated by theoretical studies carried out as early as the mid-1970s [18, 19]. However, it should be recalled that an ideal unconfined 2D system where the density of one-particle states is constant basically cannot undergo BEC at nonzero temperatures because the number of states diverges when the chemical potential vanishes $\mu \longrightarrow 0$ (i.e., the states with $K \geq 0$ can accumulate an unlimited number of Bose particles). Bose condensation can occur only at $T = 0$ K, which is meaningless from the practical point of view. It is pertinent to recall that Hoenberg [20] applied the Bogoliubov inequalities to prove that an ideal unconfined 2D system cannot have a nonzero order parameter because it is destroyed by fluctuations. This proof applies to both superfluid liquid and superconductivity in ideal 2D systems. Mermin and Wagner [21] proved a similar theorem for a 2D model of Heisenberg ferromagnet. We will not consider here the Kosterlitz–Thouless phase transition [22] when the superfluid state in disordered 2D systems can arise due to vortex pairing. This approach is topological and, therefore, does not contradict the theorem proved in [20]. Nevertheless, the BEC can occur at nonzero temperatures in quasi-two-dimensional systems and 2D systems with lateral confinement. The critical BEC temperature in a spatially confined 2D system, where the number of states is finite and the spectrum is

discrete, is equal to $T_c = 2\pi\hbar n/m \log(nS)$ [23], i.e., logarithmically decreases with increasing area S filled with a 2D Bose gas. Finally, semiconductor 2D systems are obviously quasi-two-dimensional because the ratio of the Coulomb energy to the size-quantization energy is not a small parameter in real cases. Moreover, spatial confinement always arises in these systems because of the effect of random potential.

Among the quasi-two-dimensional objects based on semiconductor heterostructures, double quantum wells (DQWs) and superlattices are of special interest to us because they provide spatial separation of photoexcited electrons and holes in neighboring quantum wells (QWs) [24–31]. In DQW with bands inclined due to bias, excitons can be excited whose electron and hole occur in different QWs and are separated by a penetrable tunneling barrier. These excitons are called spatially indirect or interwell excitons (IEs) and differ from the direct intrawell (D) excitons whose electron and hole are in the same QW. Using a GaAs/AlAs heterostructure, Butov et al. [27, 28] realized the situation in which excitons were indirect both spatially and in momentum space. In contrast to the intrawell excitons, interwell excitons are long-lived because the wave functions of their electron and hole only overlap slightly through a tunneling barrier. Therefore, the interwell excitons can easily be accumulated, and a gas of these excitons can be cooled to very low temperatures. Because the inversion symmetry is broken, IEs have a constant dipole moment even in the ground state. The dipole–dipole repulsion prevents these excitons from binding into molecules.

Various possible scenarios of collective behavior in a dense system of spatially separated electrons and holes were theoretically predicted [18, 19, 32–37]. In particular, Lozovik and Berman [37] have demonstrated that, despite the dipole–dipole repulsion between interwell excitons, a liquid dielectric phase of these excitons may become a metastable state of the $e-h$ system at certain critical values of the dipole moment, density, and temperature of IEs. Earlier, Xuejun Zhu et al. [34] pointed out that the condensed dielectric exciton phase (an analogue of Bose condensate) can arise only in the presence of lateral confinement (spontaneous or artificially prepared) in the QW plane. In the presence of this confinement and its attendant external compression, it is easier to accumulate interwell excitons up to the critical densities that are sufficient for the effects of collective exciton interaction to appear. The role of the exciton spin degrees of freedom in Bose condensation was discussed in [35].

In real tunneling-coupled quantum systems based on semiconductor heterostructures, a random potential is always present due to various structural defects—residual charged and neutral impurities, fluctuations of the barrier width and widths of quantum wells, etc. These fluctuations produce random potential relief in the QW planes. For this reason, the photoexcited and

spatially separated electrons and holes in the neighboring QWs, as well as the interwell excitons, can be strongly localized on these fluctuations if the temperature is low enough. This strong localization effect in bound quantum systems manifests itself, in particular, in lateral thermally activated charge-carrier tunneling [29, 30]. In this connection, the properties of delocalized IEs are examined in structures where the density of localized states associated with the random potential is minimal ($<10^{10}$ cm^{-2}).

This review focuses on some recent experiments in GaAs/AlGaAs DQWs with bands inclined by an electric field (n–i–n structures), where IEs exhibit collective behavior upon attaining critical density and temperature. The main information on the IE properties is gained by analyzing the photoluminescence (PL) spectra measured under conditions of continuous or pulsed optical excitation and varying excitation intensity, temperature, and character of polarization of the resonance optical pumping and magnetic field [38–41].

Experimental. We first discuss the IE properties in GaAs DQWs with narrow four-monolayer AlAs barriers separating QWs from each other and isolating each QW from the AlGaAs barrier. The IEs are strongly bound in such a narrow barriers. By applying a bias, one can change the band inclination in these n–i–n structures and, therefore, spatially separate photoexcited electrons and holes in the tunneling-coupled QWs. It is known that, in structures with narrow AlAs barriers grown by the interrupted epitaxial growth technique, fluctuations in the barrier width are large-scale (up to micrometer), so that the corresponding fluctuations in the lateral potential relief will also be large-scale. It is reasonable to expect that IEs at low temperatures will be accumulated in these random lateral large-scale potential wells. It turned out that the IE system under the random lateral confinement conditions exhibits critical behavior as the density increases at low temperature.

The luminescence spectra, shown for (D) intrawell and (I) interwell excitons in Fig. 1, were measured with resonance excitation and various applied biases. The optical transitions under investigation are schematically illustrated in Fig. 1a. In the region of intrawell luminescence at zero bias, two lines, $1sHH$ of free exciton on a heavy hole and of bound exciton, are observed. At negative biases, the spectra exhibit the interwell radiative-recombination line (I line), which almost linearly shifts down in energy as the applied voltage increases, in accordance with the linear Stark shift ($eF\Delta z$, where F is the electric field) of size-quantization levels in QWs. In this case, only the line of the charged exciton complex remains in the intrawell recombination spectrum [42]. At large negative biases $U < -0.4$ V and continuous excitation, the spectra are dominated only by the IE PL, whereas the luminescence of the direct intrawell excitons and exciton complexes is considerably less intense. In this case, the luminescence
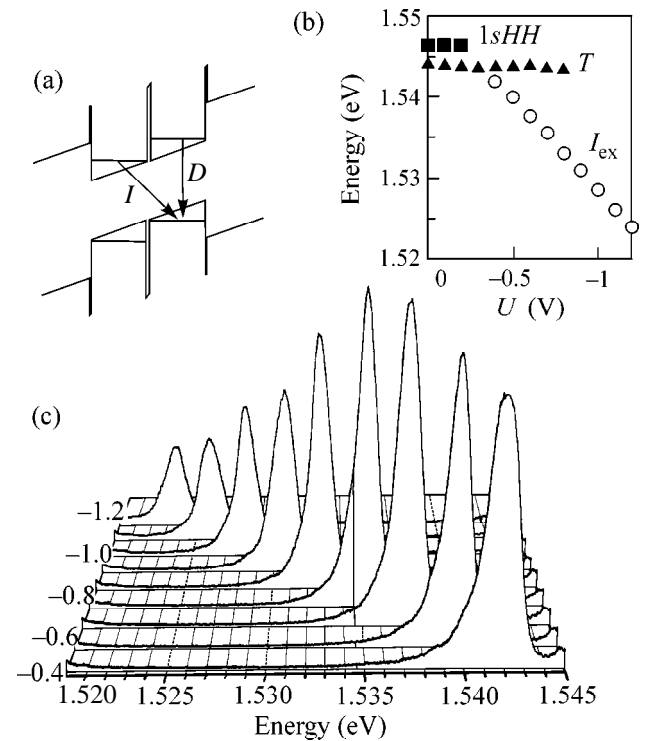

Fig. 1. (a) Scheme of optical transitions. (b) Spectral positions of the lines of the ($1sHH$) direct exciton, (T) exciton complex, and (I_{ex}) IE vs. bias. (c) Luminescence spectra of the interwell excitons at $T = 2$ K for various applied voltages indicated in volts to the left of the spectra.

quantum yield is very high and the nonradiative transitions can be ignored. This conclusion is based on the fact that, as the applied voltage increases, the IE lifetimes change by several orders of magnitude, while the PL intensity does not change appreciably.

The IE luminescence line at low temperatures ($T = 2$ K) and weak pumping is broad (FWHM = 4–5 meV), and the line shape is asymmetric with an extended long-wavelength tail and a sharp violet edge (see Figs. 1, 2). These features of the PL line of IEs are due to the strong localization of IEs on the random-potential fluctuations [29, 30]. In this case, the line width reflects the statistical distribution of the random-potential amplitudes, and the pumping is so weak that the average density of spatially separated electrons and holes is $n_{e-h} < 10^9$ cm^{-2}. At these densities, the statistically averaged IE filling of the lateral random potential wells with linear scales $l < 1$ μm is less than unity and the inhomogeneous width of the PL spectrum of IEs is large enough (see Fig. 2).

The intensity, shape, and width of the IE luminescence line change considerably with increasing intensity of resonance excitation of the direct $1sHH$ intrawell excitons by circularly polarized light (see Fig. 2). As the pumping increases, lines I narrow to 1.3 meV, i.e., by almost a factor of 4. In this case, the maximum intensity increases superlinearly and the line
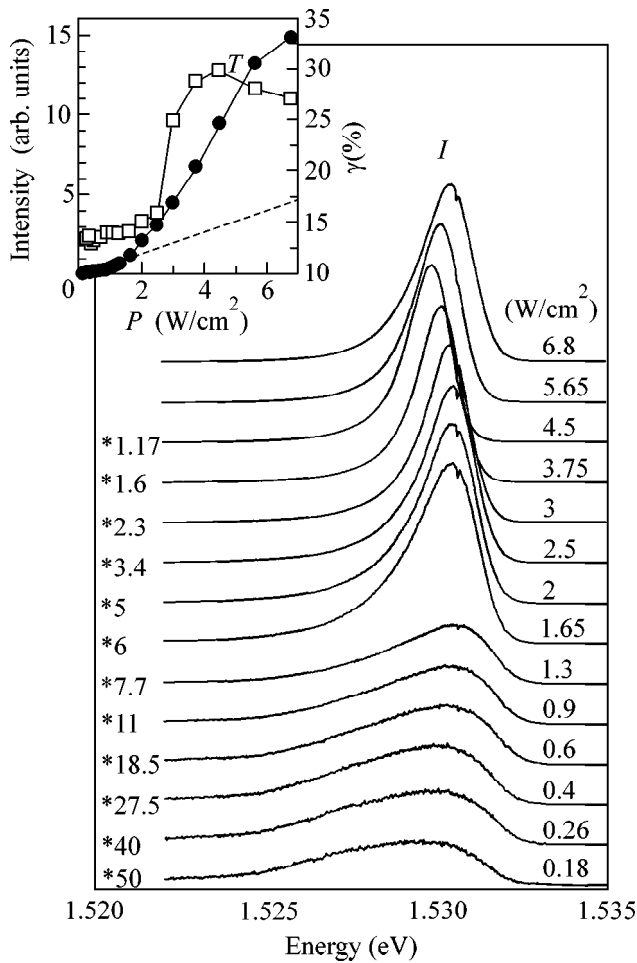
Fig. 2. Spectra of the IE photoluminescence for various intensities of the resonance excitation of the direct 1*sHH* exciton by circularly polarized light (σ^+) at the applied bias of –1 V and $T = 2$ K. The corresponding pump values (in watts per square centimeter) are indicated above the spectra at the right. The inset shows (closed circles, left scale) the IE line intensity and (open squares, right scale) the degree of circular polarization of this line vs. the power density; the dashed line is the extrapolation of the linear dependence of the intensity.

contour becomes almost symmetric. In the region of strong narrowing, the IEs line shifts to lower energies by a value of up to 1.5 meV as pumping increases. Only at rather strong pumping $P > 6$ W/cm^2 does this line shift to higher energies and broaden. The high-energy line shift testifies to the screening of the applied electric field when the IE density becomes large. Therefore, by using the Gauss formula, one can obtain an upper estimate for the IE density from the spectral shift value. This estimate for the IE density gives $n = 3 \times 10^{10}$ cm^{-2} when the line width is minimal. A considerable narrowing of the IE luminescence line is observed for negative voltages in the range from –0.5 to –1.2 V. At large negative biases, similar narrowing of the IE luminescence line occurs at appreciably smaller pumping values.

Strong narrowing of the IE PL line at low temperatures suggests that, as the excitation intensity increases, IEs first fill the localized states caused by the random-potential fluctuations. Each such state can be occupied by only one exciton because of the strong dipole–dipole repulsion between excitons. After the localized states are filled and upon a further increase in pumping, IEs find themselves above the percolation threshold (or mobility threshold associated with the strong localization effect) and become delocalized. These are precisely the delocalized IEs for which the narrow PL line shifts to lower energies with increasing IE density (see Fig. 2). This conclusion indicates that, despite the dipole–dipole repulsion, the ground-state energy of interacting IEs decreases with increasing IE density. This behavior is typical of a degenerate boson system with increasing boson density at a sufficiently low temperature.

The behavior of the degree of circular polarization of the IE luminescence line with an increase in the intensity of resonance excitation in the region of superlinear growth of line intensity is also noteworthy (see Fig. 2). In the experiments under discussion, the circularly polarized light generated direct and completely spin-aligned 1*sHH* excitons for which the total angular momentum of a heavy hole is $J_h = 3/2$ and electron spin is $S_z = -1/2$. As a result of the carrier tunneling and binding into IEs and of the spin-lattice relaxation and spin–orbit interaction, which is strong for holes, the spin "memory" of IEs is partially lost but remains noticeable and is 5–10% at low excitation density, although IEs under these conditions are localized and the corresponding PL line broadens asymmetrically. At a fixed pumping, the degree of IE PL circular polarization decreases monotonically with increasing bias. When the IE PL line narrows strongly with an increase in the power density of resonance photoexcitation, the degree of circular polarization increases several times in a thresholdlike manner. This behavior testifies to the superlinear increase in the number of excitons having preferable angular-momentum orientation. Assuming that the spin-relaxation rate changes only slightly (and most likely increases) with increasing pumping, the increase in the degree of circular polarization can also be associated with a decrease in the IE lifetime. This conclusion follows from the simple expression relating the degree of circular polarization to the lifetimes and spin-relaxation times:

$$\gamma = \gamma_0/(1 + \tau_d/\tau_s),$$

where γ_0 and γ are the degrees of polarization of intrawell and interwell excitons, respectively, and τ_d and τ_s are the radiative recombination and spin-relaxation times of IEs, respectively. Assuming that τ_s is weakly sensitive to pumping and using Eq. (1), one can readily conclude that the experimentally observed threefold increase in the degree of circular polarization of IE PL with increasing excitation intensity results

from at least a fivefold increase in the rate of the radiative annihilation of IEs. The narrow IE line in the PL spectra also appears under pulsed excitation. An analysis of the time evolution of the spectra with pulsed pumping suggests that this line corresponds to a relaxation rate that is almost an order of magnitude higher than that for the PL decay of localized IEs.

As the pumping increases in the resonance excitation of the direct $1sHH$ excitons by linearly polarized light (polarization is parallel to the layer plane), a thresholdlike increase in the linear polarization of the narrow PL line (IE alignment) is observed in the region of superlinear increase in line intensity. When the excitation densities are low and IEs are strongly localized on the random-potential fluctuations, the PL IE spectrum remains slightly polarized under the same conditions. This effect of lateral alignment of IE dipole moments reaches a maximum and then decreases with a further increase in the power density of resonance excitation when the screening of the applied bias becomes appreciable (the pump region for which the PL line starts to broaden and shift to higher energies). The IE alignment also depends on the direction of linear polarization of the resonance excitation in the (001) plane. The azimuthal dependence of the degree of IE PL circular polarization was measured for two power densities of resonance excitation linearly polarized in the (001) plane (Fig. 3): (open squares) small and (closed circles) higher by an order of magnitude. It is seen that the degree of circular polarization of IE PL considerably increases with increasing optical pumping. Strong azimuthal dependence of the degree of circular polarization corresponds to the C_{2v} symmetry and is most likely due to the strong anisotropy of the lateral relaxation time.

The above-described phenomena are very sensitive to the temperature. It was found that, as the temperature increases above the critical values at a fixed strong pumping, the IE line width increases abruptly and the degree of circular polarization decreases to previous values. Figure 4 shows the temperature dependence of the degree of circular polarization and of the IE PL line width. It is seen that in the case under consideration these dramatic changes in the spectrum occur at the critical temperature $T_c \leq 6$ K ($\Delta T = \pm 1$ K).

Let us consider the kinetics of IE luminescence spectra. Butov *et al.* [40, 41] observed an unusual behavior of the IE PL relaxation for pulsed laser excitation. At sufficiently high excitation intensities and low temperatures, the kinetics of radiative IE decay is no longer described by a simple exponential law: the PL intensity increases abruptly immediately after the pulse and then nonexponentially decreases. Figure 5 illustrates these features of the IE PL kinetics. In contrast to such an unusual behavior, the IE radiative decay kinetics becomes single-exponential and is characterized by large times at low excitation intensities, at high temperatures, in the presence of strong disorder caused
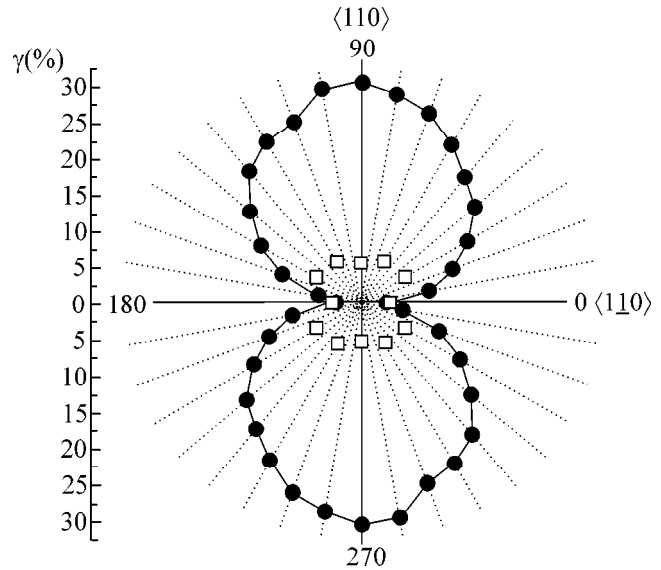
Fig. 3. Azimuthal dependence of the degree of IE PL circular polarization at $T = 1.5$ K under resonance excitation by linearly polarized light for pump values of (closed circles) 4 and (open squares) 0.2 W/cm².

by the random potential, and in the presence of a magnetic field transverse to the heterolayers. It should be noted that only those delocalized excitons radiatively annihilate whose translational momenta are on the order of the light momentum; i.e., $K \leq E_g/hc$, where c is the speed of light in a medium. Butov *et al.* [40, 41] explained the observed increase in the IE radiative recombination rate by two effects. One of them is associated with an increase in the coherence area of IEs when they are condensed into states with momenta less than the light momentum. The second effect is associated with the superlinear occupation of optically active exciton states as a result of the stimulated exciton scattering, when the occupation numbers of exciton states $n > 1$ (i.e., owing to the degenerate Bose statistics of IEs).

Discussion and conclusion. The experimental results described above cannot be explained in the framework of the simple one-particle concept of radiative annihilation of IEs localized on the random-potential fluctuations. Indeed, if the appearance of the narrow line in the photoluminescence spectra is due to the delocalized interwell excitons which can appear above the percolation threshold because of the screening of the random potential, then it is not understood why this phenomenon is so sensitive to the temperature and is absent at $T > T_c$. The thresholdlike increase in the degree of circular polarization and in the alignment of IEs with increasing IE density, as well as the increase in the radiative annihilation rate of excitons in critical conditions, is also not understood. At the same time, these results can be at least qualitatively explained by the collective behavior of delocalized IEs at the critical
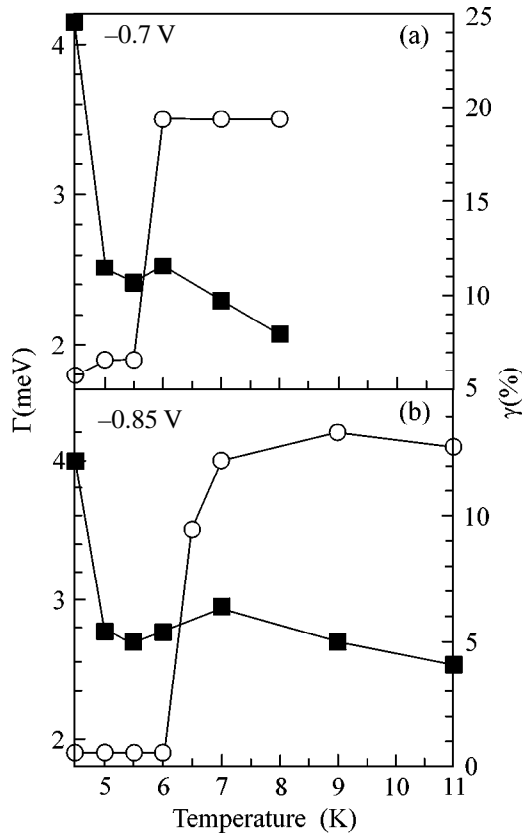
Fig. 4. Temperature dependences of (open circles, left scale) the width Γ of luminescence line of the interwell excitons and (closed squares, right scale) the degree γ of circular polarization of this line for the biases of (upper panel) –0.7 and (lower panel) –0.85 V.

temperature and density. One can assume that our structures with narrow AlAs barriers are characterized by large-scale potential fluctuations, in particular, caused by the variations of barrier width. These potential fluctuations are weakly screened, in contrast to the random potential caused by the residual charged impurities that are also present in the structures under investigation. Due to the large-scale fluctuations of the potential relief in the QW plane, the photoexcited IEs can be accumulated in macroscopically extended regions (up to several tenths of micrometer) with lateral confinement. Indeed, the variations of the QW width $w(r)$ can be associated with the variations of the effective lateral potential $U(r) = U(w(r))$. Under the conditions of quasiequilibrium, the lateral distribution of the exciton density will be determined by the equality $\mu(n(r)) + U(r) = \mu$, where μ is the IE chemical potential depending on the average IE density in QW and $\mu(n)$ is the chemical potential of a homogeneous dielectric exciton phase in the lateral confinement region. It is obvious that $|\mu(r)| < |\mu|$ because $\mu(n) = -|E_{exc}| + |\delta U|$ (E_{exc} is the exciton binding energy), and the exciton density in the lateral confinement region can be considerably higher than the average density in the QW plane.

These are precisely the regions where the main events associated with the photoexcited IEs occur.

One can assume that the strong narrowing of the IE PL line and the critical sensitivity of this phenomenon to the density and temperature are due to the IE condensation into a collective dielectric exciton phase. Lozovik and Berman [37] have demonstrated that a dense IE system can be condensed into a dielectric phase at certain IE dipole-moment values, despite the dipole–dipole repulsion between excitons. Xuejun Zhu *et al.* [34] pointed out that this condensation can most likely occur in the lateral confinement regions. The experiments described above indicate that with continuous excitation this condensation occurs at $T < 5.5$ K and at the average exciton density of 3×10^{10} cm^{-2}. The narrowing of the IE PL line with an increase in the IE density at low temperature is accompanied by a systematic shift of this line to lower energies (by about 1.5 meV). Only a sufficiently dense system of Bose quasiparticles can exhibit such a behavior at $\mu/kT \longrightarrow 0$. These observations provide independent support to the assumption that we deal with a dense enough dielectric collective IE phase in our system. In this phase, the IEs retain their individual properties. This conclusion is corroborated by the investigations of the PL spectra in a magnetic field with Faraday geometry. Larionov *et al.* [39] have found that the narrow line, similar to a free exciton, splits into the Zeeman doublet with the intensity ratio of the σ^+ and σ^- components corresponding to the temperature and spin-splitting value.

The condensed fraction of excitons should be phased within the coherence region. The spatial coherence must arise at least on the scale of the IE de Broglie wavelength $\lambda_{ex} = \hbar/\sqrt{\pi mkT}$ whose value of 1.5×10^3 Å at $T = 2$ K exceeds the exciton Bohr radius $a_B \sim 100$ Å by more than an order of magnitude. The exciton density under the same conditions corresponds to the dimensionless parameter $r = n \times \lambda_{ex}^2 = 4$. An increase in the spatial coherence in the condensed phase is evidenced by the observed thresholdlike increase in the IE alignment. It is known that the alignment is closely related to the lateral relaxation and, therefore, to the time of phase-coherence loss. The radiative decay of the phase-correlated IEs in the condensate should be characterized by considerably higher radiative probabilities than the PL of uncondensed excitons. This conclusion is also consistent with the experiment because the radiative probability of the narrow line in the PL spectra of condensed IEs is an order of magnitude higher than that for the localized excitons.

Nevertheless, the important problem of spatial coherence scale of this collective state remains to be solved in the context of justification of the assumption that IEs are condensed into the dielectric collective phase. The answer may be obtained, e.g., by measuring the correlations in the photoluminescence intensity under the conditions where the assumed exciton con-
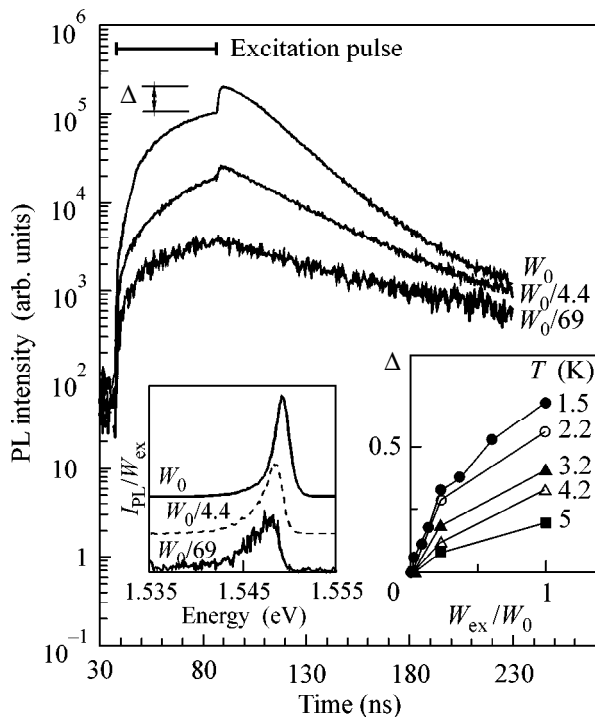
Fig. 5. IE photoluminescence kinetics measured at the maximum of the integral PL spectrum at $U = 1$ V and $T = 1.5$ K for various excitation power densities W_{ex}. $W_0 = 10$ V/cm^2. The excitation pulse is rectangular-shaped and of 50-ns duration. The left inset shows the respective integral PL spectra. The right inset shows the IE PL intensity Δ, which increases after the termination of laser pulse action, vs. the excitation power density for various temperatures.

densation occurs. Because the exciton condensation occurs in the lateral domains related to the large-scale random-potential fluctuations, the investigations of the PL of individual domains by microprobe optical microscopy are of interest. It is expected that the IE PL from an individual domain containing condensate should be completely circularly polarized under the condensation conditions. In the presence of a weak coupling between domains, time beats in the degree of linear polarization can be expected (optical analogue of the Josephson effect).

REFERENCES

1. S. A. Moskalenko, Fiz. Tverd. Tela (Leningrad) **4**, 276 (1962) [Sov. Phys. Solid State **4**, 199 (1962)].

2. I. M. Blatt, K. W. Boer, and W. Brandt, Phys. Rev. **126**, 1691 (1962).

3. R. C. Casella, J. Appl. Phys. **34**, 1703 (1963).

4. L. V. Keldysh and Yu. V. Kopaev, Fiz. Tverd. Tela (Leningrad) **6**, 2791 (1965) [Sov. Phys. Solid State **6**, 2219 (1965)].

5. L. V. Keldysh and A. N. Kozlov, Zh. Éksp. Teor. Fiz. **54**, 978 (1968) [Sov. Phys. JETP **27**, 521 (1968)].

6. A. N. Kozlov and L. A. Maksimov, Zh. Éksp. Teor. Fiz. **48**, 1184 (1965) [Sov. Phys. JETP **21**, 790 (1965)].

7. C. Comte and P. Nozieres, J. Phys. **43**, 1069 (1982); **43**, 1083 (1982).

8. M. H. Anderson, J. R. Fisher, M. R. Matthews, *et al.*, Science **269**, 198 (1995).

9. K. B. Davis *et al.*, Phys. Rev. Lett. **75**, 3969 (1995).

10. C. C. Bradley, C. A. Sackett, J. J. Tollett, and R. G. Hulet, Phys. Rev. Lett. **75**, 1687 (1995).

11. D. S. Jin, J. R. Ensher, M. R. Matthews, *et al.*, Phys. Rev. Lett. **77**, 420 (1996).

12. L. V. Keldysh, in *Proceedings of the IX International Conference on Physics of Semiconductors, Moscow, 1968*, Vol. 2, p. 1384.

13. *Modern Problems in Condensed Matter Physics*, Vol. 6: *Electron-Hole Droplets in Semiconductors*, Ed. by C. D. Jeffries and L. V. Keldysh (North-Holland, Amsterdam, 1983).

14. *Modern Problems in Condensed Matter Sciences*, Vol. 2: *Excitons*, Ed. by E. I. Rashba and M. D. Sturge (North-Holland, Amsterdam, 1982).

15. D. Hulin, A. Mysyrowicz, and C. Benoit a la Guillaume, Phys. Rev. Lett. **45**, 1970 (1980); D. W. Snoke, J. P. Wolf, and A. Mysyrowicz, Phys. Rev. B **41**, 11171 (1990); E. Fortin, S. Fafard, and A. Mysyrowicz, Phys. Rev. Lett. **70**, 3951 (1993); A. Mysyrowicz, E. Fortin, E. Benson, *et al.*, Solid State Commun. **92**, 957 (1994); A. Mysyrowicz, E. Benson, and E. Fortin, Phys. Rev. Lett. **78**, 3226 (1997).

16. I. V. Kukushkin, V. D. Kulakovskiĭ, and V. B. Timofeev, Pis'ma Zh. Éksp. Teor. Fiz. **34**, 36 (1981) [JETP Lett. **34**, 34 (1981)]; V. B. Timofeev, I. V. Kukushkin, and V. D. Kulakovskiĭ, Physica B & C (Amsterdam) **117–118**, 327 (1983).

17. G. A. Kopelevich, S. G. Tikhodeev, and N. A. Gippius, Zh. Éksp. Teor. Fiz. **109**, 2189 (1996) [JETP **82**, 1180 (1996)]; Phys. Rev. Lett. **78**, 3226 (1997).

18. Yu. E. Lozovik and V. I. Yudson, Pis'ma Zh. Éksp. Teor. Fiz. **22**, 556 (1975) [JETP Lett. **22**, 274 (1975)].

19. S. I. Shevchenko, Fiz. Nizk. Temp. **2**, 505 (1976) [Sov. J. Low Temp. Phys. **2**, 251 (1976)].

20. P. C. Hoenberg, Phys. Rev. **158**, 383 (1967).

21. N. Mermin and H. Wagner, Phys. Rev. Lett. **17**, 1133 (1966).

22. J. M. Kosterlitz and D. J. Thouless, J. Phys. C **6**, 1181 (1973).

23. W. Ketterle and N. J. van Druten, Phys. Rev. A **54**, 656 (1996).

24. T. Fukuzawa, E. E. Mendez, and J. M. Hong, Phys. Rev. Lett. **64**, 3066 (1990).

25. J. E. Golub, K. Kash, J. P. Harbison, and L. T. Flores, Phys. Rev. B **41**, 8564 (1990).

26. J. A. Kash, M. Zachau, E. E. Mendez, *et al.*, Phys. Rev. Lett. **66**, 2247 (1991).

27. L. V. Butov, A. Zrenner, G. A. Abstreiter, *et al.*, Phys. Rev. Lett. **73**, 304 (1994).

28. L. V. Butov, in *Proceedings of the 23rd International Conference on Physics of Semiconductors, Berlin, 1996.*

29. V. B. Timofeev, A. I. Filin, A. V. Larionov, *et al.*, Europhys. Lett. **41**, 435 (1998).

30. V. B. Timofeev, A. V. Larionov, A. S. Ioselevich, *et al.*, Pis'ma Zh. Éksp. Teor. Fiz. **67**, 580 (1998) [JETP Lett. **67**, 613 (1998)].

31. V. V. Krivolapchuk, E. S. Moskalenko, A. L. Zhmodikov, *et al.*, Solid State Commun. **111**, 49 (1999).

32. D. Yoshioka and A. H. MacDonald, J. Phys. Soc. Jpn. **59**, 4211 (1990).

33. X. M. Chen and J. J. Quinn, Phys. Rev. Lett. **67**, 895 (1991).

34. Xuejun Zhu, P. B. Littlewood, M. S. Hybersen, and T. Rice, Phys. Rev. Lett. **74**, 1633 (1995).

35. J. Fernández-Rossier and C. Tejedor, Phys. Rev. Lett. **78**, 4809 (1997).

36. Lerwen Liu, L. Swierkowski, and D. Nelson, Physica B (Amsterdam) **249–251**, 594 (1998).

37. Yu. E. Lozovik and O. L. Berman, Zh. Éksp. Teor. Fiz. **111**, 1879 (1997) [JETP **84**, 1027 (1997)].

38. A. V. Larionov, V. B. Timofeev, J. Hvam, and C. Soerensen, Pis'ma Zh. Éksp. Teor. Fiz. **71**, 174 (2000) [JETP Lett. **71**, 117 (2000)].

39. A. V. Larionov, V. B. Timofeev, J. Hvam, and C. Soerensen, Zh. Éksp. Teor. Fiz. **117**, 1255 (2000) [JETP **90**, 1093 (2000)].

40. L. V. Butov, A. Imamoglu, A. V. Mintsev, *et al.*, Phys. Rev. B **59**, 1625 (1999).

41. L. V. Butov, A. V. Mintsev, Yu. I. Lozovik, *et al.*, Phys. Rev. B **62**, 1548 (2000).

42. V. B. Timofeev, A. V. Larionov, M. Grassi Alessi, *et al.*, Phys. Rev. B **60**, 8897 (1999).

Translated by R. Tyapaev